Transitions of Collective Flow Observables at Intermediate Energies

By

Daniel Joseph Magestro

A DISSERTATION

Submitted to
Michigan State University
in partial fulfillment of the requirements
for the Degree of

DOCTOR OF PHILOSOPHY

Department of Physics and Astronomy

2000

ABSTRACT

Transitions of Collective Flow Observables at Intermediate Energies

By

Daniel Joseph Magestro

The comparison of experimental collective flow studies to model calculations has suggested various qualities of nuclear matter, such as the momentum dependent nuclear mean field and the reduced in-medium nucleon-nucleon cross section. Transitions in collective flow observables are particularly beneficial, since these transitions are mostly independent of experimental biases and therefore better suited for relating to theory. Three known transitions in collective flow observables exist, two of which occur at NSCL energies: the disappearance of directed flow (balance energy) and the disappearance of elliptic flow (transition energy).

The disappearance of directed flow in intermediate energy heavy-ion collisions is measured for the ^{197}Au+^{197}Au system using the Michigan State University 4π Array. Previous experiments have extrapolated values of the Au+Au balance energy, but a recent quantum molecular dynamics study suggested that the balance energy cannot be measured directly for Au+Au due to a prohibitively large Coulomb force. Boltzmann-Uehling-Uhlenbeck (BUU) model calculations are performed to show that the Coulomb interaction lowers the experimental balance energy significantly but does not suppress the observable completely. Also, BUU calculations show that the dual dependence of the balance energy on nuclear compressibility and in-medium cross section seen for light- and medium-sized systems reduces to a single dependence on the nuclear compressibility, allowing for the first time a characterization of the nuclear equation of state using the balance energy.

The disappearance of elliptic flow is measured for ^{40}Ar+^{45}Sc, ^{58}Ni+^{58}Ni, ^{86}Kr+^{93}Nb and ^{197}Au+^{197}Au. The transition energy for Au+Au exhibits a strong impact parameter dependence, in contrast to the balance energy for the same system which is nearly independent of impact parameter. However, the transition energy appears to decrease with increasing system mass, which is in accordance with the mass dependence of the balance energy. Comparison of experimental ^{40}Ar+^{45}Sc data to published model calculations of ^{48}Ca+^{48}Ca allows one to study the nuclear EOS using the transition energy for the first time. For the two independent cases of Au+Au directed flow and Ar+Sc elliptic flow, comparison of data with BUU calculations indicates a soft equation of state and a reduced in-medium cross section.

for those who never

doubted my intentions

ACKNOWLEDGEMENTS

It is somewhat of a cliché to say that one's time in graduate school was filled with highs and lows, but for me the adage is not an exaggeration. In my four years and six months at MSU, I managed to garner attention through great successes, such as the departmental T.A. award, the Research Recognition Day award, and strong commitments to the REU program, graduate student recruitment, NSCL outreach efforts, NSCL student seminars, and teaching scholarship. But my letdowns also drew necessary attention: three attempts at the old Candidacy Exam, below average coursework for the first year, and the deserved ire of more than one departmental secretary.

The biggest consequence of all these events is my interaction with the Physics and Astronomy faculty in more ways than I ever imagined possible. I especially have worked in one way or another with nearly every faculty member at the Cyclotron, and the completion of my Ph.D. degree is as much a credit to their guidance and enthusiasm as it is to my own perseverance. It is partly because of them that I have such affection for the NSCL and for Michigan State University, and I proclaim without remorse that the village certainly raised the boy.

I would like to thank Gary Westfall, whose strong commitment as an advisor began at a conference in Berkeley when he skipped some talks to convince me to apply to MSU. He has supported me unwaveringly through the tribulations of graduate school in ways too numerous to remember fully, and he always made me believe I was fully capable of trouncing any challenge (data-related or not) I faced. His most appreciated act, but also just a typical example, was the day I expressed my passion for teaching to him. Within a couple hours, I had e-mails from the associate chair of the department and a meeting with Dr. Benenson to discuss ways I could get involved in teaching

within our department. Even the difficult decision to move to Germany owes greatly to his persistent encouragement! Special thanks goes to my committee, Wolfgang Bauer, Bernard Pope, Phil Duxbury, and Thomas Glasmacher, for serving on my hastily-formed committee without blinking an eye. I owe you all much more than German chocolate!

I also would like to thank the other members of the 4π Group, some of whom I overlapped only briefly: Skip Vander Molen, Omar Bjarki, Robert Pak, Nathan Stone, Stefan Grevy, Mike Miller, and the wonderful REU students we've had over the years. Some of my long discussions with them, in particular Omar and Skip, have been among the most memorable times in my graduate career. And as is customary in acknowledgements, I would like to mention that I, too, worked many overnight shifts during problematic experiments.

What makes the NSCL such a unique place to matriculate is its unpresumptuous way of being the best without intimidating its students and visitors. My friends at other universities only wish they were so lucky. The support staff at the NSCL was just as dynamic and unwavering as it was purported to be in the acknowledgements of past graduate students, and many friendships were formed in the process.

I would like to thank Walt Benenson and Ed Kashy for not only sharing their ideas and enthusiasm for teaching but for cultivating my own interest. They were both valuable advisors to a young apprentice full of energy, and I hope I can emulate some of the things I learned from them.

Ted Forringer literally has been by my side as a friend, roommate, and fellow graduate student since Day 1 at MSU. It is astonishing to sit back and think about all of the things we have been through together and all of the times one of us was there when the other one was in need. He and I have grown so much, together and apart and together, that I cannot imagine how I would have gotten to the point of

typing my acknowledgements without him. I only hope that it doesn't end with my graduation, because I would never find someone to replace him. Also, my fellow graduate students at MSU, in particular my office mates Erik, Jenny, and Dan, are very appreciated. Through no fault of their own they were subjected to my ongoing banter. I only hope I was at least half as good of a listener as they have been.

I would like to thank my family: my parents, my sister Shelline, my grandparents, and my extensive set of relatives, all of whom lofted me above their heads and made me feel like the center of attention, providing some of the motivation to continue climbing. I thank my parents especially, for supporting and paying for 12 years of piano lessons. I used to joke that I was studying physics only to finance my budding music career. Instead, what I now get from music is the feeling that my artistic creativity has not been compromised by my choice of profession. I am indebted to my parents for that, for helping me to become the well-rounded person I am.

Finally, I owe so much to Katrina Shields that by listing her here I have already understated her role. Perhaps a special section is in order! Instead of trying to list everything she has done to help me complete my graduate career, I will simply say that, more than any other non-physics person I've known, she makes me feel like I'm doing something extraordinary and valuable. Her unbelievable patience and tolerance of my hectic schedule and my inexplicable mood swings will be recompensed for the rest of our lives. And to my cat, Ally McBeal, for watching me write this beast and for resting with me on the in-between days.

CONTENTS

LIST OF TABLES

LIST OF FIGURES

Chapter 1

Introduction

This thesis, entitled "Transitions of Collective Flow Observables at Intermediate Energies," can be classified as a study of the nuclear equation of state. The connotation of *equation of state* when used in nuclear physics is the same as when used in thermodynamics, *i.e.,* the relationships between pressure, temperature, density, and any other dynamic variables. The nuclear equation of state (EOS) is studied in this thesis by comparing experimentally measured variables obtained from detecting the charged fragments of nuclear collisions with the predictions of theoretical models and calculations. Specifically, transitions in these measured variables, or *observables*, are particularly useful because their comparison to theory is less-hindered by unavoidable experimental biases and irrelevant qualities of the theory itself. The two observables used in this thesis, *directed flow* and *elliptic flow*, are both types of "collective flow," ordered motion characterized by the strong correlation between particle positions and momenta. Directed and elliptic flow both relate to particles emitted from the centers of nuclear collisions, where compressed nuclear matter leads to higher temperatures and densities. Therefore, these observables are well-suited for studying the EOS. The data set used primarily in this thesis is ^{197}Au+^{197}Au at incident energies between 25 and 59 MeV/nucleon. Au+Au is the system of choice because of large system

size (A=394) approximates infinite nuclear matter. Other data sets are included for studying the influence that system mass has on these observables.

In this chapter we will introduce the nuclear EOS in the context of the present status of nuclear physics. In particular the nuclear compressibility, a parameter of the nuclear EOS, is discussed. Then, some important traits of nuclear matter will be presented, along with the influence these traits have on EOS studies. Finally, we will define and discuss the transitions in directed and elliptic flow that are studied in the remaining chapters.

1.1 Nuclear Physics: Introduction and Status

The science of nuclear physics concerns itself with the properties of "nuclear matter," which makes up the massive centers of the atoms that account for 99.95 percent of the world we see around us. The main properties under investigation are the structure of nuclei and the interaction between nucleons (protons and neutrons), as well as the structure of nucleons themselves. Nuclear physics also explores the nuclear reactions that fuel the stars, including our Sun, which provides the energy for all life on Earth. The field of nuclear physics has existed for less than one hundred years, as Rutherford did not discover the atomic nucleus until 1911, the same year that superconductivity was discovered and atomic crystal structures were first observed.

At its core, research in nuclear physics is a quest for knowledge as well as a search for understanding, and its reach extends from the very small to the very large. Figure 1.1, produced in 1999 by the Committee on Nuclear Physics, established by the Board on Physics and Astronomy of the National Research Council [1], shows the various ways that nuclear physics enters into scientific research over the entire range of established lengths. Nuclear physics not only advances the frontiers of knowledge but also makes remarkable contributions to the needs of society, such as nuclear energy

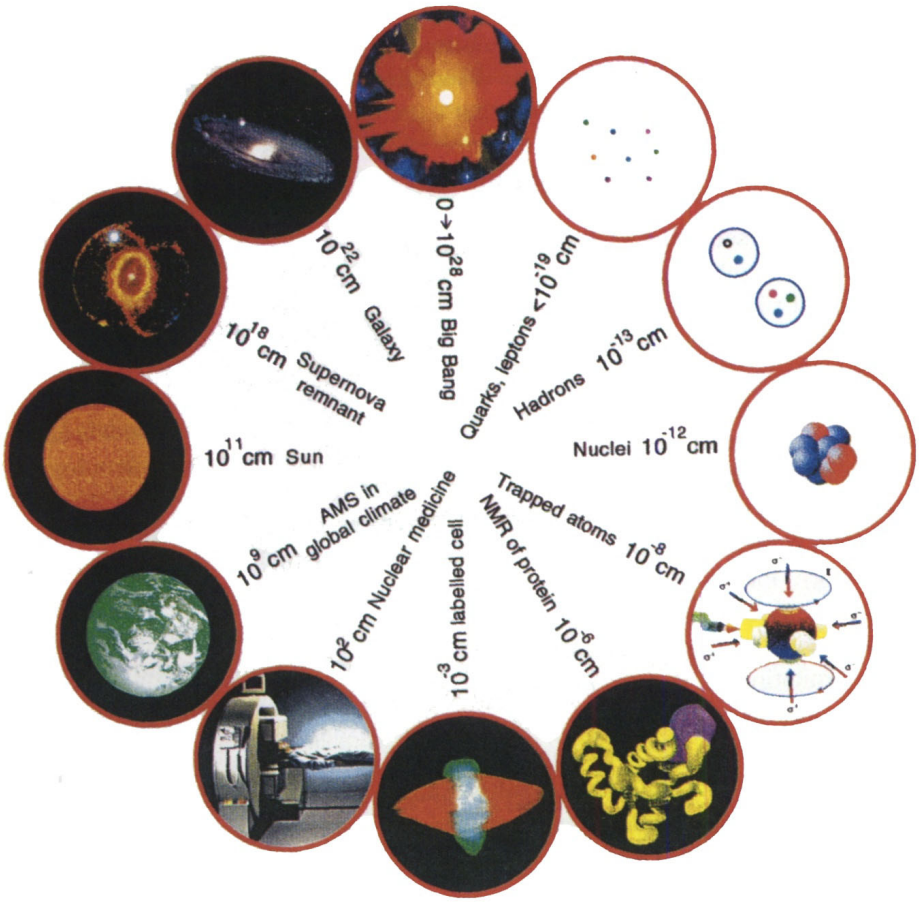

Figure 1.1: An illustration of the way in which nuclear physics enters into our world at different length scales. Taken from Ref. [1].

and nuclear medicine.

The current realm of nuclear physics is quite extensive, and some recent developments provide strong momentum as the field moves into the next century. In 1999, researchers at Berkeley's 88" Cyclotron discovered element $^{293}118$ [2] by increasing the mass of the projectile (that is fused with ^{208}Pb) from $A = 70$ to $A = 86$, far beyond what had been deemed viable and opening the window to even heavier nuclei. The result has yet to be reproduced at GSI heavy-ion research laboratory in Germany. Also in 1999, the Relativistic Heavy Ion Collider at Brookhaven performed its commissioning run and soon will be delivering beams to the four experimental devices hoping to detect and study the quark-gluon plasma [3]. Of local interest,

the Committee on Nuclear Physics has endorsed an ISOL (Isotope Separation On-Line) facility, which pending financial support will be built in this decade, possibly at Michigan State University. And numerous other recent advances in nuclear structure, nuclear astrophysics, and nuclear reactions paint a positive picture for the advances to be made in the coming years.

The 1999 Committee on Nuclear Physics identified four major priorities for the next decade, presented here as a matter of general interest:

1. Study of the quark-gluon structure of matter as well as the structure of hadronic matter at increasing energy densities;

2. Construction of a high-intensity accelerator facility for producing radioactive beams to study exotic nuclear matter;

3. Investment in instrumentation for research, including future upgrades of detector systems at both large and small laboratories; and

4. Evaluate research priorities through the continued formation of National Science Advisory Committees (NSAC) at regular six-year intervals.

1.2 The Nuclear Equation of State

When two ^{197}Au nuclei collide with enough energy to overcome the Coulomb repulsion between them, a system of 394 nucleons is formed for a very short time ($t \sim 10^{-22}$ s), occupying a volume of 10^{-36} cm^3. Despite its miniscule dimensions, the tiny laboratory of the Au+Au collision is nearly the largest that can be created on Earth. However, nature also provides nuclei of virtually infinite size in the form of neutron stars, which are typically 10^{16} cm^3 and contain $\sim 10^{55}$ nucleons. While observational astronomy can aid in understanding the behavior of a neutron star as a whole, such

as its rotational speed or its electromagnetic spectrum, much of what is learned from finite nuclei is crucial in explaining the properties of such infinite matter. For example, knowledge of the nature of the nucleon-nucleon force, the role of many-nucleon interactions, collective excitations, and the nuclear equation of state all rely on measurements made at terrestrial accelerator laboratories.

Nuclear matter is a uniform medium in which pointlike nucleons interact via a realistic two-body interaction; the electromagnetic effects are not included. In the absence of repulsive Coulomb forces, the ground state of nuclear matter is a uniform liquid having equal numbers of protons and neutrons [4] with a density of about 2.5×10^{14} g/cm^3 (0.16 nucleons per fm^3). In reality, a liquid of equally abundant protons and neutrons cannot exist because of its prohibitively large Coulomb energy. However, a heavy nucleus such as ^{197}Au can be seen as a stable, small drop of nuclear matter, even though its density is not uniform. Furthermore, some of its properties can be related to those of infinite nuclear matter, the most encompassing of which is the nuclear equation of state.

An equation of state is a relationship between the pressure (or energy per particle), temperature, and density of the matter under consideration. Atomic gases, for example, are described very well by the ideal gas law, which can be put in the form

$$P(r) = \frac{k}{m}\rho(r)T(r) \ , \tag{1.1}$$

where k is a constant, m is the mean molecular weight, $P(r)$ is the pressure, $T(r)$ is temperature, and $\rho(r)$ is the density of a sphere of radius r. While the ideal gas law is convenient and simple, candidate expressions for the **nuclear equation of state (EOS)** are more lengthy and often times require large approximations or extremely small amounts of nuclear matter in order to be used. Two typical examples of nuclear

EOS, included only for demonstration, are

$$P = \sum_{\tau} \rho_{\tau} \left[\frac{2}{3} T J_{3/2}(\eta_{\tau}) / J_{1/2}(\eta_{\tau}) + V_{\tau}^{0} + \frac{1}{2} b^{2} V_{\tau}^{1} + V_{\tau}^{2} \right]$$

which is determined from the two-body interaction using ground state properties [5], and

$$P = \frac{g_s - 1}{2 g_s} v(0) \rho^2 + kT \left[1 - \frac{3}{2} \frac{\rho}{m} \frac{\partial m}{\partial \rho} \right] \sum_{n=1}^{\infty} \tilde{B}_n \rho^n$$

which includes the Skyrme interaction and Hartree-Frock theory [6]. While both expressions for the pressure contain T and ρ, the functional dependence of P is quite complex. Though a theoretical analysis of the various EOS is beyond the scope of this thesis, the reader is referred to Refs. [7, 8] for discussions of the status of EOS theories.

A schematic way of representing an equation of state is a *phase diagram*, in which areas of a two-dimensional plot of EOS variables correspond to different physical states of the medium. Figure 1.2 is a highly schematic graph of the phases of nuclear matter, with temperature plotted *vs.* baryon density (normalized by ground-state density, ρ_0). The graph shows three distinct phases of nuclear matter. The *liquid* phase, which exists below about $T = 20$ MeV, is the phase for normal nuclei. Nuclear matter is expected, theoretically, to undergo a transition from a liquid to a *gaseous* phase at densities lower than $\rho_{\rm nm}$. The first-order liquid-gas phase transition, represented by the black border around the liquid phase, has been studied extensively but has yet to be fully characterized. At sufficiently high temperature and density, a transition from normal hadronic matter to a *quark-gluon plasma* phase is expected due to an increase in the degrees of freedom among the constituents. The nature of the hadron-quark/gluon phase transition (*i.e.,* whether it is first-order or second-order) is not known and will be one of the interesting subjects studied at RHIC [9].

Also drawn in Figure 1.2 is the evolution of the universe as a downward trajectory alongside the vertical axis of the phase diagram. From the time of the Big Bang,

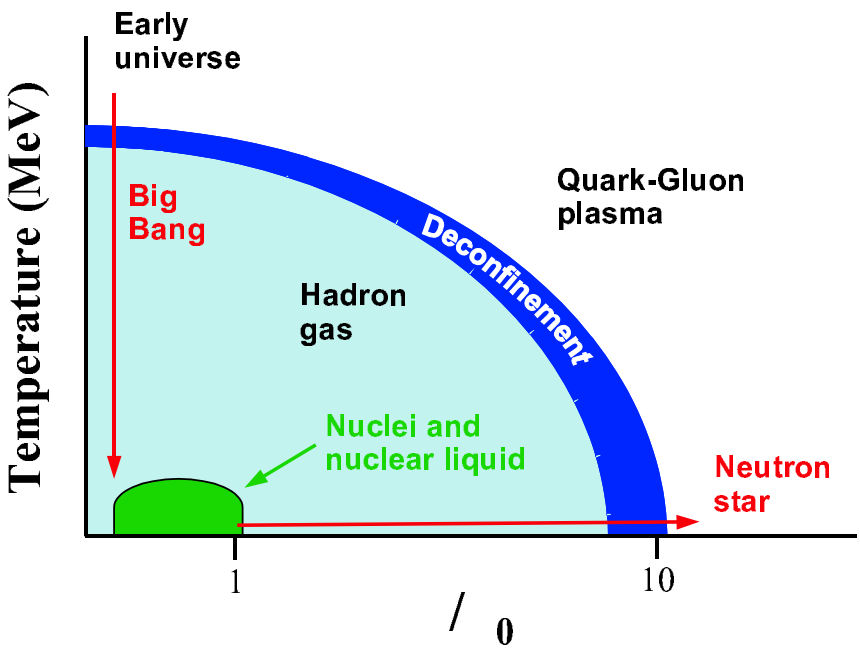

Figure 1.2: Phase diagram of nuclear matter. The three distinct phases are the liquid phase (green), the hadron gas phase (light blue), and the quark-gluon plasma phase (white). The evolution of the universe is indicated by a downward trajectory along the temperature axis, and neutron stars are thought to be at very low temperatures.

the early universe cooled as it expanded. For the first microseconds, the temperature was at least hundreds of MeV and matter existed as a quark-gluon plasma. The matter of the early universe was dominated by photons, and as the universe cooled, the quark-gluon plasma merged into hadrons (such as nucleons). If this transition was first-order, than quarks came together as hadrons in the same way that water forms rain drops. The form of the nuclear EOS at these phase boundaries is especially interesting to experimentalists and theorists alike.

One way to probe the EOS is by modeling the interactions between nucleons in a nuclear collision with a theory that treats the inter-nucleon potential as two separate pieces: a *mean field*, which represents the long-range, collective influence of all the nucleons on a single nucleon; and nucleon-nucleon scattering, which incorporates the hard collisions among the nucleons. The Boltzmann-Uehling-Uhlenbeck (BUU) model [10], used substantially in this thesis, implements an inter-nucleon potential

with mean-field and collision terms; see Sec. 4.4 for a thorough description of the BUU model.

1.2.1 Nuclear Compressibility

In order for a theory of the nuclear EOS to be valid, it must reproduce the empirical properties of nuclear matter. These properties include:

1. *saturation density*, which is the maximum density of nucleons in finite nuclei. The commonly accepted value is $\rho_0 = 0.16 \pm 0.02$ nucleons/fm^3.

2. *binding energy per nucleon*, which can be determined by using a nuclear mass formula that includes volume and surface terms. From studies made on finite nuclei, $E_B = 16 \pm 1$ MeV.

3. *mean free path*, which is related to the complex part of an optical model potential and signifies the distance a nucleon can travel before undergoing a collision. The knowledge of the mean free path λ for infinite nuclear matter is poor because, in a nucleus, λ is mostly determined by surface effects.

An empirical property that is often used to characterize the equation of state of nuclear matter in its ground state is the **nuclear compressibility** K, which is a measure of the stiffness of nuclear matter against changes in density. Nuclear compressibility is analogous to the inverse of the bulk modulus in solids that characterizes variations of the volume of a material as a function of the applied pressure [11].

In terms of equation of state variables,

$$K = 9\left[\frac{d}{d\rho}\left(\rho^2 \frac{dE_B}{d\rho}\right)\right]_{\rho=\rho_0} \tag{1.2}$$

where K is evaluated at the saturation density, ρ_0. It is also conventional to express K in terms of the *Fermi momentum*, which is the maximum value of a nucleon's

momentum in a free Fermi gas. The Fermi momentum[1] k_F can be expressed in terms of ρ_0:

$$k_F = \left(\frac{3\pi^2}{2}\rho_0\right)^{1/3} = 1.33 \pm 0.05 \text{ fm}^{-1} \tag{1.3}$$

and the corresponding expression for the compressibility is [4]:

$$K = k_F^2 \left(\frac{d^2 E_B}{dk_F^2}\right)_{\rho=\rho_0} \tag{1.4}$$

K is the slope in the variation of binding energy per nucleon as a function of k_F. The value of K is of great practical interest because it significantly influences the extrapolation of the nuclear EOS from $\rho = \rho_0$ to larger ρ [12]. It is worthwhile to stress that K corresponds to the compressibility only when $\rho \approx \rho_0$.

Several techniques for determining K have been employed. The first and most common method is to excite the isoscalar giant monopole resonance in nuclei [13], since the resonant frequency is directly related to the compressibility. However, there are inherent difficulties in using a nucleus' breathing mode, such as the influence of surface effects on the resonant frequency. Another method for finding K is to use mass formulas that involve thermodynamic variables [14]. If certain assumptions are made about the density and pressure, then measurements of the nuclear size and mass can lead to good estimates of K. This is also somewhat problematic, because the value of K is very dependent on the structure of the mass formula.

In this thesis, K is the EOS parameter of interest. The Boltzmann-Uehling-Uhlenbeck (BUU) model, presented in Sec. 4.4, determines values for K based on the model's implementation of the nuclear mean field; see Equations 4.4 and 4.5. By using the BUU model to generate quantities for comparison to experimental data, values for K can be inferred.

[1]Here, the wave number k_F is called the "Fermi momentum" in keeping with convention, despite its units of inverse length. The value for k_F at ρ_0 corresponds to $p_F = 2.91 \times 10^{-15}$ MeV/c (from $p = \hbar k$).

1.2.2 Neutron Stars

As mentioned at the beginning of this Section, much of what is learned from EOS studies of finite nuclei is crucial in explaining the properties of astrophysical objects. These properties include the maximum mass and radius of a neutron star and the densities needed for supernova explosions to occur. The EOS is also important in the process of big-bang nucleosynthesis. As an instructive example, the relationship between the EOS and structural properties of neutron stars are discussed in this Section.

A neutron star is the cosmological equivalent of a giant nucleus. Neutron star masses are roughly equal to a solar mass ($M_\odot$), packed into a sphere 10-20 km in diameter. A neutron star is formed when atoms are literally crushed out of existence by intense gravitational forces which cause protons and electrons to combine into degenerate, unbound neutrons. The mass and radius of the star is mostly limited by the counterplay between gravity and the nuclear compressibility (K), and values of the maximum mass and radius obtained from theory studies have been shown to depend directly on the value of K [15].

Figure 1.3(a) shows how the density profile of a neutron star of mass $M_{\rm max}$ depends on K, as calculated from simple assumptions about the binding energy of neutron-rich matter [16]. The curves represent different values of the nuclear compressibility, and the area below the curve is the fraction of the star's total mass which falls below a given density. As K decreases, larger amounts of the mass are seen to be at higher density. This is an expected trend, since a very high compressibility would lead to a rigid and nearly constant density profile.

Calculations of $M_{\rm max}$ vary greatly depending on the parameters of the nuclear EOS. Figure 1.3(b) shows $M_{\rm max}$ as a function of the neutron compressibility[2] for

[2]The *neutron compressibility* is related monotonically to K, the compressibility of symmetric nuclear matter, by means of the neutron-to-proton ratio. As expected, for ratios near 1, $K_N \approx K$.

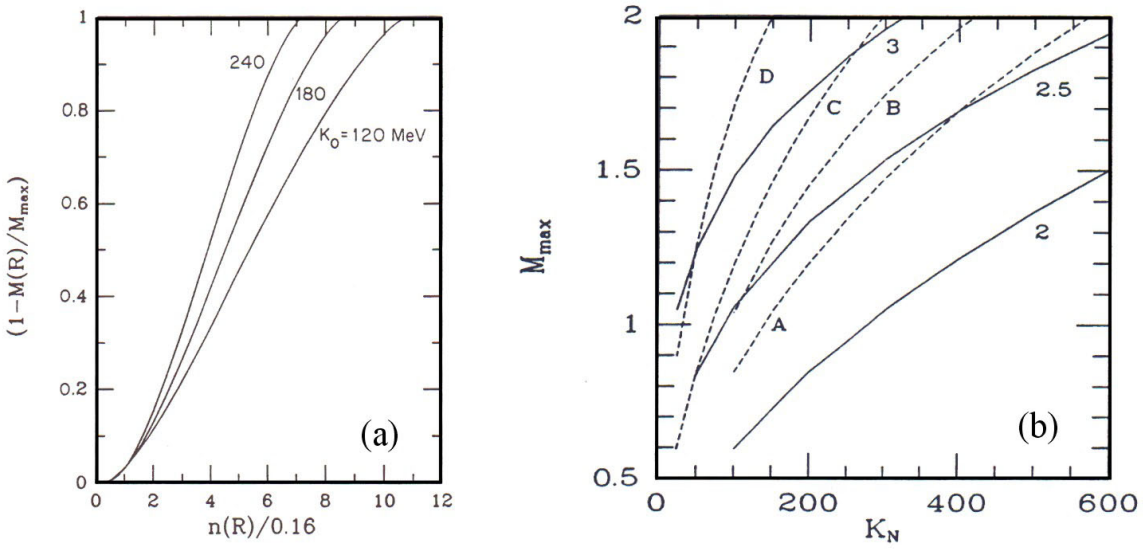

Figure 1.3: (a) Fraction of a neutron star's total mass which falls below a given density for three different values of the nuclear compressibility [16]. (b) Maximum mass of neutron stars plotted as a function of the neutron compressibility for several different assumptions about the nuclear EOS [15].

several different EOS [15]. For compressibilities around 200 MeV, $M_{\max}$ is seen to vary by more than a factor of 2, depending on the EOS. Of course, some EOS can be ruled out by observational astronomy, since known neutron stars have been observed to be as large as 1.5 $M_{\odot}$.

While a detailed explanation of the role that the nuclear EOS plays in neutron stars is beyond the scope of this thesis, it is clear that constraints can be placed on their characteristics by studying the nuclear compressibility. It is also worth noting that observational astronomy might be useful for constraining the nuclear EOS itself, although the properties of neutron stars, such as density profile, neutron-to-proton ratio, and even the recent suggestion of a quark-gluon plasma core (so-called *strange stars*, see Ref. [17]) make extracting useful information directly from neutron stars difficult.

1.3 Properties of the Nuclear Medium

The process of extracting information about the nuclear equation of state by comparing theoretical calculations of nuclear collisions to experimental data is obscured by secondary features of nuclear matter. In particular, the behavior of particles in the nuclear medium (*i.e.,* the "material" composed of nuclear matter) differs from their behavior in free space, leading to complications in the theory-data comparison. The differences between the nuclear medium and free space include:

1. the effective pion mass in nuclear matter, which increases slightly as the nuclear density ρ/ρ_0 increases;

2. the peak energy and width of nucleon resonances in nuclei, which are affected slightly by the Fermi motion of the in-medium nucleons;

3. the cross sections of pion-nucleon, kaon-nucleon, etc. interactions in-medium show enhancements when compared to free space.

A quality of nuclear matter which plays a role at intermediate energies is the reduction in the in-medium nucleon-nucleon cross section, $\sigma_{\rm nn}$. The main reason for a reduction in $\sigma_{\rm nn}$ compared to free space is the *Pauli Exclusion Principle*, which disallows certain low-momentum processes from occurring [19]. The result is fewer nucleon-nucleon collisions in areas of high nucleon density (such as the interiors of heavy nuclei).

The effect of a reduced cross section is substantial when trying to extract EOS information from nuclear reactions, since nucleon-nucleon collisions are a dominant part of the reaction. In intermediate-energy heavy ion collisions, most of the nucleon collisions scatter nucleons at the surface of the initial Fermi spheres. Therefore, the nucleons are often treated as hard spheres in theoretical models. The functional form

of the density-dependent reduction in $\sigma_{\rm nn}$ is commonly written

$$\sigma_{\rm nn} = \sigma_{\rm free}\left(1 + \alpha\frac{\rho}{\rho_0}\right) \tag{1.5}$$

[18], where $\sigma_{\rm free}$ is the nucleon cross section in the vacuum, and α is a parameter between 0 and -1. Eq. 1.5 is not intended to be capable of representing the in-medium cross section at all densities; for example, it is clear from inspection that a density of $\rho = 4\rho_0$ limits α to values above -0.25. However, the representation has been used with success by numerical models such as BUU (presented in Sec. 4.4) in accounting for the reduced cross-section at intermediate energies and near ρ_0.

1.4 Collective Flow in Nuclear Collisions

A primary motivation for experimental studies of nuclear collisions is the hope that measured quantities can be compared to and modeled by theory unambiguously and that this comparison leads to better understanding of the empirical properties of nuclei or nucleons themselves as well as astrophysical (stars) and cosmological (Big Bang) entities. As discussed in Sec. 1.2, the empirical property of interest in this thesis is the compressibility of nuclear matter at normal nuclear density ρ_0. The value for the compressibility has direct consequences on the mass limit of neutron stars as well as the stability and lifetimes of supernovae.

When two nuclei collide and are compressed to densities higher than ρ_0, a flow pattern will develop as the system subsequently expands. During the decompression stage, the directions and speeds of the constituent particles are influenced by pressure gradients, *i.e.,* particles tend to flow to regions of lower pressure. This pressure-dependent correlation between particle positions and momenta is known as **collective flow**. First proposed in the 1950's [20] and experimentally discovered in the mid-1980's [21], collective flow has been studied at beam energies ranging from

tens of MeV/nucleon to hundreds of GeV/nucleon for various emitted particle types, including nucleons, light charged particles, pions, kaons, and lambdas.

In classical physics flow is described in the language of hydrodynamics, where the simple conservation laws (momentum, mass, energy) are linked to fundamental properties of the fluid, such as the equation of state and viscosity. In nuclear physics, the approach is similar: the final states of particles are linked to dynamical properties of the collision, such as the in-medium nucleon cross section and the nuclear compressibility. In addition to contributions from random thermal motion and the initial kinematics of the collision, the contribution of collective flow to the final states is modeled by so-called *transport models* which propagate particles through space and time as they undergo interactions. The integrity of the model depends on its treatment of collective flow.

Primitively speaking, collective flow is a measure of the transverse motion imparted to particles and fragments during the collision of two nuclei. The *transverse* nature of collective flow is its most alluring quality to experimentalists, because it enables the measurement of flow for particles in different domains of the collision. This is best exemplified in the geometry of the Nuclear Fireball Model, proposed by Westfall *et al.* in the mid-1970's [23] and illustrated in Figure 1.4. In the Fireball Model, nuclear collisions with non-zero impact parameter consist of three domains: the *participant* piece from the overlap region of the nuclei, and two *spectator* pieces from the projectile and target portions which do not overlap. Because the longitudinal velocities of the three domains are different (see Figure 1.4), particles from the domain of interest can be selected by their longitudinal velocity components without interfering in the measurement of their collective transverse motion. In this thesis, collective flow of the participant region, where the compression is expected to be the largest, is the quantity being studied.

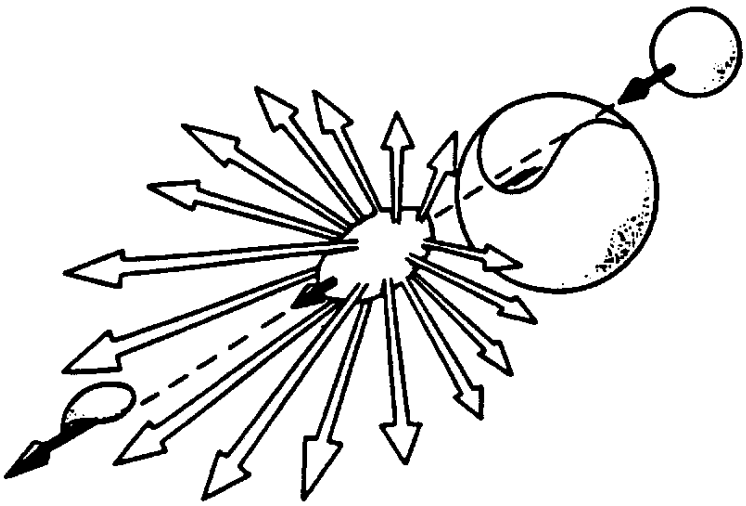

Figure 1.4: The Nuclear Fireball Model proposed by Westfall *et al.* [23]. The participant region formed by the overlap of the colliding nuclei moves at a longitudinal velocity between the two spectator region velocities, and the three "sources" can be treated as three separate pieces.

Generally, there are three types of collective flow which are discussed in nuclear collisions, termed *radial flow*, *directed flow*, and *elliptic flow*. **Radial flow**, or radial expansion, which is not studied in this thesis, arises in central collisions and is characterized by increased yields in the kinetic energy spectra of particles emitted near $\theta_{\mathrm{c.m.}} = 90^{\circ}$ relative to the beam axis. The existence of radial flow indicates that kinetic energy spectra differ from the expected spectra of a compressed thermal fluid expanding outwards. In intermediate-energy collisions, radial flow has been shown to account for as much as half of the emitted particles' energies [24], which is incompatible with the assumption of a purely thermal distribution. The existence of radial flow has implications in the temperature gradient of hot nuclear matter as well as the effects of relativistic hydrodynamics; for a recent summary of work to date, please see Reisdorf and Ritter, Ref. [25].

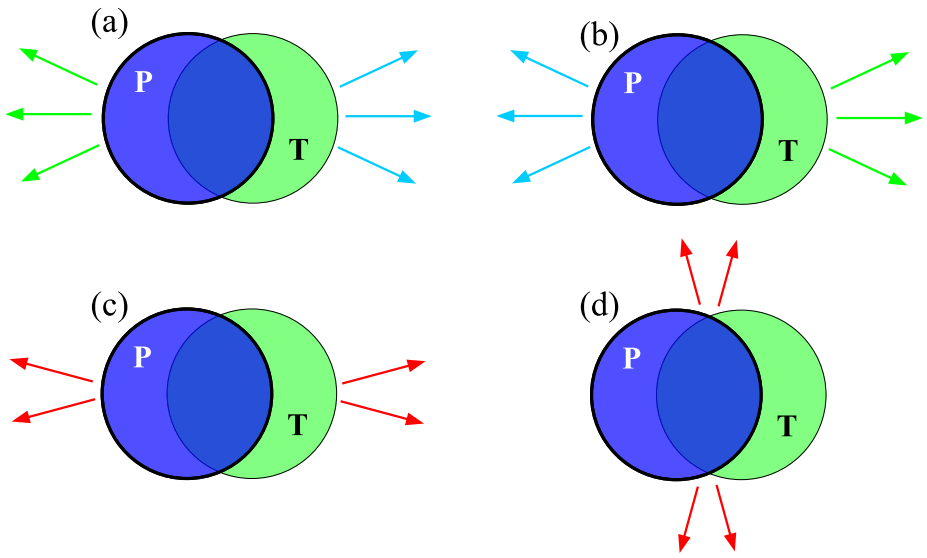

Figure 1.5: The four major types of azimuthal anisotropies, viewed in the transverse plane and looking in the direction of the beam. The target is denoted by T and the projectile by P, and blue (green) arrows indicate the preferred emission directions of projectile-like (target-like) fragments. (a) Negative directed flow; (b) positive directed flow; (c) in-plane elliptic flow; and (d) out-of-plane elliptic flow.

Directed Flow

The remaining two types of collective flow, both of which are studied in this thesis, are illustrated schematically in Figure 1.5. **Directed flow**, also called "in-plane" or "sidewards" flow in the literature, refers to the preferential emission of particles within, and to a particular side of, the *reaction plane*. (The reaction plane is defined as the plane which contains the beam axis and a line joining the centers of the two nuclei.) Stated another way, directed flow is the deflection of nucleons and fragments to finite scattering angles as a result of nontrivial interactions during the collision. The transverse components of the particles' momenta projected into the reaction plane are used to quantify directed flow.

Figure 1.6 demonstrates the preferential emission of particles in the reaction plane, characteristic of directed flow. In Figure 1.6(a), two heavy nuclei in the center of mass frame are incident upon each other with non-zero impact parameter (*i.e.*, a noncentral

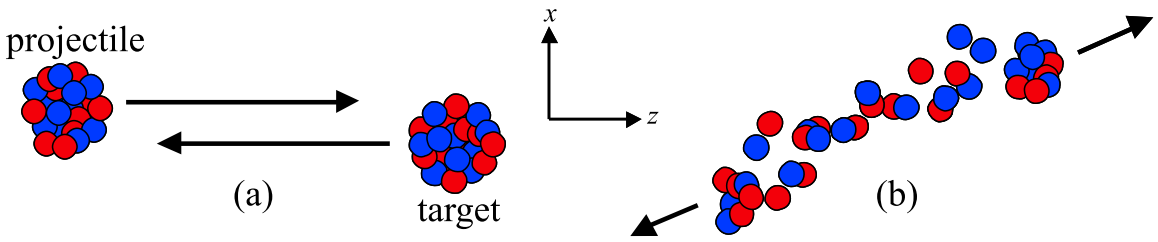

Figure 1.6: Schematic representation of positive directed flow in the reaction plane. Two nuclei are incident in the center of mass frame collide, and the overall repulsive interaction causes the flow of nucleons to positive scattering angles.

collision), and the reaction plane is taken as the plane of the paper. After the collision, projectile (target) nucleons are directed mostly in the $+x$ ($-x$) direction, illustrated in Figure 1.6(b). In the transverse plane this corresponds to azimuthal Φ distributions which are peaked at 0° (180°) for projectile-like (target-like) remnants. In collisions of identical nuclei such as Au+Au, the Φ distribution for particles at forward angles in the center of mass frame must be totally anti-symmetric to the backward-angle Φ distribution.

As mentioned above, directed flow of the participant region, where the compression is expected to be the largest, is the quantity of interest. Particles from the participant region are selected by making analysis cuts on the center of mass *rapidity*, $y_{\rm cm}$, which is a Lorentz scalar and a measure of a particle's longitudinal motion. The strength of directed flow usually is measured by plotting the average transverse momentum of all particles projected on the reaction plane ($|\mathbf{p}^\perp| \cos\Phi$) as a function of rapidity and by taking the slope of this function at $y_{\rm cm} = 0$:

$$F = \left. \frac{d\langle |\mathbf{p}^\perp| \cos\Phi \rangle}{dy} \right|_{y_{\rm cm}=0}, \tag{1.6}$$

where F is the strength of the directed flow. A more thorough explanation of how to measure directed flow is presented in Sec. 4.3.2.

Elliptic Flow

Whereas directed flow is anti-symmetric with respect to the Φ distributions for forward rapidity ($y_{\rm cm} > 0$) and backward rapidity ($y_{\rm cm} < 0$), elliptic flow has the same distribution in both rapidity regions, at least for symmetric systems. **Elliptic flow** refers to the anisotropy of the Φ distribution at midrapidity and its value indicates whether or not particle emission is *in-plane* or *out-of-plane*. Azimuthal distributions which are peaked at 0° and 180° exhibit predominantly in-plane emission, while Φ distributions peaked at $\pm 90°$ signify out-of-plane emission. The term *elliptic flow* has replaced old naming conventions such as "squeeze-out," "rotational motion," or "anisotropic flow" because the shapes of Φ distributions at midrapidity resemble ellipses with a major axis along the x-axis (in-plane emission) or y-axis (out-of-plane emission).

Out-of-plane elliptic flow, which can occur in non-central collisions, is an interesting phenomenon which has been observed at incident energies ranging from 100 MeV/nucleon to ~4 GeV/nucleon. Out-of-plane emission at midrapidity depends primarily on two factors: the pressure built up in the compression stage compared to the energy density, and the passage time for removal of the projectile- and target-like spectators of the Fireball Model. If the participant region emits particles at an early stage of the collision, the spectator pieces may still be close enough to cause pressure gradients in the out-of-plane direction. Figure 1.7 illustrates the formation of the compression region in a noncentral nuclear collision and the subsequent emission of particles from the midrapidity participant region.

Since the midrapidity Φ distribution due to elliptic flow is symmetric about both the reaction plane and the plane at $\Phi = \pm 90°$, the four-fold symmetry resembles a $\cos(2\Phi)$ function. In fact, directed and elliptic flow can be treated as the first and

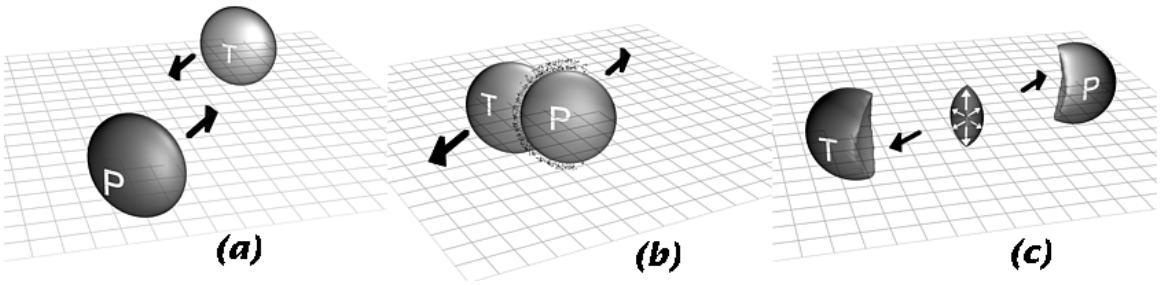

Figure 1.7: Schematic illustration of the collision of two Au nuclei and the resulting elliptic flow of the participant zone. Time shots are shown for an instant before the collision (a), early in the collision (b), and late in the collision (c). taken from Ref. [95].

second harmonics of a Fourier expansion of Φ:

$$F(\Phi) = c_0 + c_1 \cos(\Phi) + c_2 \cos(2\Phi) \ , \tag{1.7}$$

where the coefficients c_1 and c_2 correspond to the strength of the directed and elliptic flow contributions, respectively. See Section 5.3.1 for a thorough discussion of the use of a Fourier expansion when studying elliptic flow.

1.5 Transitions in Collective Flow at Intermediate Energies

Directed and elliptic flow are both robust observables for studying the hot and dense region of nuclear matter formed in the center of heavy ion collisions. Their strength rests in their simplicity; neither observable requires complex calculations or gross approximations. The most detailed part of the analysis is in the reaction plane determination, but, as discussed in Sec. 3.2, the method for determining the reaction plane is well-established.

One of the underlying objectives of science is to find experimental observables which can be compared unambiguously to theory. However, some complications arise

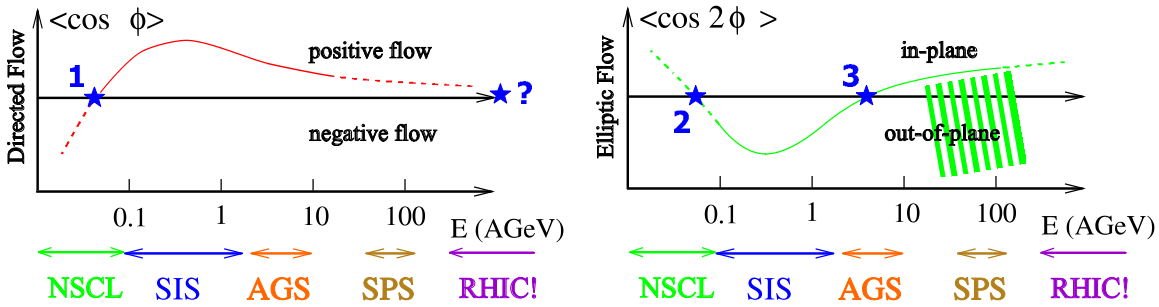

Figure 1.8: Schematic behavior of directed flow (left) and elliptic flow (right) as a function of the beam energy in the lab frame.

in the comparison between theoretical calculations and finite (non-zero) flow measurements. Finite flow values are difficult to compare to theory because

- the theory needs to incorporate experimental biases correctly, such as limited detector acceptance;
- the theory needs accurate fragment formation and (at high energies) particle production, since the collision produces a range of particle types; and
- the dispersion in the reaction plane affects the flow measurement, and correcting for dispersion increases the experimental value.

A promising and useful feature of both directed and elliptic flow is the existence of transitions between two forms of the observable. These transitions amount to measuring "zeroes" in the *flow excitation functions*, or the energy dependence of the flow variables. Measuring zero is mostly free from the difficulties inherent in the theory-data comparison for finite flow values [26].

Figure 1.8 is a schematic representation of the directed and elliptic flow excitation functions for nucleons over a wide range of beam energies. Dashed areas of the curves at higher energies represent studies that are currently underway or planned, and the dashed area in the NSCL energy regime represents the energy range studied in this thesis. The following transitions are believed to be present in the excitation functions,

indicated by stars (★):

1 transition from negative to positive directed flow in the NSCL energy regime;

2 transition from in-plane to out-of-plane elliptic flow in the NSCL and near the SIS energy regimes;

3 transition from out-of-plane to in-plane elliptic flow at AGS beam energies; and

? disappearance of directed flow in the SPS or RHIC energy regime.

The first two transitions are the objects of study in this thesis and will be explained in further detail in the subsections below.

Transition **3** in Figure 1.8 has been studied extensively the past couple years by experimental groups at the AGS. The most exciting results are from the E895 Collaboration, which measured the proton elliptic flow in Au+Au collisions for beam energies of 2−8 GeV/nucleon [27]. They found that the elliptic flow excitation function exhibits a cross-over at $\sim$ 4 GeV/nucleon. Furthermore, as shown in Figure 1.9(a), relativistic BUU calculations for two different equations of state indicate a *softening* of the equation of state in the AGS energy range. However, more data are needed to support this exciting finding.

The final transition is enumerated with a "**?**" because the existence of a directed flow transition in the SPS energy range is still uncertain. Figure 1.9(b) shows recent results of Pb+Pb collisions at 158 GeV/nucleon taken by the NA49 Collaboration at CERN [71]. The slope of the directed flow curve at midrapidity appears to be flat, corresponding to zero directed flow; however, points at backward rapidities are reflected measurements, perhaps giving a false impression. The possible existence of a zero in the directed flow excitation function is exciting, because it has been suggested as a signature of the quark-gluon plasma [28].

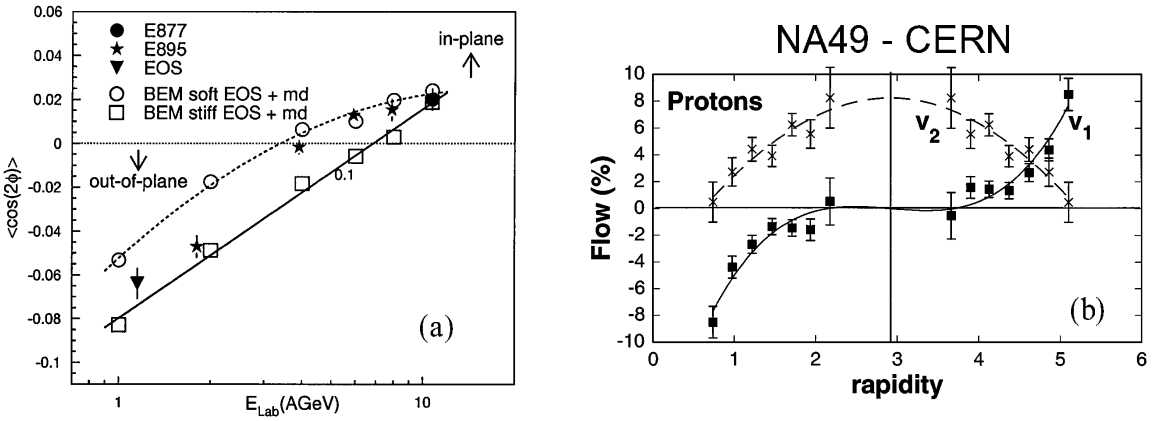

Figure 1.9: (a) Elliptic flow excitation function for Au+Au near transition **3**. Filled symbols represent experimental data. The dashed curve (open circles) and the solid curve (open squares) represent calculations for a soft and a stiff EOS, respectively [27]. (b) The rapidity dependence of the directed (v_1) and elliptic (v_2) flow for protons. The points below midrapidity have been reflected from the measurements in the forward hemisphere. Taken from the NA49 Collaboration [71].

The directed and elliptic flow transitions in Figure 1.8 represent fundamental changes in the emission patterns of protons and light fragments, and the beam energies at which these transitions take place can be probed by theoretical models, which in turn can be compared to data without taking into account some of the intricacies of the experimental setup.

1.5.1 Disappearance of Directed Flow

In intermediate-energy nuclear collisions, directed flow in the mean field approximation results from the combined effects of three quantities: an attractive nuclear mean field, the repulsive Coulomb potential, and the hard scattering processes governed by the in-medium nucleon cross section. The energy dependencies of these contributions determine whether the overall nature of the collision is attractive or repulsive for a particular system. Predominantly attractive scattering leads to negative directed flow, *i.e.*, projectile-like fragments orbit to the target side of the reaction plane. The opposite is true for a predominantly repulsive interaction, which was illustrated in

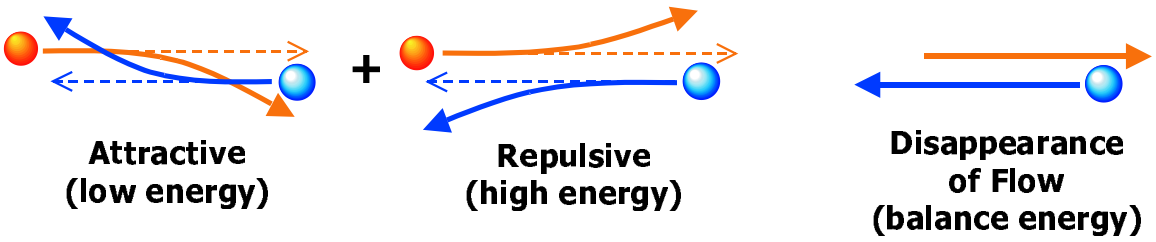

Figure 1.10: At the balance energy, attractive dynamics, dominant at low incident energies, cancel the repulsive interactions which dominate at higher energies.

Figure 1.6.

At incident energies around 10-20 MeV/nucleon, the nuclear mean field dominates the collision dynamics, resulting in mostly negative deflection. As the beam energy is increased, the mean field plays a reduced role, and hard repulsive scattering increases in importance. The disappearance of directed flow (corresponding to transition **1** in Figure 1.8) occurs when attractive and repulsive effects cancel each other. At that incident energy, termed the **balance energy**, the azimuthal distributions of projectile-like (target-like) fragments with respect to the reaction plane do not exhibit peaks at 0° (180°). This is illustrated in Figure 1.10. The balance energy for Au+Au is the subject of Chapter 4, and its utility in constraining the nuclear equation of state is presented therein.

1.5.2 Disappearance of Elliptic Flow

Transition **2** in Figure 1.8 corresponds to the change in the direction of preferred fragment emission from the compressed participant region. At energies below the **transition energy**[3], emission is primarily in the reaction plane (*i.e.* Φ distribution is peaked at 0°, 180°). Since such an in-plane enhancement is also produced in the de-excitation emission of a nucleus with a large angular momentum, this effect was

[3]Unlike "balance energy," which is a generally accepted term for the disappearance of directed flow, "transition energy" is somewhat new terminology. It was first used in 1997 by the FOPI group [66], but "onset of squeeze-out" and other conventions are still used.

called a "rotation-like effect" or "rotational flow" in early papers [29]. In higher-energy collisions, a maximum in the direction perpendicular to the reaction plane on both sides (formerly called squeeze-out) appears because the compressed matter in the interaction region can escape preferentially in directions unhindered by the presence of the projectile and target spectators.

The transition energy for Au+Au is one of the topics of Chapter 5. Also, the mass dependence of the transition energy is measured, and the transition energy for a light system is compared to published theoretical calculations.

1.6 Summary and Thesis Structure

The main objective of this thesis is to compare experimental measurements of transitions in collective flow observables to theoretical predictions in order to study the nuclear compressibility, since its value has direct consequences on the nuclear equation of state. The primary system being studied is ^{197}Au+^{197}Au, for various reasons outlined in Chapters 4 and 5. Lighter systems are analyzed for the purposes of understanding the effect of system mass and comparing to published calculations.

The balance energy for Au+Au is interesting because it extends the mass dependence of the balance energy by a factor of two, and because its existence has been questioned by theoretical studies. Au+Au also proves to be a useful system for separating the dual influence of the nuclear compressibility and the in-medium nucleon cross section on the balance energy. The transition energy for Au+Au presented in Chapter 5 has a very different value from previous experimental studies, and the transition energy for lighter systems is presented in hopes that it can provide a second way for collective flow to isolate the nuclear compressibility.

The following is a brief outine of the remainder of this thesis:

Chapter 2: Experimental details of the MSU 4π Array, with a special emphasis on

the reduction of raw data to meaningful physics quantities.

Chapter 3: Characterizing the events with impact parameter and reaction plane. Several corrections to the data are also discussed.

Chapter 4: Disappearance of directed flow for Au+Au with comparison to BUU calculations. The BUU calculations are used to quantify the role of the Coulomb interaction for heavy systems as well as isolate the nuclear compressibility for the first time using the balance energy.

Chapter 5: Elliptic flow transition from in-plane to out-of-plane emission for Au+Au as well as lighter systems. Comparison to isospin-dependent BUU calculations are made.

Chapter 2

Experimental Setup and Data Reduction

In order to make measurements of collective flow in nuclear collisions, a detector system must be chosen that can detect and characterize a large fraction of the emitted particles. This is especially true for the directed and elliptic flow study in this thesis because (a) the accuracy of the reaction plane determination is related to the number of detected particles; (b) both directed and elliptic flow depend on the impact parameter, which is related to event multiplicity and the summed transverse energy of detected particles; and (c) both observables involve particles emitted over a large angular range. Detectors with near-complete coverage such as the **MSU 4π Array** [30] are most suitable for studying flow at intermediate energies. At higher beam energies for fixed target experiments, detector systems may have very good coverage, even though they physically do not surround the target like the 4π Array, because the emitted particles are boosted forward more by the higher beam velocities. In this chapter, the parameters of the Au+Au experiment carried out for this thesis are presented. In particular, an emphasis is placed on the full procedure for converting 4π Array detector signals into meaningful physics quantities such as position and energy.

2.1 Beam and Target Parameters

The Au+Au collisions studied in this thesis were produced by colliding ^{197}Au beams with thin, stationary ^{197}Au foils located in the center of the MSU 4π Array. The ^{197}Au beams were accelerated by the K1200 cyclotron at the National Superconducting Cyclotron Laboratory (NSCL) by first stripping off between 35 and 44 electrons to create the high charge states needed. Over a five day experimental run, approximately 80 hours of active beam with intensities of approximately 10-100 electrical pA ($\sim 10^7$ Au nuclei per second) were delivered to the 4π experimental vault at incident energies of 21, 25, 29, 35, 40, 45, 50, 55, and 59 MeV/nucleon. Some of the energies were obtained by degrading a primary ^{197}Au beam in the A1200 beam analysis system without a significant loss of intensity.

The ^{197}Au beams were focused on round targets of ^{197}Au foils 1.5 cm in diameter at the center of the 4π Array. Targets can be switched conveniently without venting the detector's large vacuum chamber, and ^{197}Au foils of thickness 2, 6, and 19 mg/cm^2 were interchanged. (A 19 mg/cm^2 Au target is 10 μm thick.) Because the energy loss in the target is substantial for the energies used in this thesis, some of the incident beam's energy is lost as it passes through the target. Therefore, the effective beam energy is reduced by a small amount. This affects the kinematics of the collision, in particular the transformation to center of mass coordinates. Table 2.1 shows the effective ^{197}Au beam energies for the beam and target combinations used in the experiment.

2.2 The 4π Array

The MSU 4π Array [30], located in the N2 vault of the NSCL, is a powerful detector configuration which nearly completely surrounds the collision. The 4π Array is

Primary Beam Energy (MeV/nucleon)	Degraded Beam Energy (MeV/nucleon)	Target thickness (mg/cm^2)	Effective beam energy (MeV/nucleon)
29	25	2	24.5
29	N/A	6	28.2
45	35	19	33.1
45	40	19	38.3
45	N/A	6	44.5
50	N/A	19	48.4
55	N/A	19	53.5
59	N/A	19	57.6

Table 2.1: Effective ^{197}Au beam energies for all beam and target combinations used in this thesis.

a charged-particle detector, *i.e.,* gamma rays and neutrons are not identified. Its strength rests in three key traits:

- The underlying geometry is a 32-faced truncated icosahedron, as shown in Figure 2.1(a). This geometric configuration allows for detector modules to be packed close together, which provides nearly full coverage in the solid angle and reduces the amount of dead space between detectors.

- Most of the detector array is *logarithmic*, meaning particles in different energy ranges (and therefore different penetration distances in the detector) are identified by using information from different layers in the detector. This enables a wider range of particle types and energies to be characterized while still maintaining the 4π solid angle.

- The extensive electronics for the 4π Array are located very near the vacuum chamber, which minimizes signal losses due to long cables. The data acquisition system is built to accomodate high rates, and detectors are monitored during the experiment via a single ethernet cable between a vault computer and the

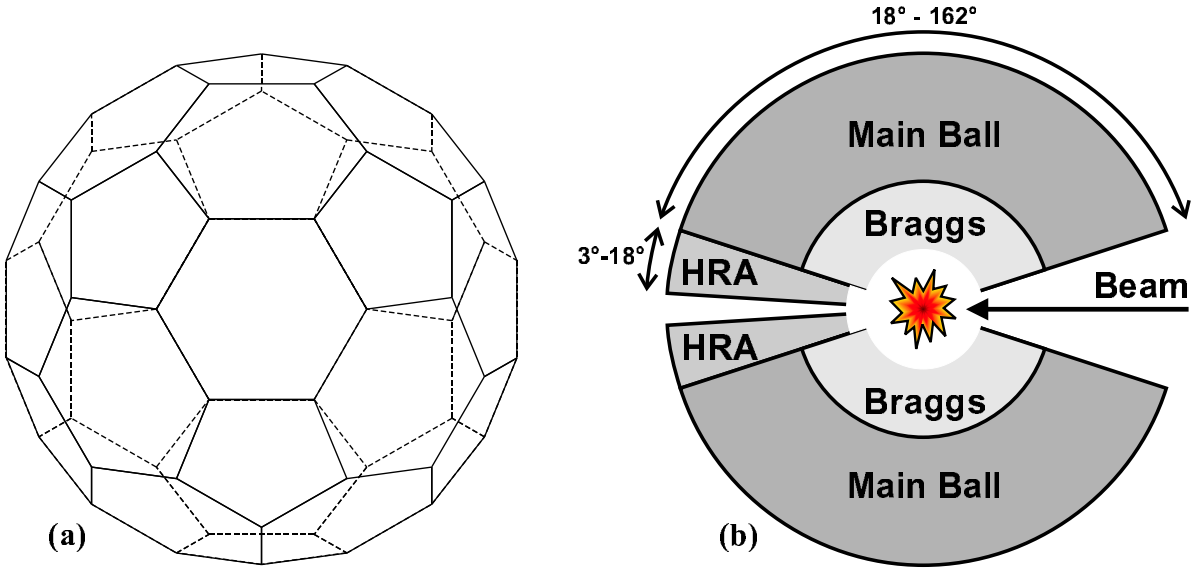

Figure 2.1: (a) Basic geometry of the MSU 4π Array. (b) Polar angles subtended by each of the detector subsytems used in this thesis.

users' area.

These qualities make the 4π Array a suitable detector system for experiments that require high statistics and a large acceptance for charged particles.

2.2.1 Detector Subsystems

For the data presented in this thesis, the 4π Array was operated in a configuration that includes three distinct detector arrays: the plastic scintillators of the Main Ball, known as phoswiches; Bragg curve gas detectors in front of the Main Ball scintillators; and the set of plastic scintillators of the High Rate Array.[1] The three detector subsystems are explained below. The entire detector system is housed in a large vacuum vessel two meters in diameter for which pressures of 2×10^{-5} torr were reached during the experiment. Figure 2.2 shows the 4π Array around the time of the Au+Au experiment from two different vantage points. In Figure 2.2(a) the beam enters from

[1]Three additional 4π Array subsystems are available but were not used: Maryland Forward Array, Zero Degree Detector, and the Iowa Forward Array. The 4π Array is also configured to run with PPAC detectors on the fronts of the Main Ball modules, although they presently are not installed.

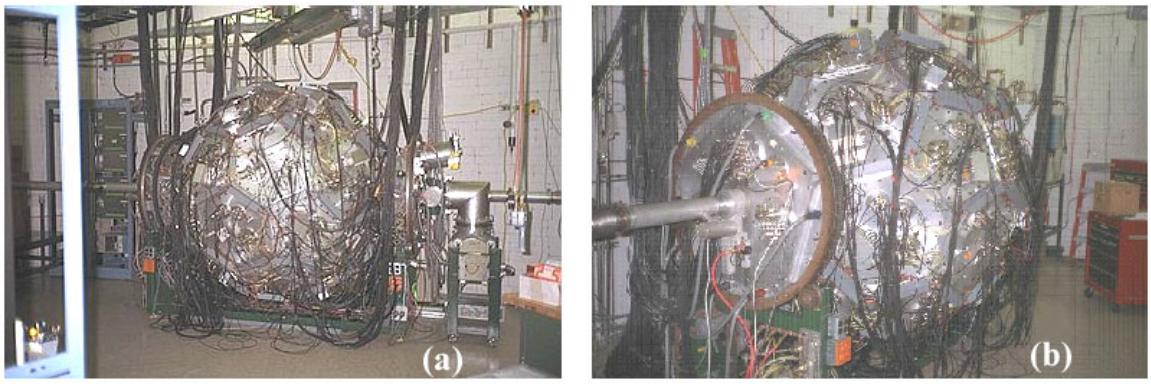

Figure 2.2: The 4π Array, located in the N2 vault of NSCL. (a) View of the array from the entrance to the vault. (b) View looking at the High Rate Array face of the detector.

the right side and exits on the left side through opposing pentagonal faces. Figure 2.2(b) shows the view from the exit side of the Main Ball. The exit face serves as the mounting plate for the High Rate Array.

Main Ball Phoswiches

The 4π Array is composed of 170 detectors in the Main Ball, distributed among twenty hexagonal and ten pentagonal modules. (The remaining two pentagonal faces of the truncated icosahedron are the entrance and exit faces.) Each hexagonal (pentagonal) module contains a subarray of six (five) two-layer, close-packed plastic scintillators, and the polar angles subtended by the array of ball detectors is $18^\circ \lesssim \theta_{lab} \lesssim 162^\circ$ (see Fig. 2.1). The individual detectors in the main ball are triangular pyramids which subdivide either hexagons (60°, 60°, 60°) or pentagons (72°, 54°, 54°). Each phoswich consists of a 3 mm thick layer of fast plastic scintillator followed by a 25 cm thick block of slow plastic scintillator, which is optically coupled to a photo-multiplier tube (PMT). Physical specifications of the phoswiches are given in Appendix A.

When a charged particle is incident upon the scintillator elements of a phoswich, light is produced [32], which is collected by the PMT and turned into a single current

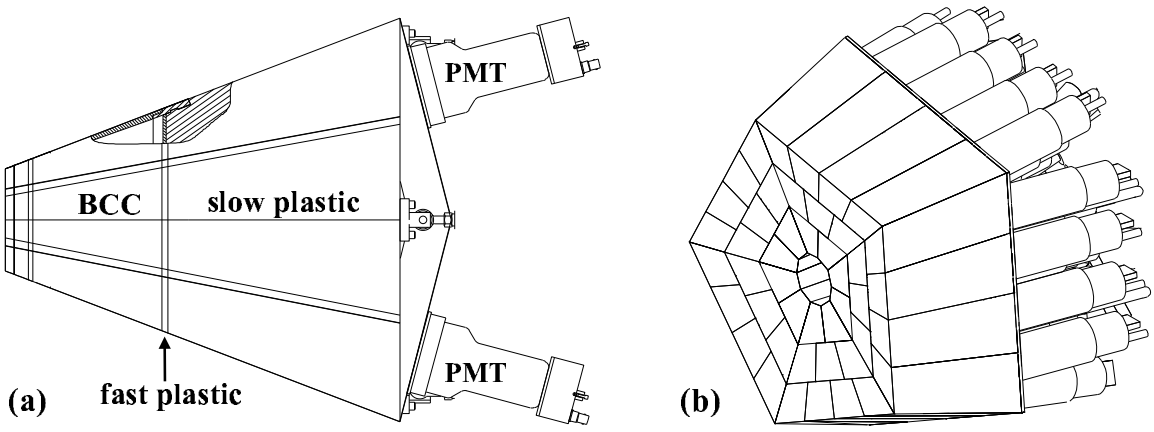

Figure 2.3: Schematic diagram showing the components of a 4π Array module. (b) Geometry of the High Rate Array.

pulse. The contributions of the phoswich's individual layers to the current pulse can be separated because the fast and slow plastic have different response times (hence the names "fast" and "slow"). The separation is done in the electronics, discussed in Sec. 2.3. The thin layer of fast scintillator acts as a ΔE detector, while the thick, slow scintillator records the residual energy E when a charged particle is fully stopped.

Bragg Curve Counters

Mounted in front of each of the 30 Main Ball phoswich modules is a gas ionization chamber known as a Bragg Curve Counter (BCC) [31]. The BCCs primarily are used to detect α particles (Z=2) as well as intermediate mass fragments (*i.e.,* particles with charge $3 \leq Z \lesssim 20$). These heavier fragments often do not "punch through" the thin fast plastic and could not be identified without the BCC. The five most forward hexagonal modules have BCCs with anodes of the same segmentation as the phoswiches; otherwise, a single BCC chamber is used for an entire module's phoswiches. Thus, there are 55 separate BCC detectors in the Main Ball.

Figure 2.3(a) shows the cross section of one of the 30 ball modules. When particles such as IMFs stop in the thin fast plastic, the BCC serves as the ΔE detector and

the fast plastic serves as the E detector. The threefold combination of detectors is *logarithmic*, since the purpose of each layer changes as a function of an incident particle's penetration depth. Detectors of this nature are often called *telescopes*.

High Rate Array

Mounted to the exit plate of the 4π Array vacuum vessel is a 45-segment fast/slow plastic scintillator array known as the High Rate Array (HRA) [33]. The HRA, built by Robert Pak, provides a sturdy, close-packed subsystem of sufficiently high granularity to handle the large fraction of particles emitted at small polar angles (due to the center of mass boost). The 45 phoswich detectors span the polar angles $3^\circ \lesssim \theta_{lab} \lesssim 18^\circ$ and detect particles from $Z = 1$ to $Z = 14$. Figure 2.3(b) shows the basic geometry of the HRA; each of its five faces is tilted slightly so that incident particles impinge perpendicular to the detector's face.

The HRA functions the same way as the fast/slow phoswiches in the Main Ball. An incident particle produces light in both layers of the plastic, and the light is collected by a single PMT. The separation of the PMT signal into ΔE and E components is possible because of the different response times of the two layers of plastic. In the following section, the procedure for converting the detector signals from the 4π Array to the raw data, which is stored on magnetic tape, is detailed.

2.3 Electronics and Raw Data

Figure 2.4 illustrates the general route taken by a candidate phoswich or BCC signal through the electronics of the 4π Array, with a possible final destination on a raw data tape. The term "candidate" applies to the signals because several conditions need to be satisfied for a signal to be recorded. This section outlines the basics of the 4π Array's electronics setup. The High Rate Array's electronics are nearly identical to

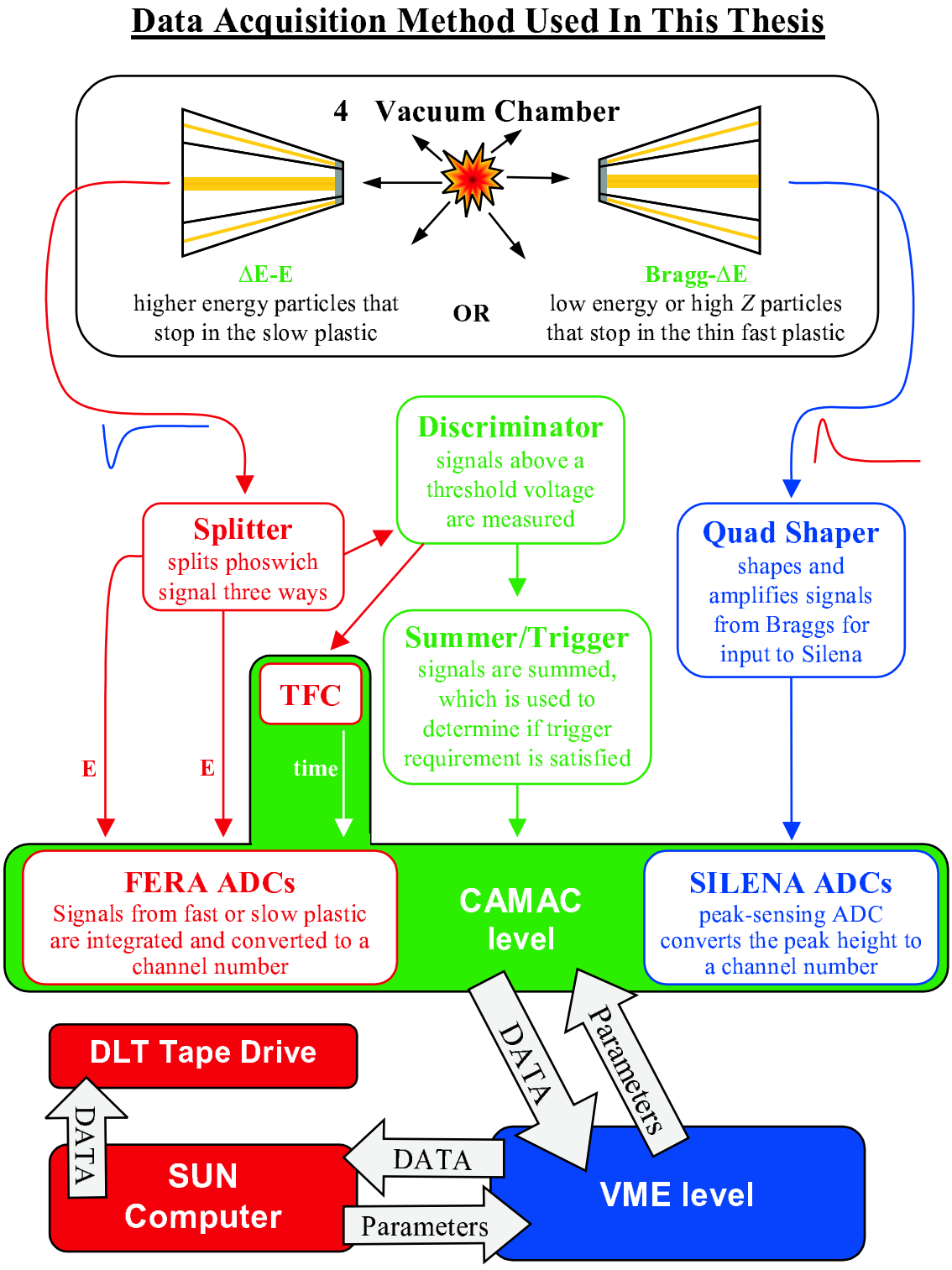

Figure 2.4: Simple schematic of the method for converting the detector signals into a form which can be stored on magnetic tape.

the phoswiches of the Main Ball and do not need separate discussion. The discussion is more qualitative than technical in order to complement the rigorous explanations of previous theses with nearly identical experimental setups [34, 35].

Phoswich signals

The PMTs of the 215 Main Ball and HRA phoswich detectors, located in the vacuum vessel, are supplied their voltage via a single cable which also transmits the detector signal. These high-voltage cables are connected to splitter box modules where the high voltage is separated from the phoswich signal and the signal is split into three signals: ΔE, E, and *time*. The time signal initially goes to a 16-channel discriminator which checks to see if the signal's (negative) amplitude is larger than the pedestal level for that channel. If it is, then a voltage signal proportional to the number of hits in the discriminator is sent by the discriminator to a summer which adds the voltages of the Main Ball (and/or HRA) channels. If the summed voltage signal for all channels exceeds the requirements of the trigger (*i.e.,* if enough detectors fire discriminators), then a gate is generated which allows the signals from all detectors, including the BCCs, to be recorded to tape.

The current pulses representing the ΔE signal and E signal are identical when leaving the splitter box. However, the signals are gated differently by their respective FERAs, which are analog-to-digital converters (ADCs) with 2048-channel resolution. The general shape of the current pulse and the ΔE and E gates to separate the fast and slow components of this signal are schematically shown in Figure 2.5. Data from the phoswich FERAs are zero-suppressed, *i.e.,* only channels with nonzero values are recorded to tape. For all channels, the pedestal level, which represents the minimum threshold amplitude a particular channel's signal needs in order to be nonzero, is determined by operating the electronics with the detectors turned off to determine

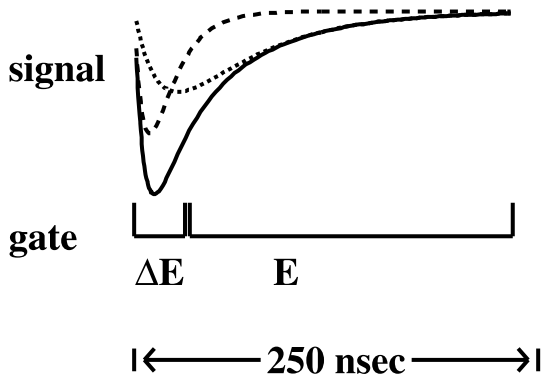

Figure 2.5: Diagram of the phoswich signal and gates. The width of the two FERA gates selects the appropriate section of the signal.

the noise level of that channel. The pedestals are passed as parameters from the UNIX computer to the FERAs where they are stored in memory. The use of zero suppression and pedestals reduces the amount of dead time as well as the amount of tape used. Including the ΔE and E for both the Main Ball and HRA, there are 645 channels of electronics in the FERAs.

BCC signals

Because the response time for a Bragg Curve Counter signal is on the order of microseconds (as opposed to 100s of nanoseconds for the phoswich signals) and the arrival time varies by microseconds, BCCs are not used in the trigger. The BCCs are supplied their voltage via a separate cable. A BCC signal first passes through a quad shaper, which amplifies the signal and produces a very clean voltage signal. The amplified signal then goes to a Silena, a peak-sensing analog-to-digital converter with 4096-channel resolution. Like FERAs, Silenas are zero-suppressed so that only non-zero channels are written to magnetic tape. In total, there are 55 channels of Silenas used for BCC electronics.

2.3.1 Writing Raw Data

The 4π Array trigger can be configured to include the phoswiches of the Main Ball and the HRA, and the trigger level can be adjusted to select certain types of events. A trigger level of 5 preferentially would select more central events, since peripheral events produce fewer particles (see Sec. 3.1). If a trigger is satisfied (*i.e.,* enough phoswich pulses produce voltage signals in the discriminators) then electronic gates are generated and sent to the ADCs, and the digitized signal information is recorded and sent via a VME crate to a UNIX computer.

In the 4π Array's data acquisition configuration, raw data is written to magnetic tape by the UNIX computer which also serves as the gateway for ethernet access from outside the experimental vault. On-line monitoring of detector counts and energy spectra are done via the ethernet connection. The computer also monitors the electronics and can set threshold levels to the individual FERAs and discriminators. Raw data are written on an event-by-event basis to tape. The on-line monitoring programs and analysis software perform the task of selecting and matching signals from an event that correspond to the same particle.

2.4 Reducing Raw Data to Meaningful Quantities

The basic task of the electronics is to convert detector signals into numbers that can be stored on tape in a structured manner. Analogously, the task of translating these numbers into physics variables (such as energy and charge) is performed by a series of software routines designed to identify and characterize charged particles from the raw data numbers which includes signals from cosmic rays as well as neutral particles (such as neutrons and high-energy gamma rays). The result of these software routines is a conversion and reduction of raw data to "physics" files, which are much smaller

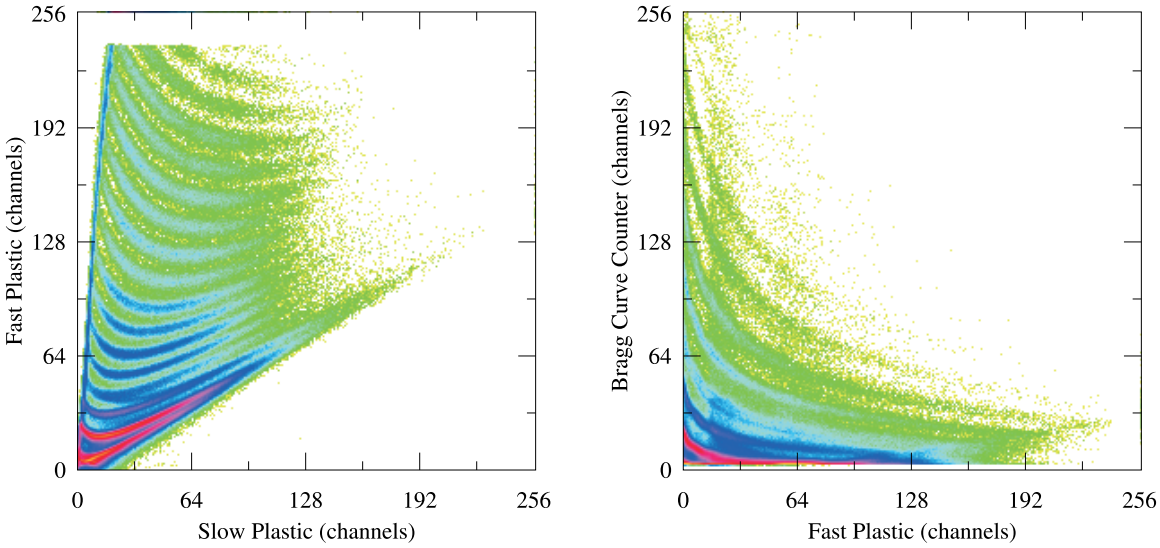

Figure 2.6: (a) Sample ΔE-E spectra from HRA phoswich detector. (b) Sample ΔE-E spectra from BCC-fast plastic pair.

and permit quicker analysis of the data.

2.4.1 Particle Identification

When the integrated signals from the thin fast plastic are plotted versus the corresponding signals from the thick slow plastic, particles with different charges and masses fall into different bands in the resulting ΔE-E spectrum. The same is also true for particles that stop in the fast plastic of the Main Ball, although in that case the BCC signal serves as the ΔE. Figure 2.6 shows examples of raw two-dimensional spectra produced by (a) a HRA phoswich and (b) a particle stopping in the fast plastic.

Some of the qualities of fast/slow spectra differ from those of BCC/fast spectra. Fast/slow spectra (Figure 2.6(a)) are bound by thick diagonal lines, which result from the fact that the same detector signal is sampled for both the ΔE and E. The nearly vertical line, called the *punch-in* line, contains signals from particles which stopped in the fast plastic; the diagonal line that forms the bottom border of the spectra arises

from cosmic rays or neutrons that scintillate in the thick slow plastic only. In contrast, the BCC/fast spectra (Figure 2.6(b)) do not have these lines, since there is no overlap between the two different signals. A decision is made for particles with both phoswich and BCC signals as to which spectra type should be used to identify the particle. If the particle lies in the punch-in line of the fast/slow spectra (as determined by a 2-D gateline), then it is identified using the BCC/fast spectra.

Figure 2.7 shows the process for reducing raw data used in this thesis. The first step, corresponding to the blue boxes, is to sort the raw data by detector into fast/slow spectra and BCC/fast spectra. These spectra then are gain-matched to existing 2-D templates by adjusting the offset from the origin and by stretching/shrinking each spectra to account for voltage and gate differences between the detectors and the reference template. The templates for each spectra type (HRA fast/slow, Main Ball fast/slow, Main Ball BCC/fast) were created when the particular subsystem was added to the 4π Array, and their purpose is to map experimental raw data numbers into particle type and incident kinetic energy. The two gain-matching programs (MTK and BRAGGMATCH[2]) generate parameter files, known as *lines files*, that contain the offsets and multiplicative factors for each axis for all 2-D spectra.

2.4.2 Physics Quantities

Once the lines files for all of the detectors are generated, the raw data are converted to physics data with PHYTAPE, a VMS-based program that uses an assortment of tables and parameter files to assign physics quantities to each real particle. This assortment includes:

- lines files generated by the gain-matching programs;

[2]The BCC/fast spectra were matched using a MAC-based application written by Gary Westfall for the first time. This replaced a VMS-based program whose graphics package was phased out by DEC.

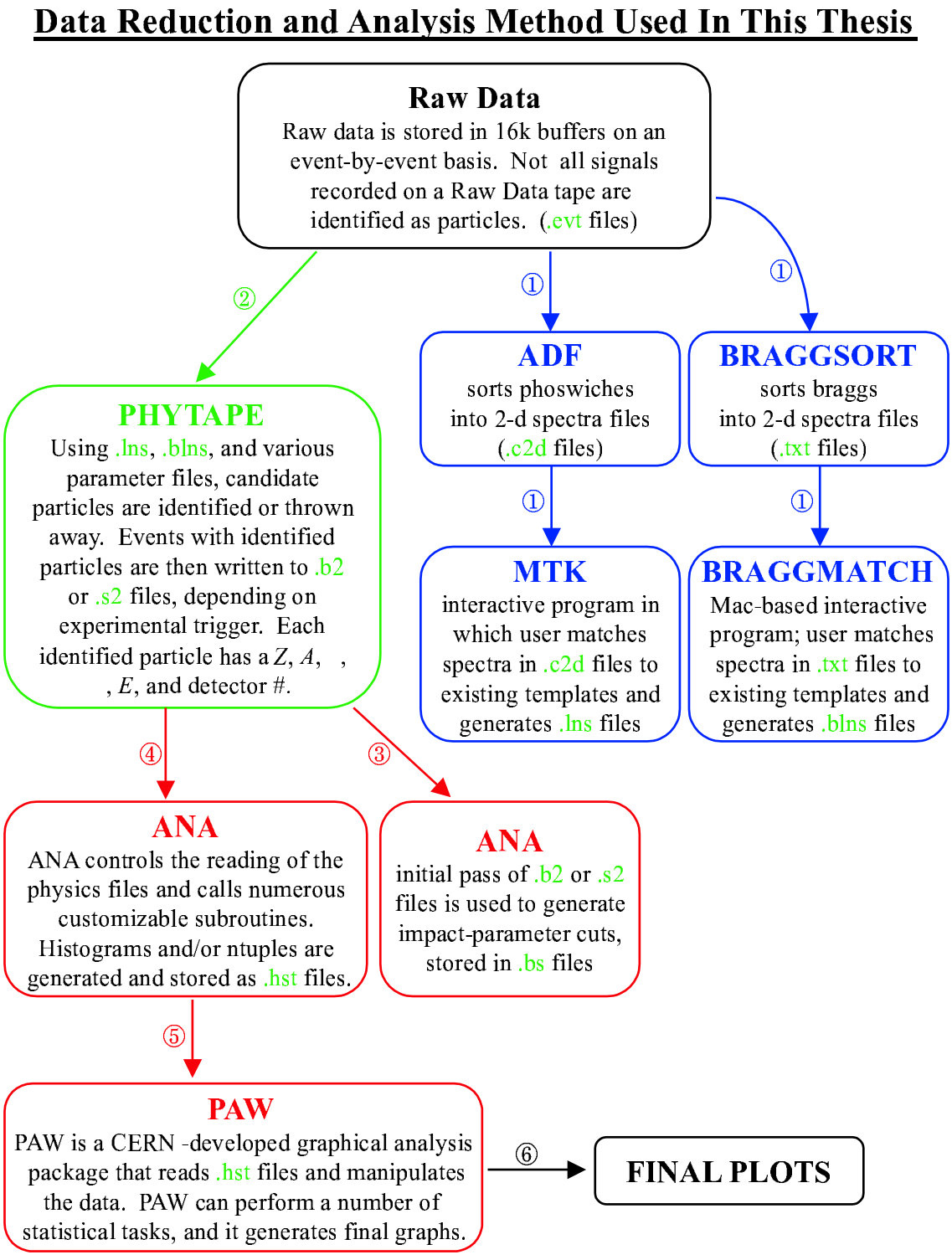

Figure 2.7: Simplified diagram that shows the entire process from raw data to final plots used in this thesis.

- detector parameter files which map detector number to their lab polar angles (θ, ϕ);
- look-up files which contain 2-D arrays for mapping the matching templates to particle type and energy.

For each event with at least one particle, identified particles are written to a physics file by their parameters Z, A, θ, ϕ, E, and detector number.

Some particles are flagged because of their location in the ΔE-E spectra. For example, candidate particles that fall in the punch-in line of the fast/slow ΔE-E spectra but do not have BCC signals are assigned a mass of $A = 0$ so that they can be included/excluded in the analysis. Also, particles that overflow a particular axis (which happens when the maximum channel number of an analog-to-digital converter is exceeded by a detector signal) are flagged with negative mass so that their inclusion in the analysis can be decided later.

2.5 Summary

Once the experiment has been performed and the raw data have been converted to useful physics variables, the analysis can begin. Figure 2.7 indicates the basics of the analysis in red boxes. One primary aspect of the analysis in this thesis is the use of millions of collision events to increase statistics and to decrease fluctuations in analysis variables. The next chapter details some of the analysis techniques used in this thesis to describe and classify the collisions.

Chapter 3

Characterizing the Collisions

Before anything can be said about the physics of nuclear reactions, it is first necessary to determine the parameters of each collision. For example, to first order, the number of particles produced in a collision depends on four parameters: three chosen by the experimentalist (beam energy, projectile particle type, and target particle type) and one selected by the collision itself (the impact parameter, see Sec. 3.1). If a theorist wishes to predict the number of particles that will be produced in a collision, he or she needs to specify these four parameters.

Determining the nature of each collision requires manipulating the experiment's measured quantities. In the case of the 4π Array, the measured quantities for each particle are charge, mass, final position, and kinetic energy. Using these variables, we can calculate a particle's momentum, rapidity (an invariant measure of longitudinal velocity), transverse kinetic energy, and other useful quantities. We can also sum certain quantities over all measured particles in an event to produce even more useful quantities, such as total transverse kinetic energy, excitation energy, etc.

For the present analysis, several tasks need to be completed before the results can be presented. Some of these tasks characterize the collisions, others were performed to understand or reconcile confusing results, and still others were merely diagnostic. In

this chapter, the impact parameter and reaction plane determination are presented. Also, several corrections to the data are made in an effort to remove some of the experimental bias from the 4π Array.

3.1 Impact Parameter

As expected from the Nuclear Fireball Model [23] (see Fig. 1.4), what transpires during a nuclear collision depends strongly on the **impact parameter** of the collision. Two nuclei that merely graze each other will produce a tiny participant zone of compressed matter, while a head-on collision of zero impact parameter will lead to higher compression and larger pressure gradients because nearly all the initial kinetic energy is deposited into the participant source. As a result, both collective flow observables being studied in this thesis have been shown to depend on impact parameter. In the case of the disappearance of directed flow, Pak *et al.* showed that the balance energy increases linearly as a function of the impact parameter for a light system such as Ar+Sc [58]. For the transition to out-of-plane elliptic flow, data from Popescu *et al.* showed the energy of transition to increase with impact parameter for ^{64}Zn+^{58}Ni [92].

Figure 3.1 illustrates the definition of impact parameter $\vec{b}$ as the vector pointing from the center of the target to the center of the projectile's path (beam points along the z-axis). A maximum impact parameter of $b_{\rm max} = R_{\rm proj} + R_{\rm targ}$ is defined and is especially useful for studying the system mass dependence of a quantity, since the basic geometry of the collision can be preserved. The 4π Array is well-suited to act as an impact parameter filter due to its large acceptance.

Impact parameter is not a directly accessible experimental quantity, but there are several *centrality* variables which have been shown to be strongly correlated with the impact parameter. These include total charged-particle multiplicity [36], midrapidity

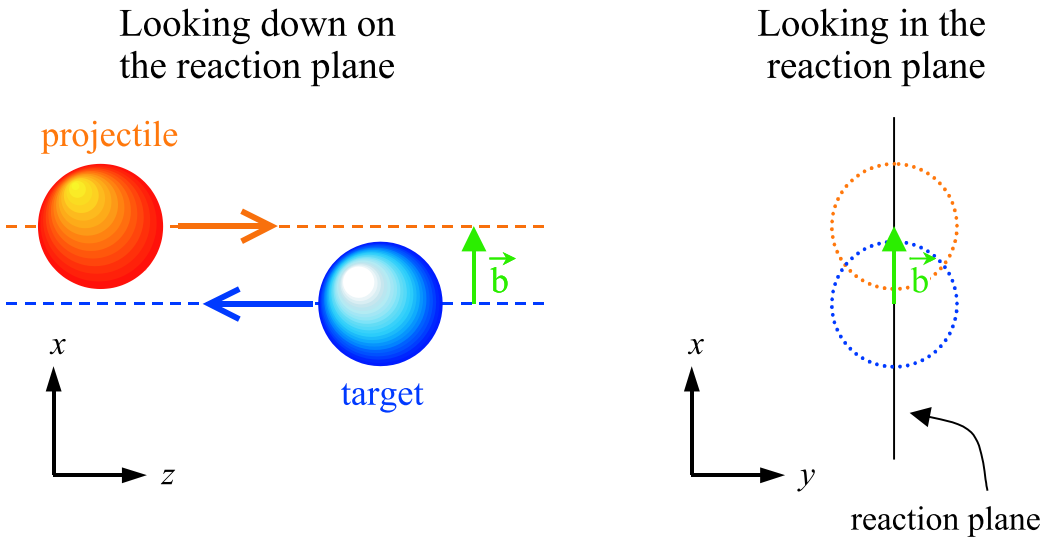

Figure 3.1: Geometrical description of the impact parameter and the reaction plane. The impact parameter vector $\vec{b}$ lies in the reaction plane and points to the projectile side.

charge [37], and the total transverse kinetic energy E_t [38]. In this thesis, E_t is the chosen centrality variable because impact parameter binning can be more precisely controlled [39] and because the acceptance of the 4π Array over the range of Au+Au energies is weak at backward midrapidity; see Figure 4.12.

The total transverse kinetic energy of an event with N identified particles is defined as

$$E_t = \sum_{i=1}^{N} E_i \sin^2 \theta_i \ , \tag{3.1}$$

where E_i is the kinetic energy and θ_i is the polar angle of the ith particle in the lab frame. To obtain a quantitative estimate of the impact parameter from E_t (or any other centrality variable), a geometrical prescription owed to Cavata *et al.* [36] assumes that E_t is monotonically related to the impact parameter b, *i.e.*, as E_t increases from zero to its maximum value, b continually increases or decreases, but not both. The following relation expresses this:

$$\frac{2\pi b db}{\pi b_{\max}^2} = -f(E_t) dE_t \ . \tag{3.2}$$

In this expression $f(E_t)dE_t$ is the probability of detecting a collision with a value between E_t and $E_t + dE_t$. The function $f(E_t)$ is normalized to unity. A consideration of $b = 0$ and $b_{\rm max}$ leads to the assumption that $b \to b_{\rm max}$ corresponds to $E_t \to 0$, which causes the minus sign in Eq. 3.2.

The correct divisions in the E_t spectra for placing events into impact parameter bins can be obtained by integrating Eq. 3.2 from b to $b_{\rm max}$:

$$\int_b^{b_{\rm max}} \frac{2bdb}{b_{\rm max}^2} = -\int_{E_t(b)}^{E_t(b_{\rm max})} f(E_t')dE_t' \ . \tag{3.3}$$

The integration limit $E_t(b_{\rm max})$ can be replaced with 0 as stated above. After integrating the left-hand side, the *reduced* impact parameter $b/b_{\rm max}$ can be expressed as

$$b/b_{max} = \sqrt{1 + \int_{E_t(b)}^{0} f(E_t')dE_t'} \ . \tag{3.4}$$

This expression directly relates the E_t spectra (normalized to unity) to $b/b_{\rm max}$ through the integral.[1] For example, a reduced impact parameter of $b/b_{\rm max} = 0.5$ corresponds to the $(0.5)^2 \times 100 = 25\%$ events with the largest E_t.

To separate the data into impact parameter bins, equal partitions of the E_t spectra with respect to the number of events are constructed and the limits of the bins are determined from Eq. 3.4. Figure 3.2 shows sample reduced E_t ($E_t/E_{\rm proj}$) spectra for Au+Au at three different energies. The hatched area represents the 20% of all events with the largest E_t. Using Eq. 3.4, this corresponds to $b/b_{\rm max} \leq 0.44$, which is roughly 6 fm using the formula $R = 1.2A^{1/3}$ fm for the radius of each Au nucleus. In Chapters 4 and 5 different impact parameter binning is used, depending on the observable and whether it is being plotted with data from previous studies.

[1]The value of the integral in Eq. 3.4 is always between 0 and -1 because the integration is carried out from left to right in the E_t spectra. Therefore, $b/b_{\rm max}$ is between 0 and 1, as required.

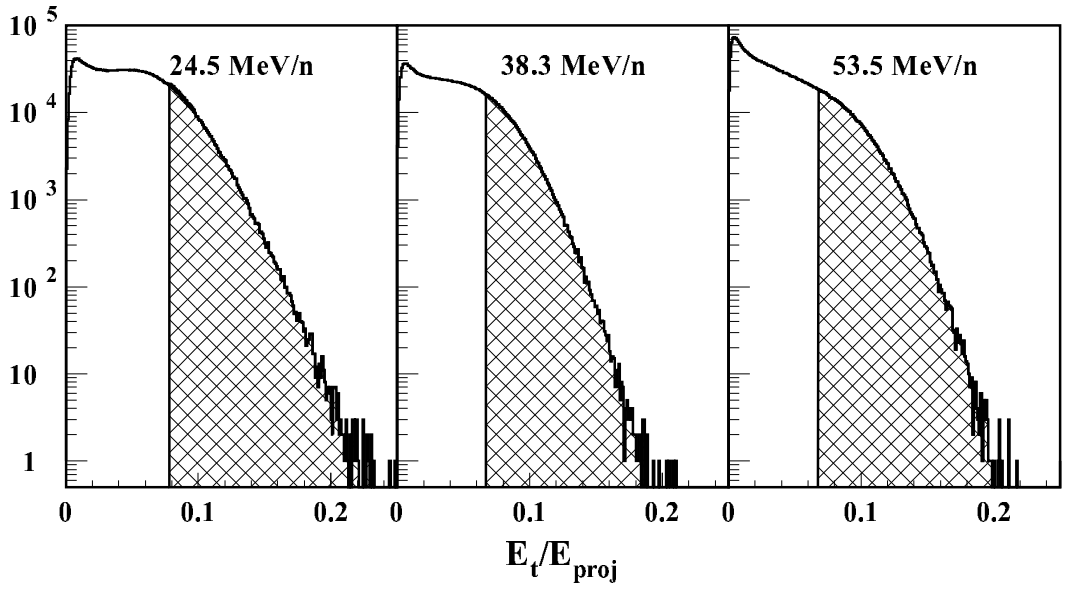

Figure 3.2: Reduced total transverse kinetic energy ($E_t/E_{\rm proj}$) for three different beam energies of Au+Au. The hatched area corresponds to the 20% most central events, as explained in the text.

3.2 Reaction Plane Determination

The observation and quantization of directed and elliptic flow require the accurate determination of a **reaction plane**, since both observables rely on the azimuthal angle between the flow particles and the reaction plane. In the thesis, the convention

$$\Phi = \phi_i - \phi_{\rm RP}.$$

is chosen to mask the $\phi_{\rm RP}$ angle, since it is the orientation of particles with respect to the reaction plane that is of importance. Historically, two standard techniques of reaction plane determination have been used most commonly: the sphericity tensor method [40] and the transverse momentum method [52]. The *sphericity tensor method* uses the existence of flow to calculate a kinetic energy tensor which represents an ellipsoid, and the reaction plane is formed by the plane which contains the beam and the principal axis of the ellipsoid. Danielewicz and Odyniec [52] showed that the sphericity tensor method is poor when the flow signal is weak, because any spherical momentum distribution of a finite number of particles will yield a reaction plane and

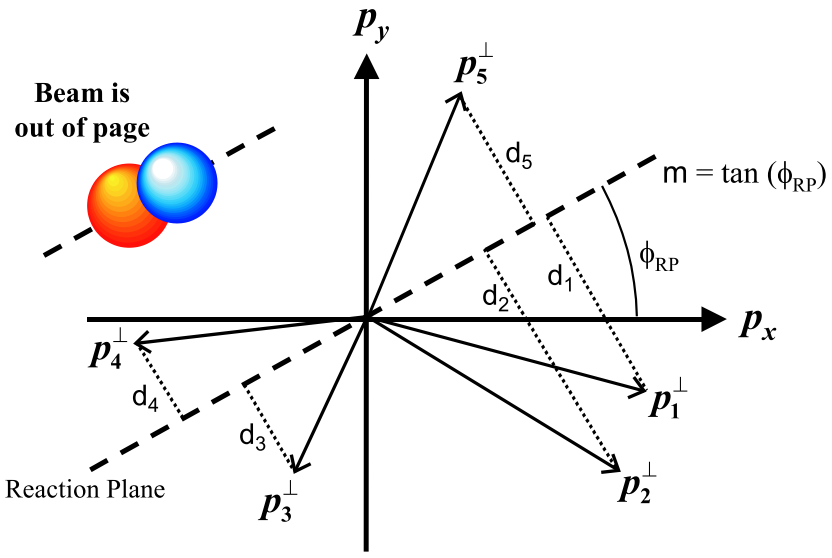

Figure 3.3: The azimuthal correlation method of reaction plane determination. The line that minimizes the sum of the distances d_i squared corresponds to the reaction plane.

non-zero flow, even if generated randomly. In contrast, the *transverse momentum method* uses only the transverse components of the particles' momenta to determine the reaction plane:

$$\mathbf{P} = \sum_{i=1}^{N} \omega_i \, \mathbf{p}_i^\perp \tag{3.5}$$

where the weight ω_i is chosen to be positive (negative) for particles emitted in the forward (backward) center-of-mass hemisphere. The reaction plane is defined by the beam axis and $\mathbf{P}$, which points toward the positive side of the plane.

Both of these techniques were shown to be inferior to the *azimuthal correlation method*, introduced by Wilson *et al.* [41], for cases when flow is weak. The method is based on the observation that particle emission is strongly enhanced in the reaction plane. Thus, this technique involves finding the plane that aligns best with the particles themselves. Figure 3.3 illustrates the azimuthal correlation method for a small event of five particles. The sum of the deviations d_i of the particles' transverse

momenta in the event from a line which passes through the origin is given by:

$$D^2 = \sum_{i=1}^{N} [\mathsf{d}_i^2] = \sum_{i=1}^{N} \left[(p_i^x)^2 + (p_i^y)^2 - \frac{(p_i^x + \mathsf{m} p_i^y)^2}{1 + \mathsf{m}^2} \right]. \tag{3.6}$$

where m is the slope of the line in Figure 3.3. The value of m which minimizes D^2 is determined by setting the derivative of D^2 with respect to m equal to zero and finding the two roots, which are

$$\mathsf{m} = \frac{\sum_{i=1}^{N} [(p_i^y)^2 - (p_i^x)^2] \pm \sqrt{(\sum_{i=1}^{N} [(p_i^x)^2 - (p_i^y)^2])^2 + 4(\sum_{i=1}^{N} [p_i^x p_i^y])^2}}{2 \sum_{i=1}^{N} [p_i^x p_i^y]}. \tag{3.7}$$

Substituting the two m roots back into Eq. 3.6 determines which root minimizes D^2 and maximizes the in-plane enhancement. ϕ_{RP} is found by taking the arc tangent of m and picking the direction for the positive side of the reaction plane using Eq. 3.5.

A necessary step taken to avoid autocorrelation between ϕ_{RP} and ϕ_i when measuring the flow of the ith particle is to remove that "particle of interest" (POI) from the determination of ϕ_{RP}. This must be done for each flow particle in an event, resulting in N different reaction planes for an event of N particles. To examine the effect of excluding POIs from the ϕ_{RP} determination, Figure 3.4 shows the spread of an event's N reaction planes with respect to the average ϕ_{RP} for all events. The narrow distribution peaked at 0° demonstrates the validity of using a separate reaction plane for each POI, which also greatly enhances the statistics of the method.

Another way to see the effect of excluding the POI is to view the relationship between the reaction planes determined with and without the POI. Figure 3.5 shows this relationship by means of a three-dimensional surface plot. A very strong correlation exists, since a tall row of peaks exists at $\phi_{\mathrm{RP,POI\ INC.}} = \phi_{\mathrm{RP,POI\ EXC.}}$. The small rows of bumps to the left and right of the strong correlation correspond to the slight probability that a reaction plane's direction flips to the other side of the beam, (*i.e.*, rotates by 180°). The peaks at (90°, 270°) and (270°, 90°) illustrate an interesting and small side effect of the azimuthal correlation technique. Reaction planes aligned

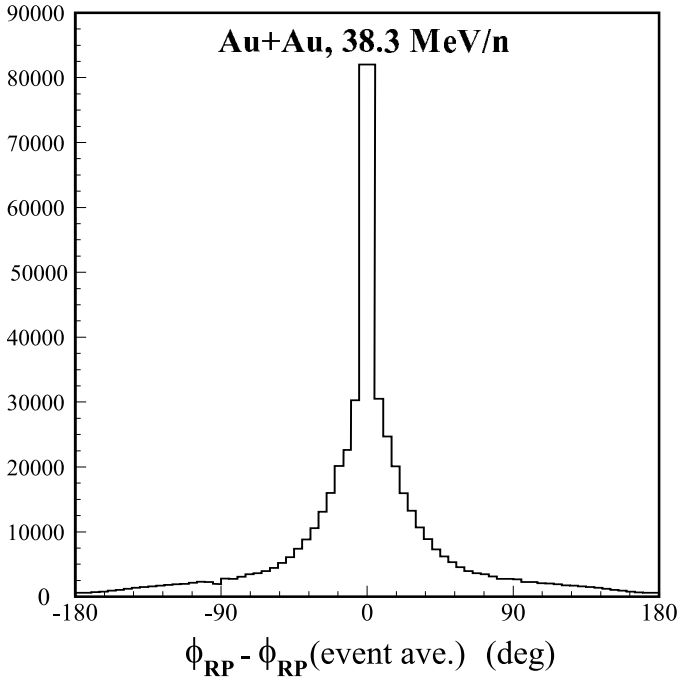

Figure 3.4: Distribution of the azimuthal angles between the individual reaction planes for an event and the event average. Removing the flow "particle of interest" leads to N reaction planes for each event.

near the y-axis are slightly more likely to appear flipped to the other side when the POI is excluded due to the more likely chance that a small rotation of the ϕ_{RP} angle will move the direction into a neighboring quadrant.

It should be emphasized that the above method can only estimate the true reaction plane. The true reaction plane is concealed by an imperfect detector system, a finite number of particles, and thermal fluctuations. Because of the difference between the true and estimated reaction planes, the observed flow projected into the estimated reaction plane will always be smaller than the actual flow. A measure of the accuracy of the reaction plane determination is the *reaction plane resolution*, discussed in Section 3.3.3.

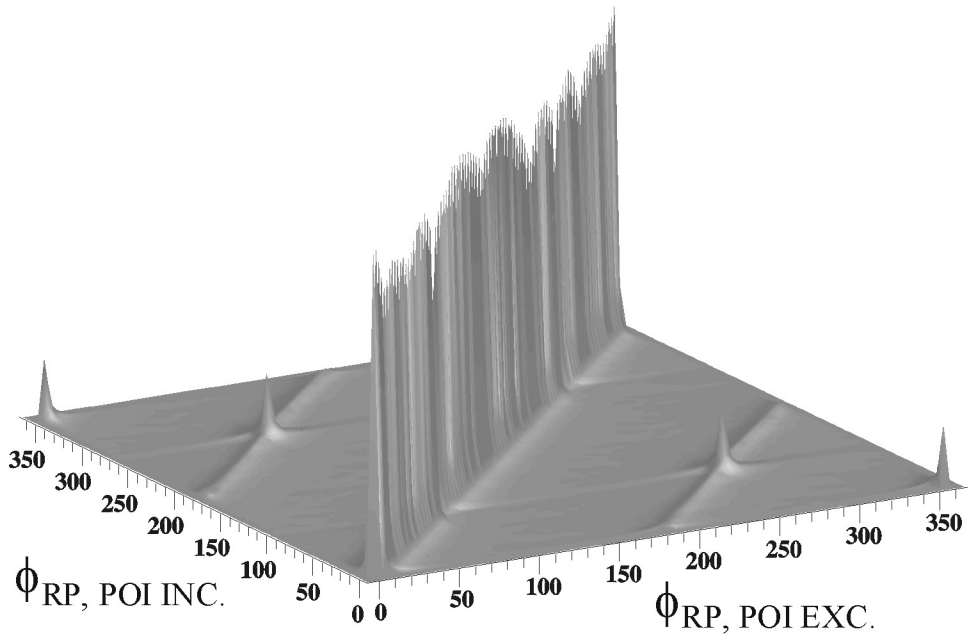

Figure 3.5: Relationship between the reaction planes determined including and excluding the particle of interest. The tall row at $\phi_{\mathrm{RP,POI\ INC.}} = \phi_{\mathrm{RP,POI\ EXC.}}$ shows the minimal effect that excluding the POI has on the reaction plane determination.

3.3 Correcting for Experimental Biases

One of the underlying objectives of nearly all science is to find experimental observables which can be compared unambiguously to theory. Unfortunately, in nuclear physics the comparison is obscured by features of the detector system. The primary quality of nuclear experiments that acts to bias the data is the finite position and momentum resolution of all detectors. This is caused by either the physical dimensions and properties of the detector elements (such as the 4π Array) or the error associated with reconstructing a particle's path through a detector (track resolution). Experimenters go to great lengths and expense to improve position and momentum resolution by building larger detector arrays with more detector elements. For example, the ALICE detector currently being built at CERN will have more than a million separate detector elements [42] to improve the detection resolution for the anticipated 50,000 particles per collision. In this section, corrections made to the data presented

in this thesis are discussed.

3.3.1 Angle Smearing

In total, the 4π Array contains 215 geometrical detector elements: 45 phoswiches in the High Rate Array and 170 BCC-phoswich telescopes in the Main Ball. The 215 detectors almost completely surround the target at the center of the array so that each detector covers an appreciable amount of solid angle. The position of an incident particle within the detector cannot be determined for detectors of these types. Therefore, previous studies of collective flow with the 4π Array assigned the geometrical center of the detector as the particle's (θ, ϕ). This leads to discrete bands in both anguular distributions. In addition, the 4π Array has five-fold symmetry in the azimuth due to its truncated icosahedronal shape, leading to slight anisotropies in the ϕ distributions.

Assigning a particle's position to be the geometrical center of the detector affects the isotropic symmetry of the reaction plane distribution. It also is slightly erroneous because the "most likely" location for a particle to strike depends slightly on the center of mass boosts for different beam energies.

In order to reduce the effects of detector granularity in the 4π Array, the assigned θ and ϕ angles for each particle are smeared over the range of angles covered by the detector. The angular probability distributions for each detector are generated by making use of the 4π software filter which describes the geometry of the 4π Array. To generate the (θ, ϕ) histograms that describe each detector's acceptance, isotropic distributions of protons were produced in the center of mass by a simple event generator and boosted to several different beam energies. The distribution was passed through the 4π software filter, and reference histograms were created. CERN's Physics Analysis Workstation (PAW) software was used to assign a variable based on

the distribution of a 1-D histogram.

Then, each particle's (θ, ϕ) in the experimental data was smeared by making use of the histogram look-up table for the particular detector. Figure 3.6 shows the effect of angle smearing on the θ and ϕ distributions for Au+Au at 40 MeV/nucleon. The discrete blue bands represent the centers of the detectors, and since the 4π Array has five-fold symmetry there are five times fewer discrete bands as there are detectors. The green spectra represent the smeared angular distributions. The ϕ distribution is nearly flat as expected, with the exception of five periodic dips. These irregularities correspond to the corners of the pentagon created by the five most forward modules, evident from inspection of the mean ϕ angles in Table A.6 in Appendix A. The θ distribution is smoother and is peaked at forward angles due to the velocity of the beam projectile.

In order to check the effect of angle smearing on the analysis, it is practical to investigate the change in the p_x *vs.* $(y/y_{\rm proj})_{\rm cm}$, since p_x is the quantity of interest in the directed flow analysis of Chapter 4. Figure 3.7(a) shows the p_x *vs.* $(y/y_{\rm proj})_{\rm cm}$ distribution when discrete angles are assigned to the particles. When the angles are smeared, as in Figure 3.7(b), the distribution's color contour lines are smoother but the general shape of the plot is unchanged. Therefore, smearing the particles positions according to the 4π software filter is an effective method for dealing with the granularity of the 4π Array.

3.3.2 Repairing the Reaction Plane Distribution

For a perfect detector system, one expects an isotropic reaction plane distribution because beam projectiles are incident upon target projectiles with no preferred side. However, the locations and shapes of detector elements as well as dead channels and imperfect calibration lead to anisotropies in $\phi_{\rm RP}$. Figure 3.8 shows the $\phi_{\rm RP}$

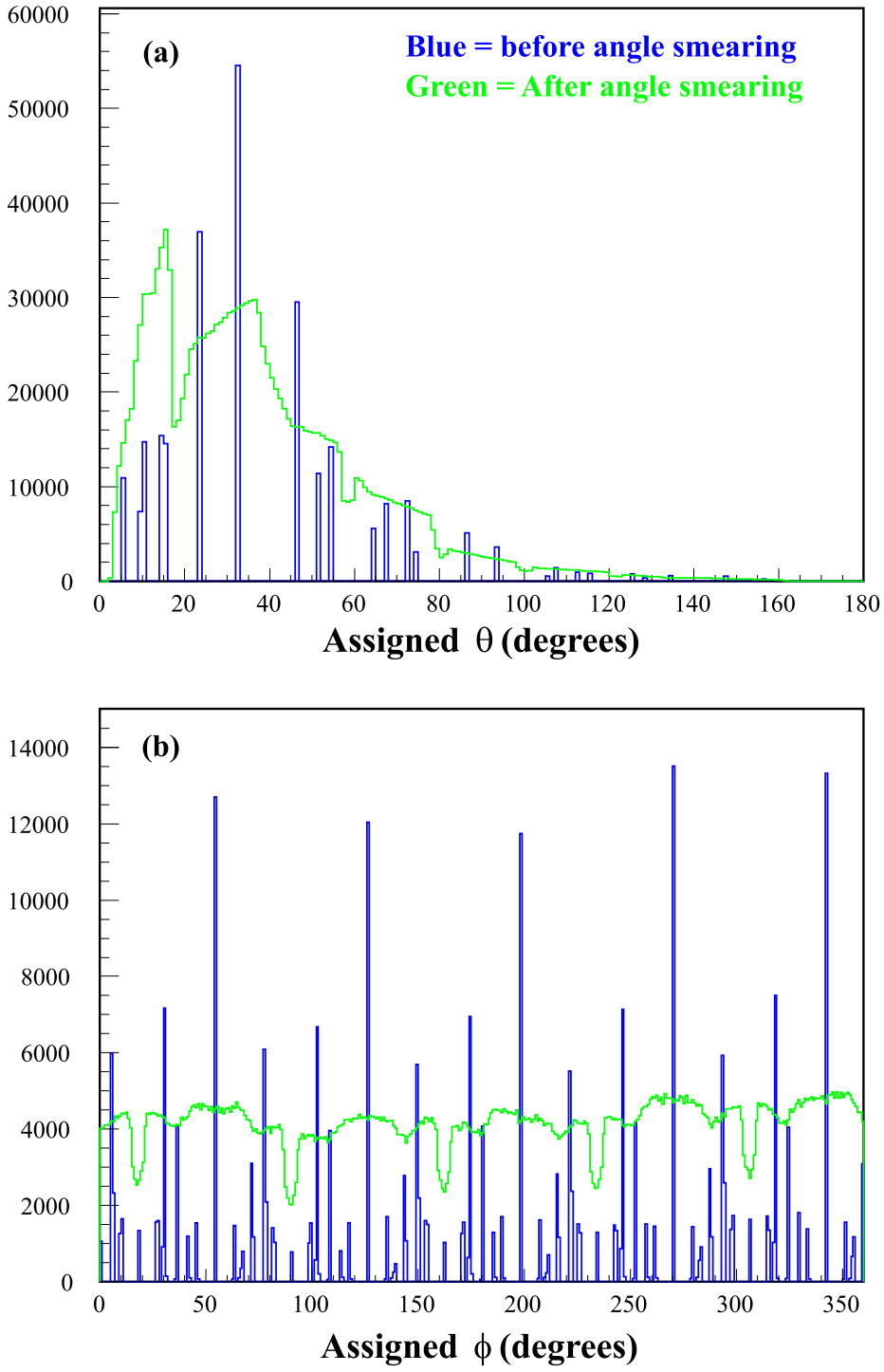

Figure 3.6: Effect of smearing the polar angles of particles over the active area of the detector as opposed to assigning the detector's geometric center (a) θ and (b) ϕ.

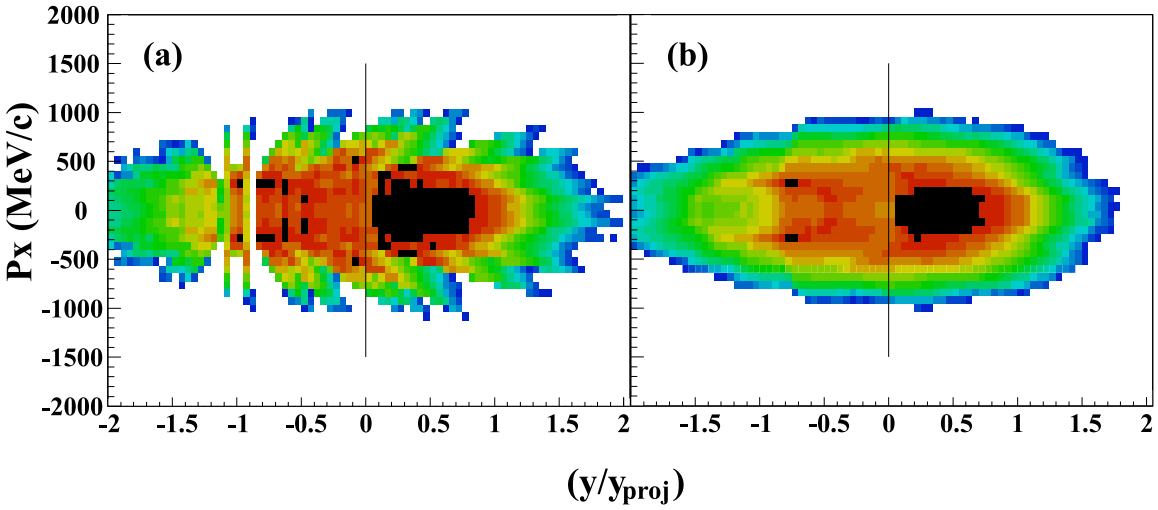

Figure 3.7: p_x *vs.* $(y/y_{\rm proj})_{\rm cm}$ for (a) before angle smearing and (b) after angle smearing for Au+Au at 33.1 MeV/nucleon.

distribution for Au+Au data at 33.1 MeV/nucleon. The arrows pointing downward along the top of the figure indicate the geometric centers of the fifteen most forward detectors in the Main Ball. Since these detectors are subject to higher counts as well as higher-momentum particles, they have a substantial influence on the reaction plane distribution. Also shown in Figure 3.8 is the azimuthal location of module 9, which had a dead Bragg Curve Counter for the duration of the experiment. The effect of module 9 is also seen at 180° from its azimuthal location, since module 9 detects particles from the backward hemisphere which contribute to the reaction plane determination with a 180° phase (see Sec. 3.2).

Biases due to the finite acceptance of the detector can be removed by making the distribution of reaction planes isotropic in the laboratory [43]. There are several different methods to remove the effects of anisotropy which have been used, and each of them has some disadvantages. (see Ref. [43] for a discussion of the different methods.) The method used in this thesis, adopted from the E877 Collaboration at the AGS [44], is to fit the unweighted $\phi_{\rm RP}$ distribution, summed over all events, to a Fourier expansion. An event-by-event shifting of $\phi_{\rm RP}$ needed to make the final

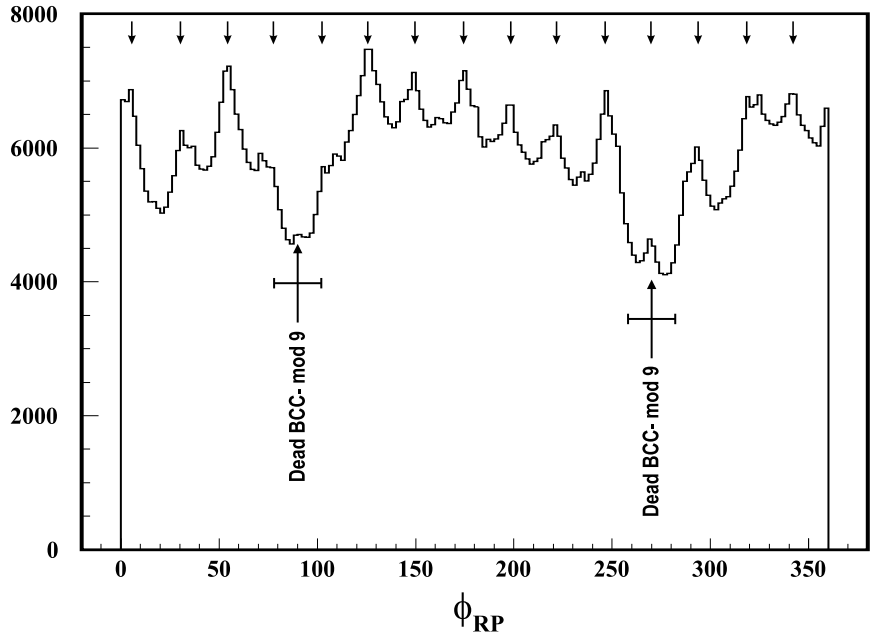

Figure 3.8: Uncorrected reaction plane distribution for Au+Au at 33.1 MeV/nucleon. The arrows along the top of the plot correspond to the 15 most forward detectors in the Main Ball.

distribution isotropic is performed by using the coefficients of the Fourier expansion. A new angle is defined as

$$\phi'_{\rm RP} = \phi_{\rm RP} + \Delta\ \phi_{\rm RP}\ , \tag{3.8}$$

where $\Delta\phi_{\rm RP}$ is written in the form

$$\Delta\phi_{\rm RP} = \sum_n \left[A_n \cos(n\ \phi_{\rm RP}) + B_n \sin(n\ \phi_{\rm RP})\right]\ . \tag{3.9}$$

Requiring the vanishing of the nth Fourier moment of the new distribution, the coefficients A_n and B_n can be evaluated by the original distribution:

$$B_n = \frac{2}{n}\left\langle \cos(n\ \phi_{\rm RP})\right\rangle\ , \tag{3.10}$$

$$A_n = -\frac{2}{n}\left\langle \sin(n\ \phi_{\rm RP})\right\rangle\ , \tag{3.11}$$

where the angular brackets refer to an average over events. These coefficients are written to a look-up file for each set of data, since the reaction plane distribution

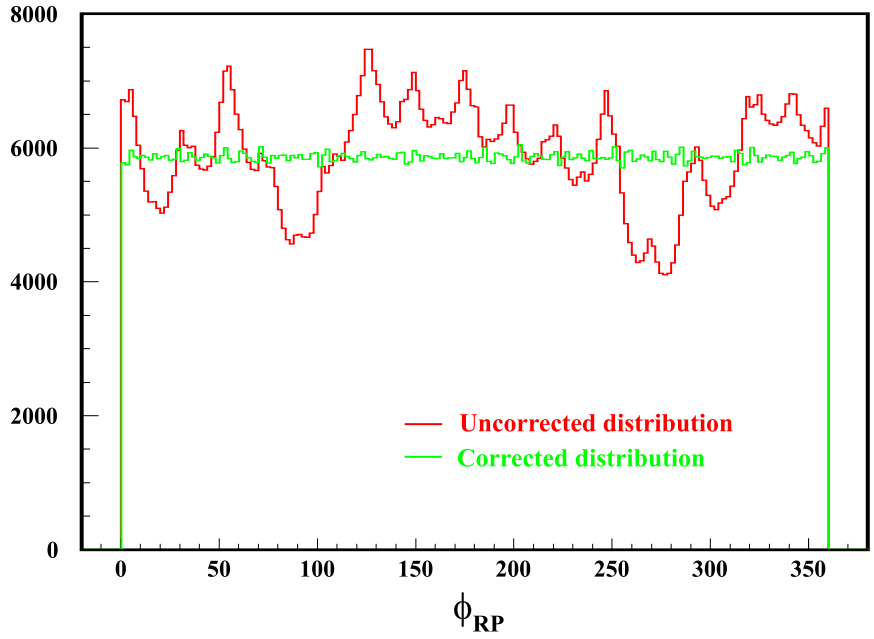

Figure 3.9: Effect of repairing the reaction plane distribution by making use of a Fourier expansion for Au+Au, 35 MeV/nucleon. $n = 30$ terms were used in the expansion.

changes slightly for each beam energy. The final distribution is given by

$$\phi'_{\rm RP} = \phi_{\rm RP} + \sum_n \frac{2}{n} \left[-\langle \sin(n\ \phi_{\rm RP}) \rangle\ \cos(n\ \phi_{\rm RP}) + \langle \cos(n\ \phi_{\rm RP}) \rangle\ \sin(n\ \phi_{\rm RP})\ \right]. \tag{3.12}$$

The number of terms in the Fourier expansion needs to be large enough to account for periodic features of the $\phi_{\rm RP}$ distribution, and the adjusted $\phi'_{\rm RP}$ distribution needs to be checked to make sure it indeed becomes isotropic. In the present analysis, $n = 30$ was used to account for the 15 periodic peaks in the $\phi_{\rm RP}$ distribution and the ten-fold symmetry of the High Rate Array. Figure 3.9 shows the $\phi_{\rm RP}$ distribution before and after the Fourier correction for Au+Au at 35 MeV/nucleon. The distribution is sufficiently flattened for $n = 30$. Redistributing the reaction planes removes possible trigger biases, such as imperfect calibration, dead channels, or any other asymmetry, from the data.

3.3.3 Reaction Plane Resolution

The reaction plane determined in Sec. 3.2 is only an estimate of the *true* reaction plane. The disparity between the measured reaction plane and the true reaction plane is due to imperfect detectors as well as a finite set of particles per collision. Since both observables studied in this thesis, directed flow and elliptic flow, depend on the azimuthal angle between the reaction plane and the particle whose flow is being measured, the data must be corrected for the effects of reaction plane dispersion. The form of the correction is

$$\text{Flow} = \frac{\text{Observed Flow}}{\left\langle \cos(\phi_m - \phi_r) \right\rangle}, \tag{3.13}$$

where ϕ_m and ϕ_r are the experimentally measured and true reaction plane angles,[2] respectively, and the brackets signify the mean over all events. The mean cosine values are less than one and thus this correction always increases the measured flow.

Of course, in its current form the correction term $\left\langle \cos(\phi_m - \phi_r) \right\rangle$ contains the unknown ϕ_r. Therefore, the correction must be obtained by an indirect method. One approach is to recognize that when flow is present, a correlation exists between the azimuthal angles of the particles from a particular collision. In other words, an event's particles themselves can be used to determine the accuracy of the reaction plane determined from all particles. This approach relies on the fact that the reaction plane resolution is directly related to the flow; the stronger the flow, the better the resolution.

When an event of multiplicity N is divided randomly into two equal "subevents" of multiplicity $N/2$, the reaction planes for the subevents are correlated due to the flow present in the collision. Figure 3.10 shows the absolute value of the azimuthal angle between the two reaction planes for Au+Au. The peak at 0° is evidence that

[2]The subscript 'RP' is dropped from the symbols for the reaction plane in this section due to overcrowding. All ϕ angles in this section correspond to reaction plane angles.

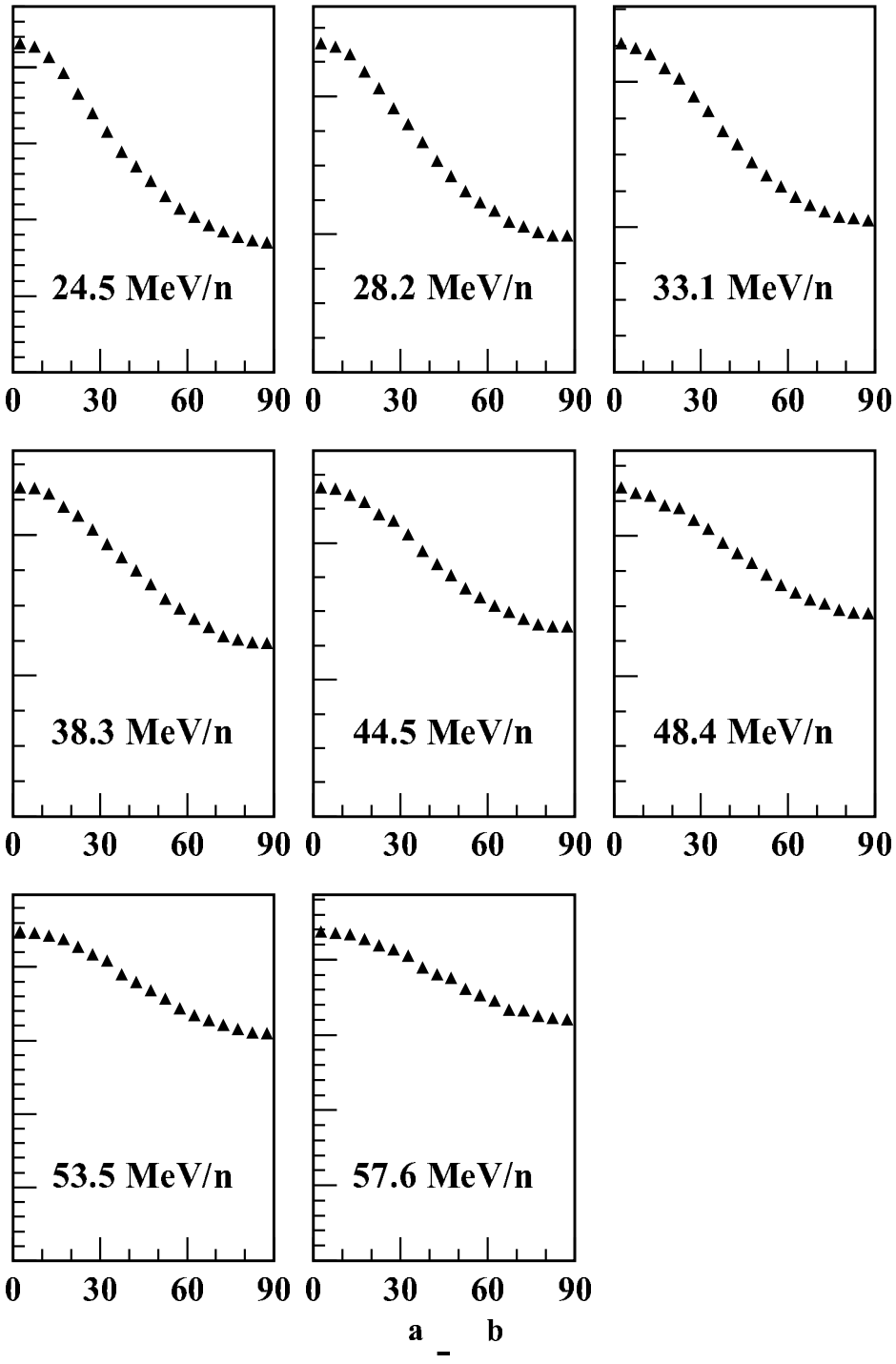

Figure 3.10: Absolute value of the azimuthal angle between the reaction planes for two subevents in Au+Au collisions.

there exists a correlation. The correlation weakens slightly as the beam energy is increased, which is most likely due to the strengthening of the out-of-plane elliptic flow signal for Au+Au, as discussed in Sec. 5.3.2.

The angle between the two constructed reaction planes is related to the true reaction plane by the expression

$$\left\langle \cos(\phi_m^a - \phi_m^b) \right\rangle = \left\langle \cos(\phi_m^a - \phi_r) \right\rangle \times \left\langle \cos(\phi_m^b - \phi_r) \right\rangle , \tag{3.14}$$

where ϕ_m^a and ϕ_m^b are the measured reaction planes for the subevents.[3] Then, recognizing that the correction terms on the right-hand side of Eq. 3.14 should be nearly equal due to the random division of the events,

$$\left\langle \cos(\phi_m^a - \phi_r) \right\rangle \approx \left\langle \cos(\phi_m^b - \phi_r) \right\rangle , \tag{3.15}$$

Eq. 3.14 can be turned around to read

$$\left\langle \cos(\phi_m^a - \phi_r) \right\rangle = \sqrt{\left\langle \cos(\phi_m^a - \phi_m^b) \right\rangle} . \tag{3.16}$$

The resolution of the reaction plane for the full event is related to the resolution for a subevent by a $\sqrt{2}$ because the full event has twice as many particles as the subevents. The final expression for the corrected flow observable is

$$\text{Flow} = \frac{\text{Observed Flow}}{\sqrt{2\left\langle \cos(\phi_m^a - \phi_m^b) \right\rangle}} , \tag{3.17}$$

Table 3.1 lists the $\sqrt{2\langle \cos(\phi_m^a - \phi_m^b) \rangle}$ correction values for all energies of Au+Au. The corrections are used when plotting the present flow measurements with data at higher energies (see Sec. 4.3.3). In agreement with Fig. 3.10, the values decrease as the beam energy increases.

[3] It should be pointed out that the assumption is made that there are no other correlations except the ones due to flow, or that other correlations can be neglected.

Table 3.1: Values for the correction to the reaction plane dispersion.

Beam Energy	Correction Value	Beam Energy	Correction Value
24.5 MeV/nucleon	0.728	44.5 MeV/nucleon	0.693
28.2 MeV/nucleon	0.724	48.4 MeV/nucleon	0.685
33.1 MeV/nucleon	0.715	53.5 MeV/nucleon	0.674
38.3 MeV/nucleon	0.702	57.6 MeV/nucleon	0.667

3.4 Summary

In this chapter, the method for assigning Au+Au events to impact parameter bins was presented, as well as the technique used to estimate the reaction plane. Up to this point in the thesis, experimental results have not been shown. Chapter 4 outlines the search for the disappearance of directed flow in Au+Au collisions and what can be learned from it. Chapter 5 contains a detailed study of the cross-over of elliptic flow at NSCL beam energies.

Chapter 4

Disappearance of Directed Flow in Au+Au Collisions

As often happens in experimental physics, some of the results are not anticipated. This adage certainly holds true for the contents of this chapter. The initial motivation for studying the disappearance of directed flow for Au+Au was to extend its system mass dependence and investigate whether it could be measured at all (see Section 4.2.3). But the more valuable findings concern the effect of the Coulomb interaction on the balance energy (Section 4.5) and the isolation of the nuclear equation of state with the balance energy for Au+Au (Section 4.6).

This chapter begins with a chronological history of directed flow, which was defined and introduced in Section 1.5.1. Then, the motivation for an Au+Au experiment at the NSCL is outlined. After presenting the experimental data and reconciling the data with measurements made over a wide range of energies, model calculations based on Boltzmann-Uehling-Uhlenbeck theory are discussed and compared to data. The result is a powerful statement about the utility of studying Au+Au collisions at intermediate energies.

4.1 History of Directed Transverse Flow

The idea that a nuclear shock wave could be formed in compressed nuclear matter was first proposed in 1959 by Glassgold[1], Heckrotte, and Watson [45], who were studying nuclear theory at University of California-Berkeley's Radiation Lab . They proposed a way to determine the nuclear compressibility coefficient by using the angular distribution of the emitted fragments, remarkably similar to the work of the present thesis. However, they limited their study to the passage of protons and pions through a heavy target nucleus, since beams of heavy ions were still on the horizon.

The idea of nuclear shock waves remained largely unnoticed until the early 1970s, when the theoretical emphasis on heavy-ion collisions mirrored the parallel developments in accelerators [46]. Most of the theoretical work assumed that hydrodynamic effects led to the formation of a shock wave propagating in the beam direction. In 1974, the importance of expansion in the *transverse* direction was first suggested by Scheid[2], Müller, and Greiner [47] at the University of Frankfurt. Using the $^{16}O+^{16}O$ system, they showed that compressed nuclear matter expanded faster in the transverse direction than in the longitudinal direction at beam energies as low as 13 MeV/nucleon.

The model they proposed was very simple: two identical nuclei that collide at zero impact parameter (i.e. head-on) form a region of compression which is ellipsoidal in shape, and the regions inside and outside the ellipsoid can be treated separately (see Figure 4.1). By expressing the velocity field of the ellipsoid in terms of the ellipsoid's dimensions and by satisfying boundary conditions, the ellipsoid is seen to expand faster transverse to the relative movement of the nuclei for low energies. However, as beam energy is increased, the longitudinal direction's expansion velocity

[1] A.E. Glassgold is now a professor of theoretical astrophysics at New York University and was unaware that his work as a post-doc at Berkeley was partly responsible for the growth of an entire field.

[2] Werner Schied is now a professor at the University of Giessen, Germany.

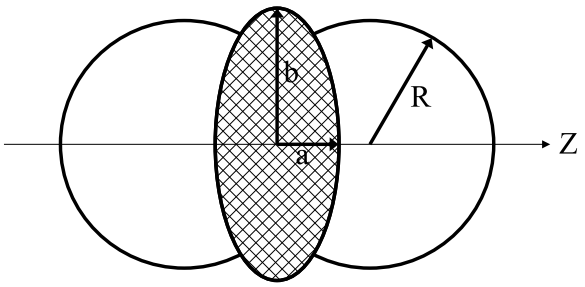

Figure 4.1: The geometrical parameters of the simple model used by Scheid, Muller, and Greiner to predict transverse expansion are shown. The component of the velocity field in the compressed (hashed) region in the direction of **b** represents transverse expansion.

overtakes the transverse direction. They concluded that measuring the longitudinal and transverse components of the velocity as a function of beam energy can be a powerful experimental probe of the compression region.

The importance of the seminal work by Scheid *et al.* was two-fold. First, transverse expansion of the compressed region meant that nuclear matter could reach detectors uninhibited by nucleons in the uncompressed regions, which travel mostly in the direction of the beam. Detectors with near-4π coverage, such as the detector array used in this thesis, would be very useful for detecting the transverse matter. Second, although they used ^{16}O+^{16}O, a relatively light system, for their calculations, the results of the simple geometrical model were valid for all symmetric systems (such as Au+Au), so that a systematic study of emission patterns could yield information about the nature of the compressed region.

The need for experimental data was clear, because the shapes predicted by hydrodynamical and intranuclear cascade calculations were quite different. The hydrodynamical model predicted ellipsoidal shapes which were oriented along the beam axis for peripheral collisions and nearly perpendicular to the beam axis for central collisions [48]. On the other hand, cascade calculations (which do not include a nuclear mean field) predicted no flow at all impact parameters [49].

It wasn't until the mid-1980's that the first convincing experimental evidence for directed transverse flow appeared. The Streamer Chamber and the Plastic-Ball/Wall at Berkeley were both 4π detectors that could fully characterize events by identifying and measuring the momenta of most of the emitted charged particles [25]. Using the *sphericity method* in which a kinetic energy tensor is formed to represent the shape of the collision, data from both detectors showed enhanced emission perpendicular to the beam direction in Ca+Ca and Nb+Nb collisions at 400 MeV/nucleon [21, 50]. The excitement of the finding was evident in the quick theoretical corollary: the very next paper in *Physical Review Letters* following the Streamer Chamber result was a theoretical analysis of the data by Buchwald *et al.* [51] at Frankfurt, confirming a long series of predictions based on fluid dynamics. Interestingly, the Plastic Ball data, which came earlier than the Streamer Chamber result, was rejected by *Physical Review Letters.*

The fundamental technique for analyzing directed flow is due to the work of Danielewicz[3] and Odyniec at Berkeley. In 1985, they published the *transverse momentum method* [52] in which the transverse momenta of detected particles on an event-by-event basis are used to determine the reaction plane and collective transverse motion in the collision. The strength of the transverse "flow"[4] was seen to be stronger than predicted by the cascade model, but weaker than in the hydrodynamical model.

The mid-1980's witnessed the advent of microscopic transport models specifically designed to overcome one of the possible shortcomings of fluid dynamics, the unrealistic assumption of local equilibration. This assumption is unphysical during the *freeze-out* phase when the nuclear matter has expanded to a density lower than normal nuclear density. Numerical simulations based on Boltzmann-Uehling-Uhlenbeck

[3]Pawel Danielewicz is now a professor at Michigan State University.

[4]The use of the term *flow* probably can be ascribed to Horst Stöcker *et al.*, who in 1980 used the term "collective sideward flow" in the title of a *Physical Review Letters* paper [53].

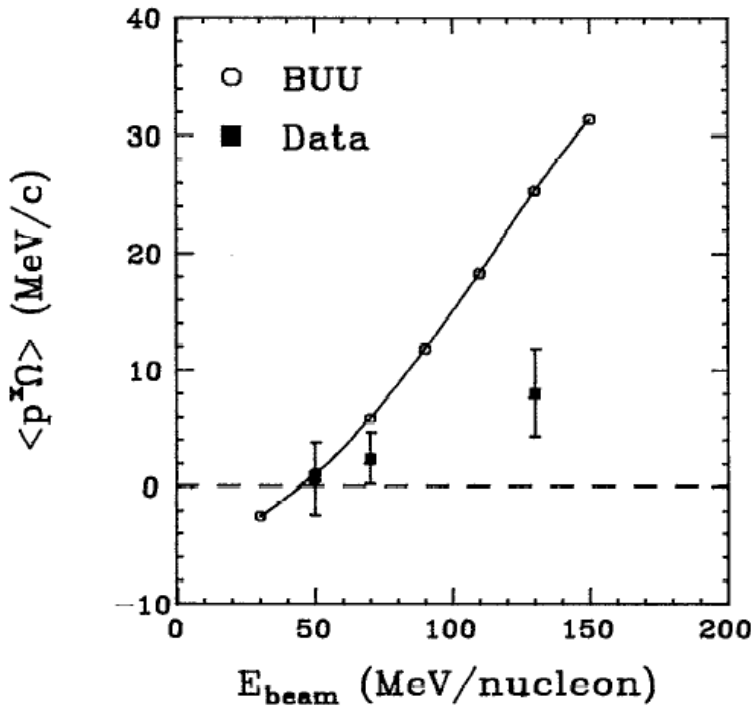

Figure 4.2: First experimental evidence for the disappearance of directed transverse flow [56]. Data are taken for the ^{139}La+^{139}La system with the MSU charge-coupled device camera.

(BUU) [54] and Quantum Molecular Dynamics (QMD) [55] models avoid the assumption of equilibration by describing microscopically the evolution of excited nuclear matter from a non-equilibrium state into one that is possibly thermal [25]. Aided by faster computers which can propagate the movements and interactions of a large number of particles in very small time steps, BUU and QMD codes include an approximation of the nuclear mean field (see section 4.6), which is directly related to the nuclear equation of state.

The disappearance of directed flow, which is the subject of this chapter, was first observed for ^{139}La+^{139}La collisions in digital streamer chamber photographs by Krofcheck[5] *et al.*, using the MSU charge-coupled device camera system [56]. The disappearance was attributed to the gradual dominance of the attractive part of

[5]D. Krofcheck is a professor of physics at the University of Auckland, New Zealand.

the nuclear mean field as the beam energy is lowered to several tens of MeV/nucleon. Krofcheck showed that the energy of zero flow agreed well with predictions from BUU calculations (see Figure 4.2). However, as shown by Bertsch[6], Lynch, and Tsang at MSU, the value of the nuclear compressibility and the in-medium nucleon-nucleon cross section both affect the buildup of compression at these energies. The apparent dual dependence of the *balance energy*[7] made the prospect of extracting information about the equation of state difficult.

In the past nine years, the field of directed transverse flow has grown and spans an energy regime of nearly five orders of magnitude (about 30 MeV/nucleon to 200 GeV/nucleon). At low energies, the mass dependence [57], impact-parameter dependence [58], and isospin dependence [59] of the balance energy (for light- and medium-sized systems) have provided useful comparisons of experimental data to transport models. Some phenomena uncovered include the momentum-dependent nuclear mean field [60] and the reduced in-medium nucleon cross section [57]. The low-energy results relevant to the analysis presented in this chapter will be discussed in greater detail in the following sections.

At higher energies, the study of directed flow has grown to include flow of produced particles, such as pions and kaons. Some of the high energy results have been very unexpected. In Ne+Pb collisions at 800 MeV/nucleon, The Diogène Collaboration at Saclay, France, showed that charged pions exhibit positive transverse momentum $\langle p_x \rangle$ values for all rapidities [61], indicating that they are preferentially emitted towards the light projectile and away from the heavy target side of the collision. The EOS Collaboration at Berkeley and the FOPI Collaboration at Darmstadt, Germany, found that directed flow of Λ particles follows the flow patterns of nucleons, while K^+ show

[6]George Bertsch, a former professor at MSU, is now a Senior Fellow in the Institute for Nuclear Theory and professor of physics at the University of Washington. Dr. Bertsch is also Editor, *Reviews of Modern Physics*.

[7]The term *balance energy* first appeared in a paper by Ogilvie *et al.*. Craig Ogilvie was a postdoc at MSU during 1988-90.

very little flow. A discussion of the implications of these "strange" results can be found in Reference [25].

More recently, directed flow measurements by collaborations at AGS and CERN have been published [71, 27]. Since the onset of new phases or new and exotic forms of matter is reflected in the equation of state, a study of the energy dependence of directed flow is warranted. Motivating the study, Rischke used a relativistic hydrodynamic model to suggest that the QCD phase transition will coincide with a minimum (or maybe a zero) in the directed flow excitation function, which he predicted to be around 100 GeV/nucleon [62]. The study of directed flow at the Relativistic Heavy Ion Collider at Brookhaven, which will go on-line in the coming months, could be used to understand the transition to a quark-gluon plasma. Much remains to be learned.

4.2 Motivation for Au+Au Experiment at NSCL

As stated in the introductory chapter, one of the primary goals of the study of nuclear reactions is to obtain information about the nuclear equation of state (EOS) as well as characteristics of bulk nuclear matter. The "bulk" in *bulk nuclear matter* is a stumbling block for experimentalists and theorists alike. Theorists are hindered by the large computational requirements of simulating nuclear matter of any appreciable size, since the complexity of the numerical simulation increases considerably as the number of nucleons increases. Experimentalists are limited by the number of isotopes available to collide.

The Au+Au system, which has 394 nucleons, is nearly the closest to infinite nuclear matter we can create in the laboratory (and away from any star, for that matter). Many of the world's past and future accelerators ran Au+Au experiments due to its large size: the Bevalac at Berkeley, SIS at GSI in Darmstadt, the Alternating Gradient Synchrotron (AGS) at Brookhaven, and (soon) the Relativistic Heavy Ion

Collider (RHIC) at Brookhaven. The SPS at CERN chose to run ^{208}Pb+^{208}Pb, a slightly larger system. With planning underway for a next-generation radioactive beams facility which will accelerate uranium beams [1], the potential for $A > 450$ reactions exists. However, the Au+Au system is the system of popular choice for another reason: it is isotopically pure in nature, making it less expensive than other heavy elements (such as lead) that need to be isotopically purified. The purity of the projectile and target is particularly important for studying directed flow because the flow analysis is done in the center of mass, and variations in the system mass introduce error bars in the transformation. As an added benefit, gold is the most malleable metal, allowing for thin targets to be made with relative ease.

4.2.1 Extension of the Mass Dependence of E_{bal}

As mentioned at the outset of this chapter, the initial purpose for performing an Au+Au experiment at the NSCL was to study the balance energy for a heavy system and extend the mass dependence of the balance energy beyond ^{86}Kr+^{93}Nb. The prospect of studying Au+Au collisions over the energy range necessary to measure the balance energy was made possible by ion source developments and corresponding A1200 calculations which showed that the high charge states needed to produce high energy Au beams could produce sufficient currents.

Figure 4.3 shows the mass dependence of the balance energy, obtained with the 4π Array and published in 1993 [57]. Solid squares are experimental data, and open points are Boltzmann-Uehling-Uhlenbeck model calculations from Ref. [18] (see Section 4.4 for a discussion of the BUU model). The balance energy is seen to decrease as the system mass is increased, in agreement with the calculations. The lines in the figure represent power law fits of the form $E_{bal} \propto A^{-\tau}$, and the solid line corresponds to $\tau = 1/3$. A simple scaling argument suggests the power law relationship arises

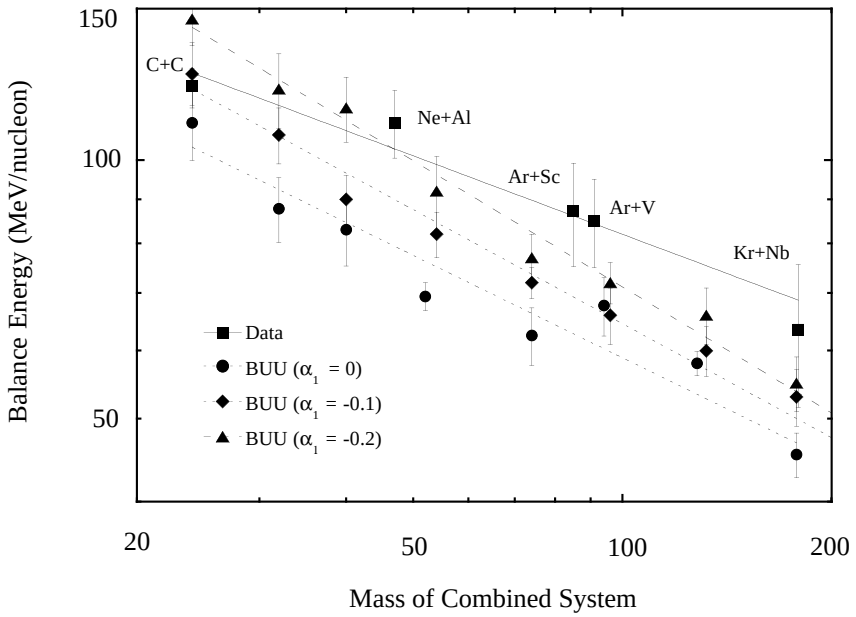

Figure 4.3: Previously published mass dependence of the disappearance of directed transverse flow [57]. Data are taken using the 4π Array at the NSCL, and BUU model calculations are from Ref. [18].

from two terms: the nuclear mean field, which scales roughly with the surface area of the nuclei, $A^{2/3}$; and the repulsive nucleon-nucleon scattering, which scales with the number of nucleons present in the collision, A. However, visual inspection of Fig. 4.3 shows that the value of τ in the power law fit may increase as the system mass increases. Extending the mass dependence of $E_{\rm bal}$ to Au+Au is useful for understanding the trend.

4.2.2 Previous Studies of Directed Flow for Au+Au

Another motivation for studying directed flow in Au+Au collisions at the NSCL is to add to an already extensive set of data which spans several orders of magnitude in beam energy. Flow measurements at intermediate energies can be compared with flow data taken at SIS, AGS, SPS, and (soon) RHIC, and it is hoped that a complete *flow excitation function*, or flow *vs.* beam energy plot, would provide insight. In order to plot finite flow values from different experiments on the same graph, dispersion in

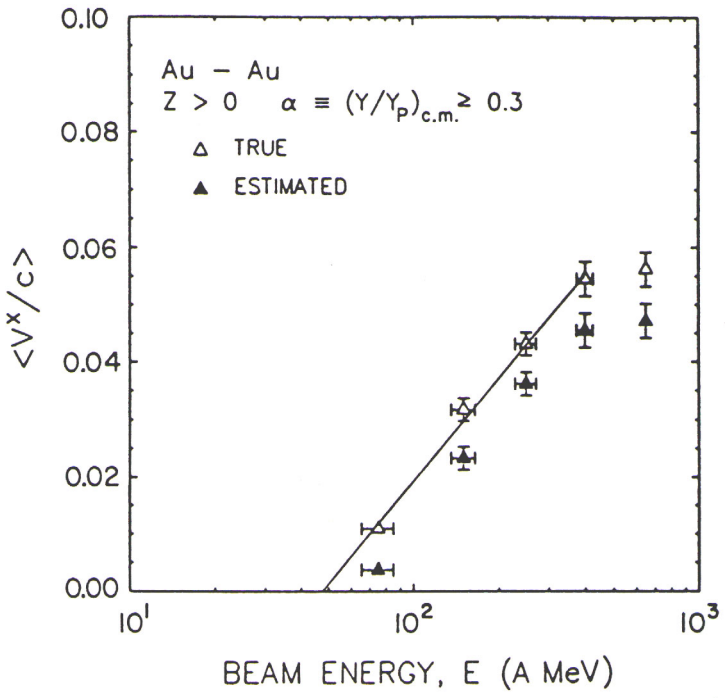

Figure 4.4: Energy dependence of directed flow for data taken with a plastic wall array at Berkeley [64]. An extrapolated a value of $E_{\rm bal} = 47 \pm 11$ MeV/nucleon was obtained using a logarithmic fit.

the experimental reaction plane needs to be corrected for in a consistent manner (see Section 3.3.3 and Appendix A).

Since the balance energy for Au+Au is a significant feature of the flow excitation function, three collaborations previously estimated the value of $E_{\rm bal}$ by extrapolating from flow measurements taken at higher beam energies. Using a plastic wall array at the Bevalac, Zhang *et al.* [64] measured the average in-plane transverse velocities and corrected for the reaction plane dispersion by adopting the method of Ref. [52]. They obtained a value of $E_{\rm bal} = 47 \pm 11$ MeV/nucleon by fitting data between 75 and 400 MeV/nucleon to a logarithmic function (see Figure 4.4). However, the large error was associated only with the uncertainty in the interaction energy of the collision between the projectile and the target. Inspection of Fig. 4.4 shows that the magnitude of dispersion correction affects the extrapolated balance energy greatly.

The EOS Collaboration measured directed flow in Au+Au collisions at the Bevalac

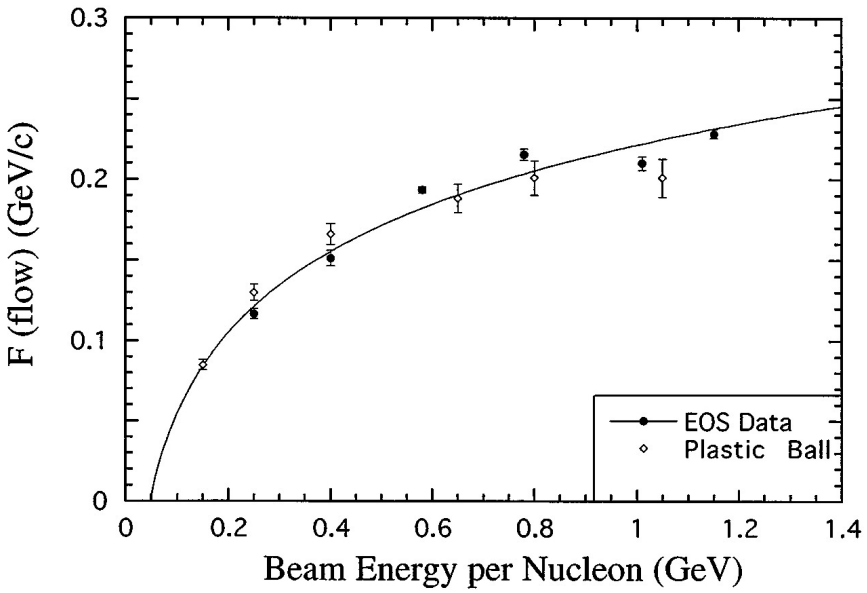

Figure 4.5: Energy dependence of flow for EOS data [65] and Plastic Ball data [63]. The EOS data extrapolated a value of $E_{\rm bal} = 47 \pm 5$ MeV/nucleon using a logarithmic fit.

with beam energies ranging from $0.25A$ to $1.15A$ GeV [65]. By comparing their results with a quantum molecular dynamics model, they found that neither the "soft" nor the "hard" equation of state described the data over the entire range of beam energies. Figure 4.5 shows their data plotted together with data from the Plastic Ball [63]. All of the data is for a semi-central impact parameter bin. Like Zhang *et al.*, they extrapolated $E_{\rm bal}$ for Au+Au by fitting their dispersion-corrected flow parameters to a logarithmic function and measuring the abscissa. They obtained a value of 47 ± 5 MeV/nucleon.

Most recently, the FOPI Collaboration at GSI in Darmstadt measured the excitation function of directed flow at seven incident energies between $E_{\rm beam} = 100$ MeV/nucleon and $E_{\rm beam} = 800$ MeV/nucleon. Figure 4.6 shows the flow (in this case, normalized by fragment mass) in semi-central collisions for four different fragment types, $Z = 2 - 5$. The solid lines correspond to fits to the data points up to 400 MeV/nucleon with Fermi functions. All of the extrapolated balance energies are

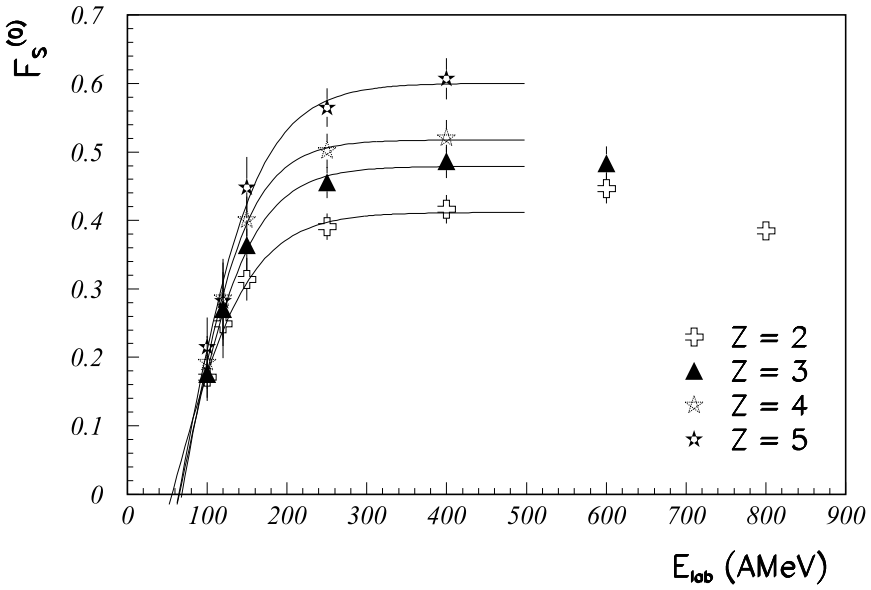

Figure 4.6: Energy dependence of flow for FOPI data [66]. For $Z = 2$ fragments, a value of $E_{\rm bal} = 56 \pm 21$ MeV/nucleon is extrapolated using a Fermi function fit.

within error bars, and for $Z = 2$, $E_{\rm bal} = 56 \pm 21$ MeV/nucleon.

In all previous studies of Au+Au, the balance energy was obtained by extrapolating the abscissa from flow measurements at higher energies. However, dispersion in the experimental reaction plane affects non-zero flow values, which in turn affect a fit's intersection with the x-axis. In addition to the energy-dependent nuclear interactions that cause the flow, the increased role of the Coulomb interaction could alter the functional trend at low beam energies, as discussed in the next section.

4.2.3 Can the Balance Energy Be Measured for Au+Au?

For light- to medium-sized systems, the balance energy arises from the balancing of the repulsive nucleon-nucleon scattering and the attractive nuclear mean field potential (see Section 1.5.1). However, as the system mass is increased, long-range repulsion between projectile and target increases due to the Z^2 dependence of the Coulomb interaction. Also, since the mass dependence predicts a lower $E_{\rm bal}$ for heavy systems, the Coulomb interaction should play a stronger role.

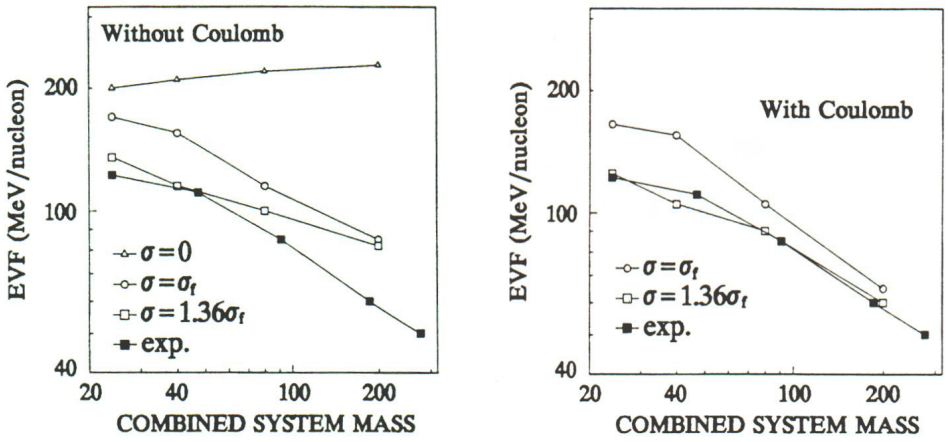

Figure 4.7: Vlasov-Uehling-Uhlenbeck calculations by Zhou *et al.* [67] of the mass dependence of the balance energy with and without the Coulomb interaction included. Experimental data are from the 4π Array.

The influence of Coulomb forces on $E_{\rm bal}$ was first studied by Zhou *et al.* [67], using model calculations based on the Vlasov-Uehling-Uhlenbeck (VUU) approach in which the mean field is determined by the coupling constants between nucleons and mesons. The energy of vanishing flow was a result of the complex interplay between nuclear and Coulomb forces, even for medium-sized systems. Figure 4.7a shows the experimental mass dependence of $E_{\rm bal}$, taken from 4π Array data, and the result of VUU calculations without the Coulomb interaction. A *soft* EOS is used. One can see that $E_{\rm bal}$ decreases slowly as a function of system mass. With Coulomb included, as in Fig. 4.7b, the mass dependence of the VUU-calculated balance energy decreases more rapidly, as expected. The calculations were carried out for system sizes up to $A = 200$.

An interesting prediction arose from quantum molecular dynamics (QMD) calculations performed by Soff *et al.* at the University of Frankfurt [68]. They regarded the existence of negative flow, and therefore of a balance energy, for Au+Au as an open question due to the strong Coulomb repulsion. Figure 4.8 shows the transverse momentum p_x as a function of the reduced rapidity $y/y_{\rm proj}$, the slope of

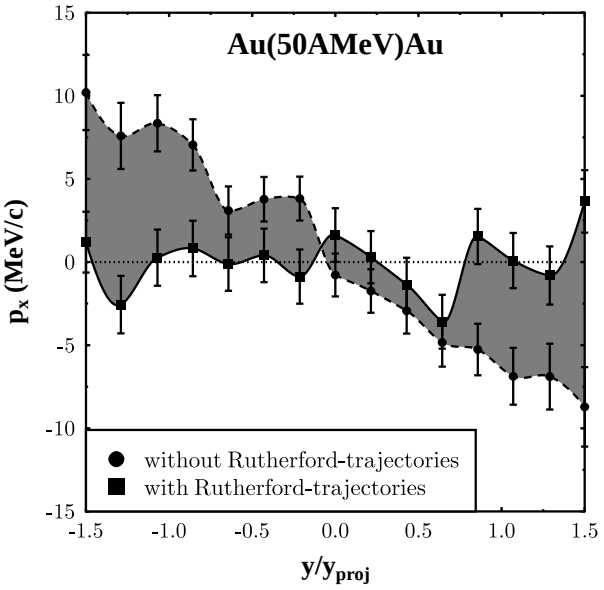

Figure 4.8: Transverse momentum p_x as a function of the reduced rapidity $y/y_{\rm proj}$ for quantum molecular dynamics calculations of Au+Au at 50 MeV/nucleon by Soff *et al.* [68]. Squares represent calculations in the lab frame, circles are calculations in a rotating Rutherford frame.

which corresponds to the directed transverse flow (as discussed in the next section). When Coulomb interactions are included in the QMD calculation (labeled "with Rutherford-trajectories" in the figure), the transverse momentum is nearly flat at 50 MeV/nucleon. But when the projectile's motion due to the long-range Coulomb interaction is accounted for, a negative slope is recovered, representing overall attractive collision dynamics. In effect, the reference frame becomes a rotating reference frame so that Coulomb influence is removed. The conclusion that Soff *et al.* reached was that $E_{\rm bal}$ could not be observed experimentally because Coulomb effects would overwhelm the low-energy attractive regime of the flow excitation function.

In their 1997 review of collective flow [25], Reisdorf and Ritter pointed to the importance of determining the balance energy for Au+Au.

> For very heavy systems such as Au+Au, efforts to determine the balance energy so far are inconclusive, since the balance energy has not been

reached experimentally... Coulomb effects are not negligible and could change the simple size scaling considerations (of the mass dependence of $E_{\rm bal}$) made before.

In this chapter, experimental evidence for the balance energy is presented. In addition, Boltzmann-Uehling-Uhlenbeck (BUU) simulations are carried out to investigate the role that Coulomb interactions play in the collision dynamics. Also, using BUU calculations, $E_{\rm bal}$ for Au+Au is seen to be insensitive to both the impact parameter and the in-medium cross section, allowing the EOS parameter K, the nuclear compressibility, to be extracted for the first time.

4.3 Experimental Results

As discussed in Sec. 1.5.1 of the introductory chapter, the disappearance of directed flow occurs at an incident beam energy, termed the *balance energy*, where the attractive and repulsive dynamics of the collision balance each other. At low energies ($\sim$ 10 MeV/nucleon), the attractive part of the nuclear mean field dominates, leading to the deflection of matter to negative scattering angles. At higher energies ($\sim$ 150 MeV/nucleon), repulsive nucleon-nucleon scattering dominates and deflects matter to positive scattering angles. At the balance energy the attractive and repulsive interactions, which are both energy-dependent, cancel, leading to zero transverse flow in the reaction plane.

Physically the balance energy $E_{\rm bal}$ occurs when nuclear matter in the collision's overlap (or participant) region does not expand preferentially in a particular quadrant of the reaction plane. However, the balance energy should not be misunderstood to represent necessarily isotropic emission of participant matter in the transverse direction. Figure 4.9 shows a schematic representation of directed flow in the center-of-mass frame at incident energies below, at, and above $E_{\rm bal}$. At the balance energy,

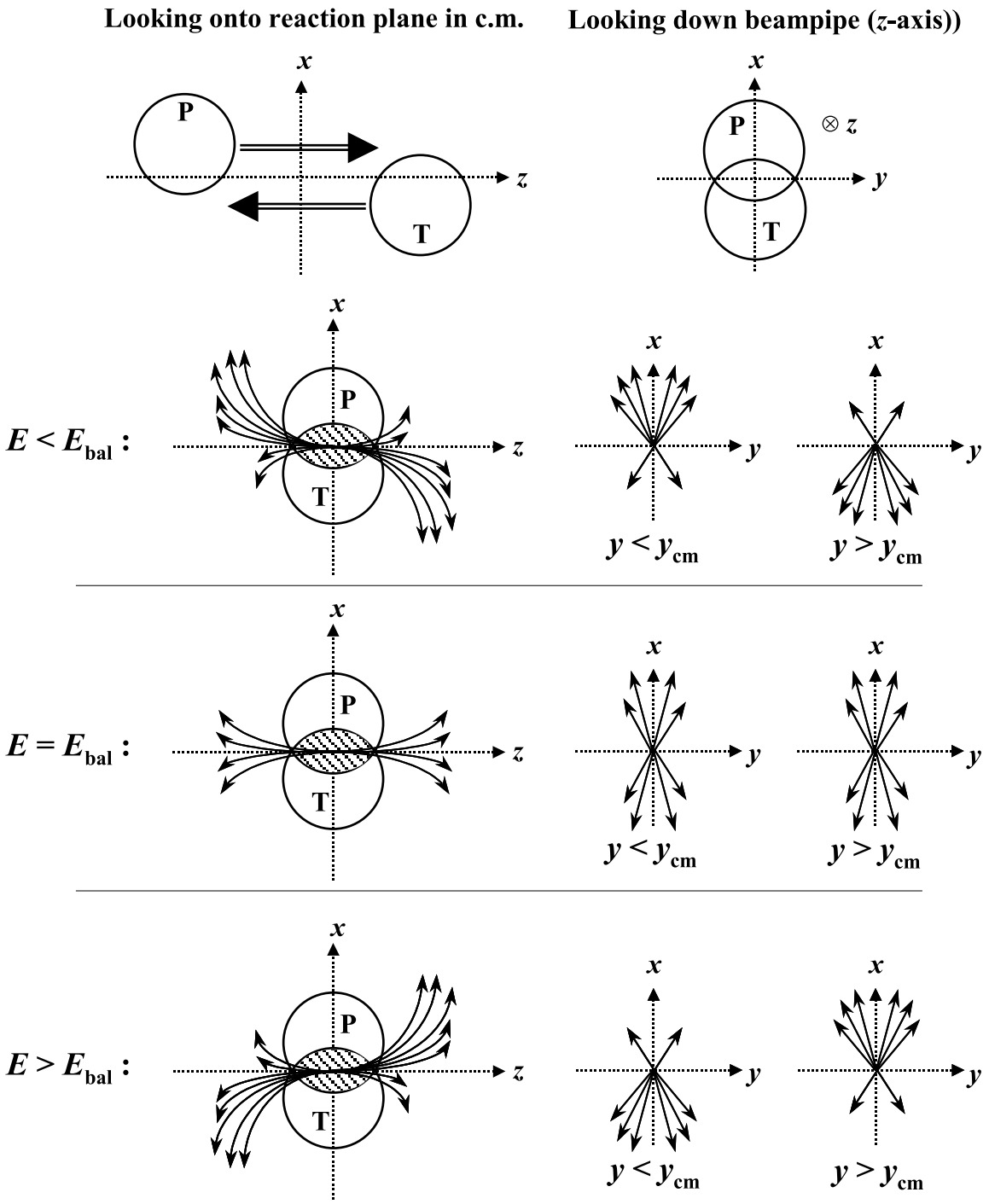

Figure 4.9: Schematic representation of directed flow at incident energies below, near, and above the balance energy. The left column is looking down on the reaction plane (x-z plane), and the right column is looking down the beampipe (z-axis). In the right column, particles are grouped by their rapidities to show the preferential emission of forward (backward) particles to positive (negative) angles.

emission at midrapidity is effectively symmetric about the y-axis, as expected from the balancing of the attractive and repulsive interactions. This corresponds to a fragment ϕ-distribution about the beam axis which is symmetric about $\pi/2$. As discussed in Sec. 5.3.1, it could be that the ϕ-distribution of participant fragments is never azimuthally symmetric for non-central collisions.

The utility of the balance energy is the ease with which experimental data can be compared to theoretical models. Since $E_{\rm bal}$ has been shown to be independent of particle type [57, 69, 58], the need for accurate fragment formation in the model is removed. And since the balance energy represents "zero" flow, experimental biases such as detector acceptance and reaction plane dispersion affect $E_{\rm bal}$ weakly [26]. That is not to say that these biases can be ignored, however, as discussed in the following paragraphs.

4.3.1 Caveats to Measuring the Balance Energy

Measuring directed flow requires determining the reaction plane as well as assigning the reaction plane *direction*. Direction can be taken to mean the side of the target that the projectile strikes or the direction that matter flows in the collision. Either way, determining the direction requires using the particles in the collision themselves, of course. The result is that one cannot differentiate between negative (attractive) and positive (repulsive) flow.

Figure 4.10 shows the difference between experimental and theoretical study of directed flow. Because the theorist knows the reaction plane *a priori*, he or she can assign negative flow correctly. However, the experimentalist only sees positive flow, based on the reaction plane direction's determination (see Sec. 3.2). Therefore, the balance energy corresponds to the minimum of the flow excitation function, as opposed to the crossover energy. Alternatively, the experimentalist can reflect

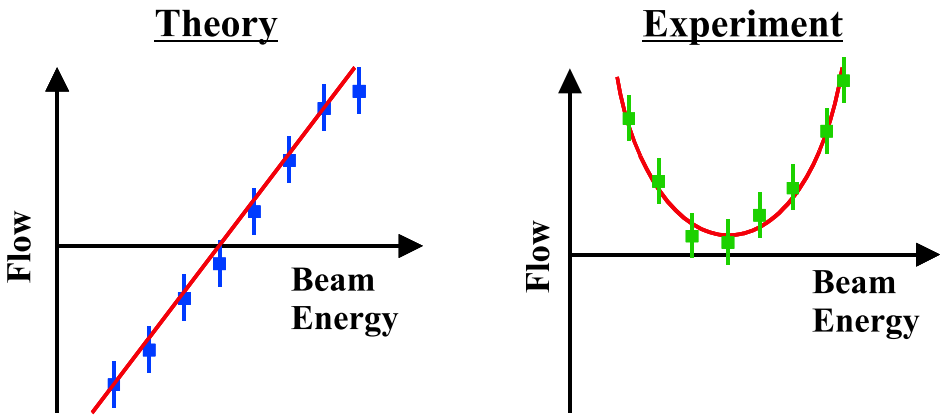

Figure 4.10: Directed flow near the balance energy, as determined by (a) theoretical and (b) experimental studies. Experimental studies of flow cannot discern between negative and positive flow because the reaction plane is determined using the same particles.

points below the minimum about the x-axis to represent the attractive regime, but a systematic error is introduced since there are one or two points whose reflection is questionable.

The other caveat to measuring the balance energy is the inherent difficulty of trying to measure "zero," since the flow should be zero at $E_{\rm bal}$. Because there are a finite number of particles in the collision, and because of imperfect detectors and imperfect angular resolution, detected flow will be nonzero even at the balance energy [52]. To circumvent this effect and to avoid autocorrelation, each detected particle is removed from the reaction plane determination (see Sec. 3.2), resulting in N separate reaction planes for an event with multiplicity N.

4.3.2 Transverse Momentum Analysis

The technique for extracting the directed flow at midrapidity is due to the work of Danielewicz and Odyniec [52] who first proposed transverse momentum as a way of isolating collective motion in high-energy nuclear reactions. Previous methods, such as two-particle correlations [70] and sphericity analysis [21], were hindered by

statistical fluctuations and finite-particle effects. In the case of sphericity analysis, where any anisotropy in the reaction is estimated by measuring how spherical the particles' momenta are on an event-by-event basis, it is easy to see that any spherical momentum distribution of a finite number of particles will yield a reaction plane and non-zero flow, even if generated randomly [52].

In contrast, the transverse momentum method successfully isolates collective motion by: 1) treating each particle individually and determining a reaction plane from the remaining particles; 2) separating participant and spectator matter in the collision by plotting *vs.* the rapidity; and 3) summing over many events to distinguish between statistical fluctuations and flow effects. The transverse momentum method has been the standard technique for virtually every directed flow analysis over the entire range of available beam energies.

The method is quite straightforward. For an event with N detected particles, each particle is treated as a "particle of interest" (POI) and removed from the determination of a reaction plane (see Sec. 3.2). In the reaction plane determination, a direction is assigned to be *positive* based on the summed transverse momenta of the particles. The transverse momentum $\mathbf{p}_i^{\perp}$ of the POI is then projected onto the reaction plane:

$$p_i^x = \mathbf{p}_i^{\perp} \cdot \hat{Q}_i, \tag{4.1}$$

where p_i^x is the transverse momentum of the POI and $\hat{Q}_i$ is the unit vector of the reaction plane for that POI. Since the reaction plane includes the z-axis, $\hat{Q}_i$ lies in the transverse plane (xy-plane in Fig. 4.9). Expressed another way,

$$p_i^x = |\mathbf{p}_i^{\perp}| \cos(\phi_i - \phi_i^{\mathrm{RP}}), \tag{4.2}$$

where ϕ_i and ϕ_i^{RP} are the azimuthal angles of the POI and the reaction plane, respectively.

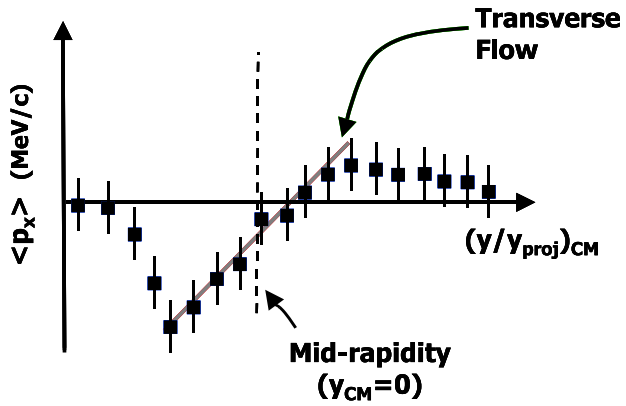

Figure 4.11: Schematic of the transverse momentum method for determining directed flow in symmetric nuclear collisions. The slope of a least-squares fit over a range of midrapidity $\langle p_x \rangle$ corresponds to the flow.

A strong flow signal is characterized by particles in the forward hemisphere of the reaction ($y_{\rm cm} > 0$) with mostly positive p_i^x's, and particles in the backward hemisphere ($y_{\rm cm} < 0$) with mostly negative p_i^x's. The rapidity for each POI is calculated and transformed to the collision's center-of-mass, and POIs are then placed into rapidity bins. For an experimental run with $N_{\rm run}$ particles of a certain type (such as p or α) and rapidity bin,

$$\langle p_x \rangle = \sum_{j=1}^{N_{\rm run}} \frac{p_j^x}{N_{\rm run}}, \tag{4.3}$$

where $\langle p_x \rangle$ is the average transverse momenta. Figure 4.11 shows a rough schematic of the transverse momentum method. $\langle p_x \rangle$ is plotted *vs.* $(y/y_{\rm proj})_{\rm cm}$, the center-of-mass rapidity normalized by the projectile rapidity. Under the useful normalization, $y_{\rm proj} = 1$ and $y_{\rm targ} = -1$. The directed transverse flow is defined as the slope of a least squares fit to $\langle p_x \rangle$ over the midrapidity region.

Before presenting the Au+Au transverse momentum analysis, detector acceptance effects need to be considered. To investigate acceptance effects on the analysis presented in this chapter, a two-dimensional histogram of p_i^x *vs.* $(y/y_{\rm proj})_{\rm cm}$ is generated for the data. Also, a simple event generator is used to simulate isotropic events which are passed through a software replica of the detector array, as discussed in Sec. 3.3.

Comparing the data to "filtered" isotropic events will uncover any unexpected acceptance issues.

Figure 4.12 shows the two-dimensional acceptance plots for (a) 38.3 MeV/nucleon Au+Au data, (b) unfiltered simulated isotropic events boosted to 40 MeV/nucleon, and (c) filtered isotropic events. The acceptance at backward rapidities is hindered by detector energy thresholds. This is due to the low lab-frame energies that the particles at backward rapidity strike the detectors. Preliminary transverse momentum analysis showed a strong effect due to these acceptance effects. In particular, the direction of the deduced reaction plane was inaccurate, as judged by the negative slope of $\langle p_x \rangle$ obtained for all but the highest beam energy.

Therefore, to minimize acceptance bias, only particles in the forward hemisphere of the collision ($y_{\rm cm} > 0$) are used in the transverse momentum analysis presented here. Assuming forward/backward symmetry in the reaction, the $\langle p_x \rangle$ values are reflected about $y_{\rm cm} = 0$ for graphical purposes, and the least squares fit is carried out only for the actual (and not the reflected) $\langle p_x \rangle$. The practice of reflecting $\langle p_x \rangle$ values to regions of poor acceptance is very common at higher energies [66, 71].

Figure 4.13 shows the average transverse momentum $\langle p_x \rangle$ plotted as a function of the reduced rapidity for $Z = 2$ POI in Au+Au collisions at all of the available beam energies. Data are for the most central impact parameter bin ($\langle b/b_{\rm max} \rangle = 0.28$, see Sec. 3.1). In these plots, open squares represent experimental values, and closed squares are the experimental values reflected about $y_{\rm c.m.} = 0$ by assuming forward/backward symmetry. The error bars are statistical, and the solid lines correspond to linear least square fits for the midrapidity region $0.0 \leq (y/y_{\rm proj})_{\rm c.m.} \leq 0.5$. Fragments emitted in this region are emitted from the excited participant volume created by the projectile-target overlap. The slope of this fit is defined as the directed transverse flow, which is a measure of the amount of collective momentum transfer in

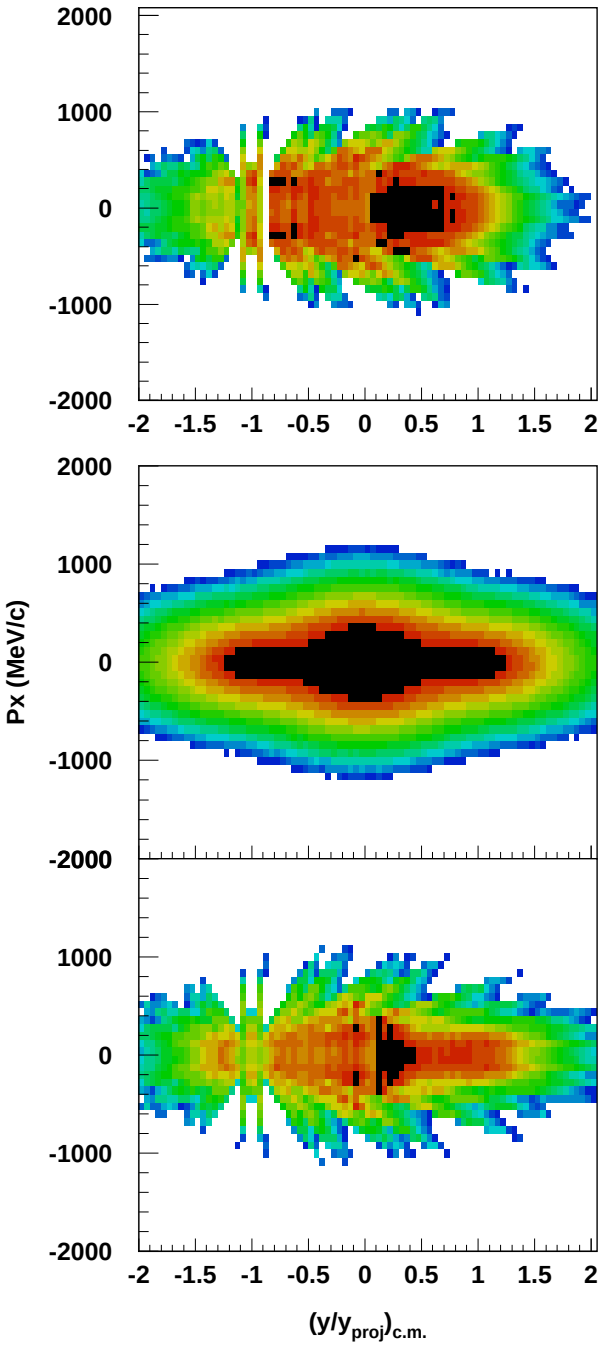

Figure 4.12: The acceptance of the 4π Array for Z=2 fragments in Au+Au collisions at 38.3 MeV/nucleon for: (a) data, (b) unfiltered isotropic simulation, and (c) filtered isotropic simulation. The acceptance is measured in terms of the transverse momentum p_x in the reaction plane vs. reduced c.m. rapidity. The detection efficiency is weak at backward mid-rapidity, and the effect is reproduced well by the software filter.

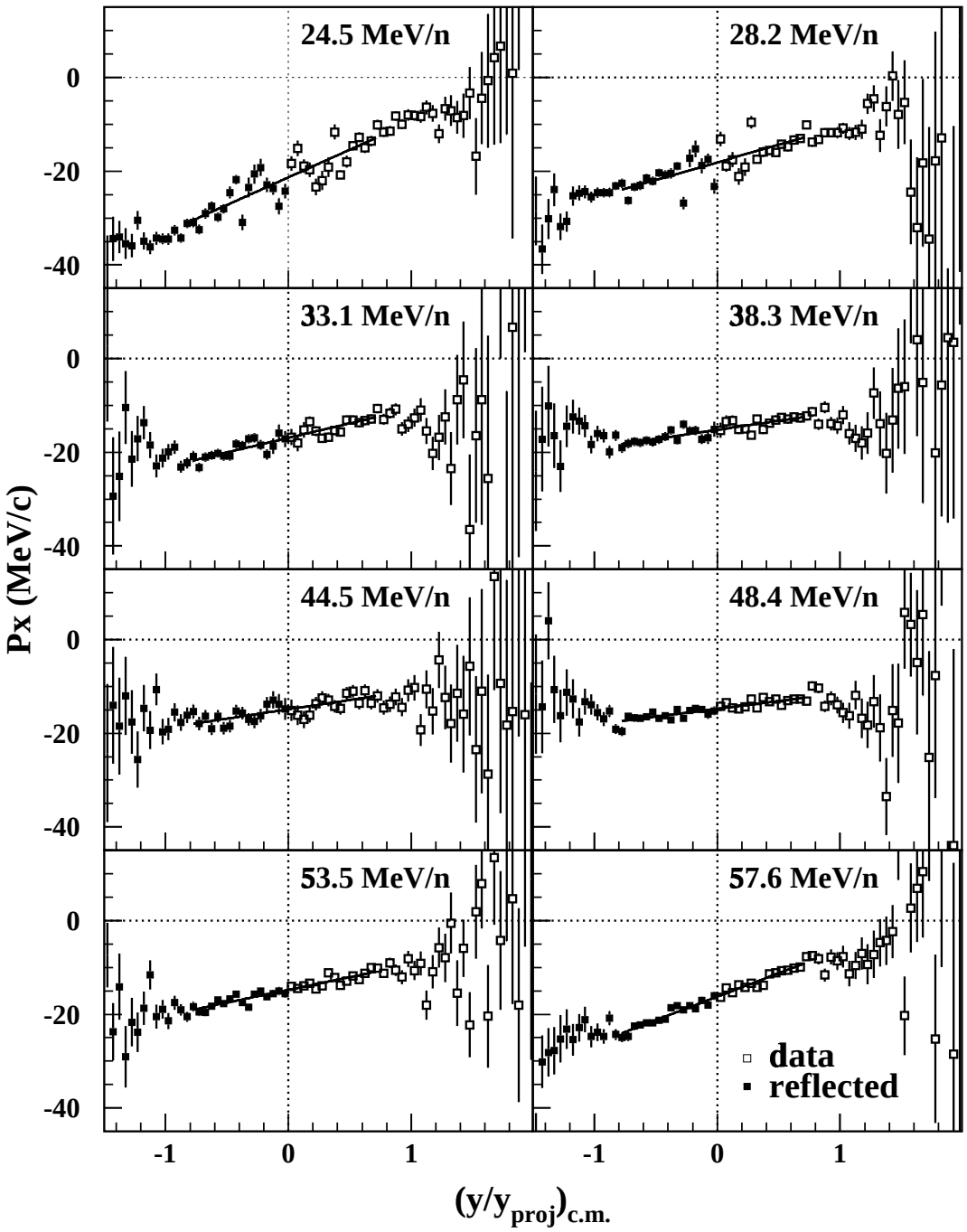

Figure 4.13: Average transverse momentum *vs.* the reduced rapidity in near-central Au+Au collisions ($\langle b/b_{\max}\rangle = 0.28$). $Z = 2$ is the flow particle of interest. Open squares are experimental measurements, and solid squares are reflections about $y = 0$ assuming forward/backward symmetry in the collision.

the collision. Clearly the slope is largest for the lowest ($E_{\rm beam} = 24.5$ MeV/nucleon) and highest ($E_{\rm beam} = 57.6$ MeV/nucleon) beam energies.

The transverse momentum is expected to pass through $p_x = 0$ at $y_{\rm c.m.} = 0$. The negative offsets in Fig. 4.13 has been seen previously in many systems [58, 26] and is attributed to two experimental biases. By removing the flow particle from the reaction plane determination (to avoid autocorrelation), an inherent lack of momentum conservation is present in the assigned reaction plane direction. However, this effect is small, because the 4π Array does not detect all particles. Furthermore, the expected reduction of this effect with increasing system mass is not seen experimentally.

A larger effect results from the likelihood of double hits in detectors which lie in the direction of the reaction plane. If a flow particle of interest (POI) is directed in the reaction plane, it is more likely to contribute to a double hit and be undetected than a POI directed to negative angles. This effect was seen in EOS data [72] and corrected by using negative-rapidity particle spectra and by considering the two-track resolution. However, these corrections are more difficult in a phoswich array such as the 4π Array, as the location of a particle cannot be pinpointed precisely enough; see Sec. 3.3.1.

Plotted in Figs. 4.14 and 4.15 are $\langle p_x \rangle$ *vs.* $(y/y_{\rm proj})_{\rm c.m.}$ for $Z = 1$ and $Z = 3$ POI fragments, respectively. For the case of $Z = 1$, $\langle p_x \rangle$ is nearly flat at midrapidity for all beam energies. This is attributed to weaker flow for lighter POI, as expected from previous experiments.

The extracted flow values (slopes from the transverse momentum plots) are plotted *vs.* incident beam energy in Figure 4.16 for $Z = 1, 2$, and 3. For $Z = 1$, the extracted flow is weak for all of the measured energies. This is partially due to the well-known fragment mass dependence of flow and the higher energy thresholds for $Z = 1$, since the Bragg curve counters in the main ball of the 4π Array do not detect these; see

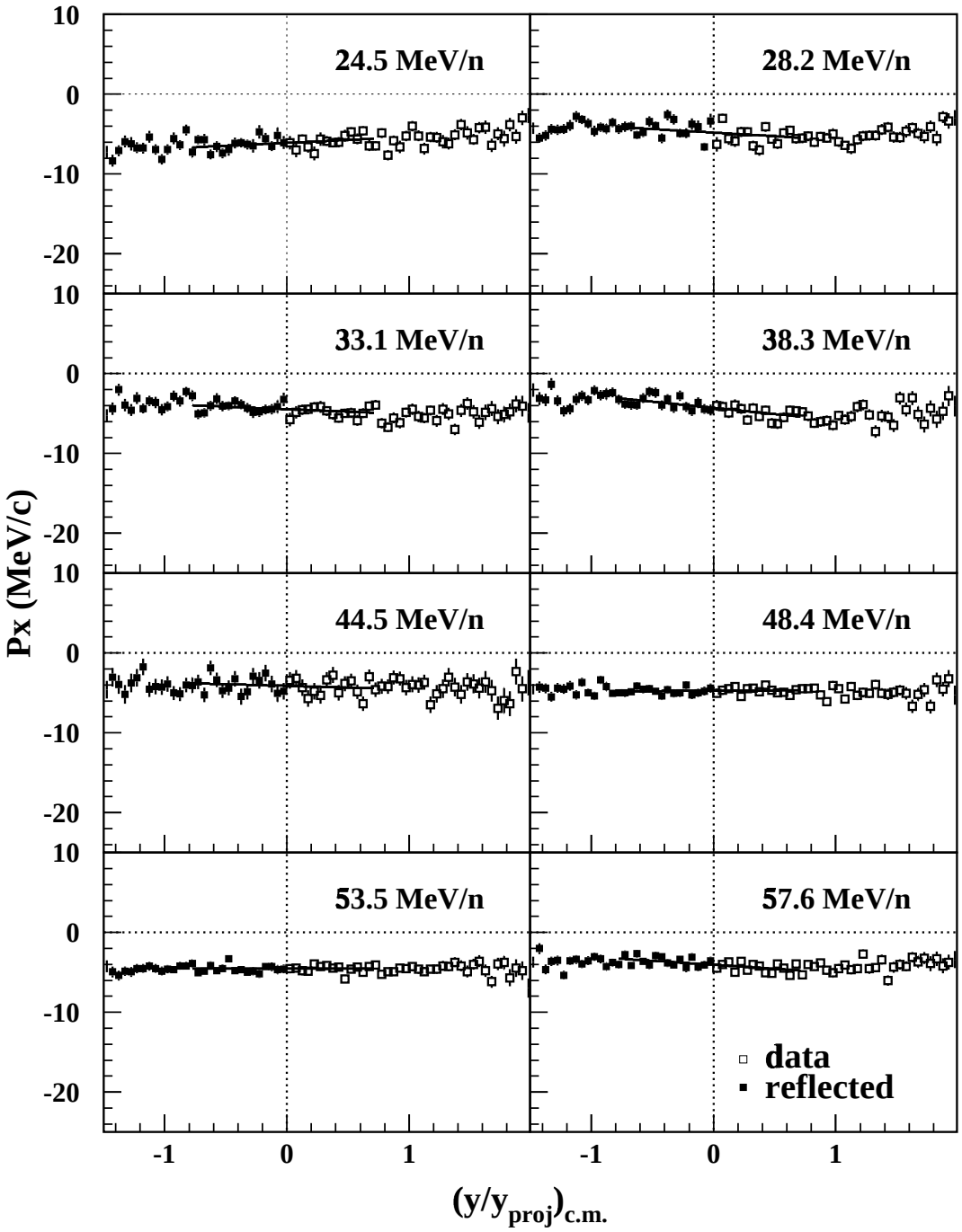

Figure 4.14: Average transverse momentum *vs.* the reduced rapidity in near-central Au+Au collisions ($\langle b/b_{\rm max}\rangle = 0.28$). $Z = 1$ is the flow particle of interest. Open squares are experimental measurements, and solid squares are reflections about $y = 0$ assuming forward/backward symmetry in the collision.

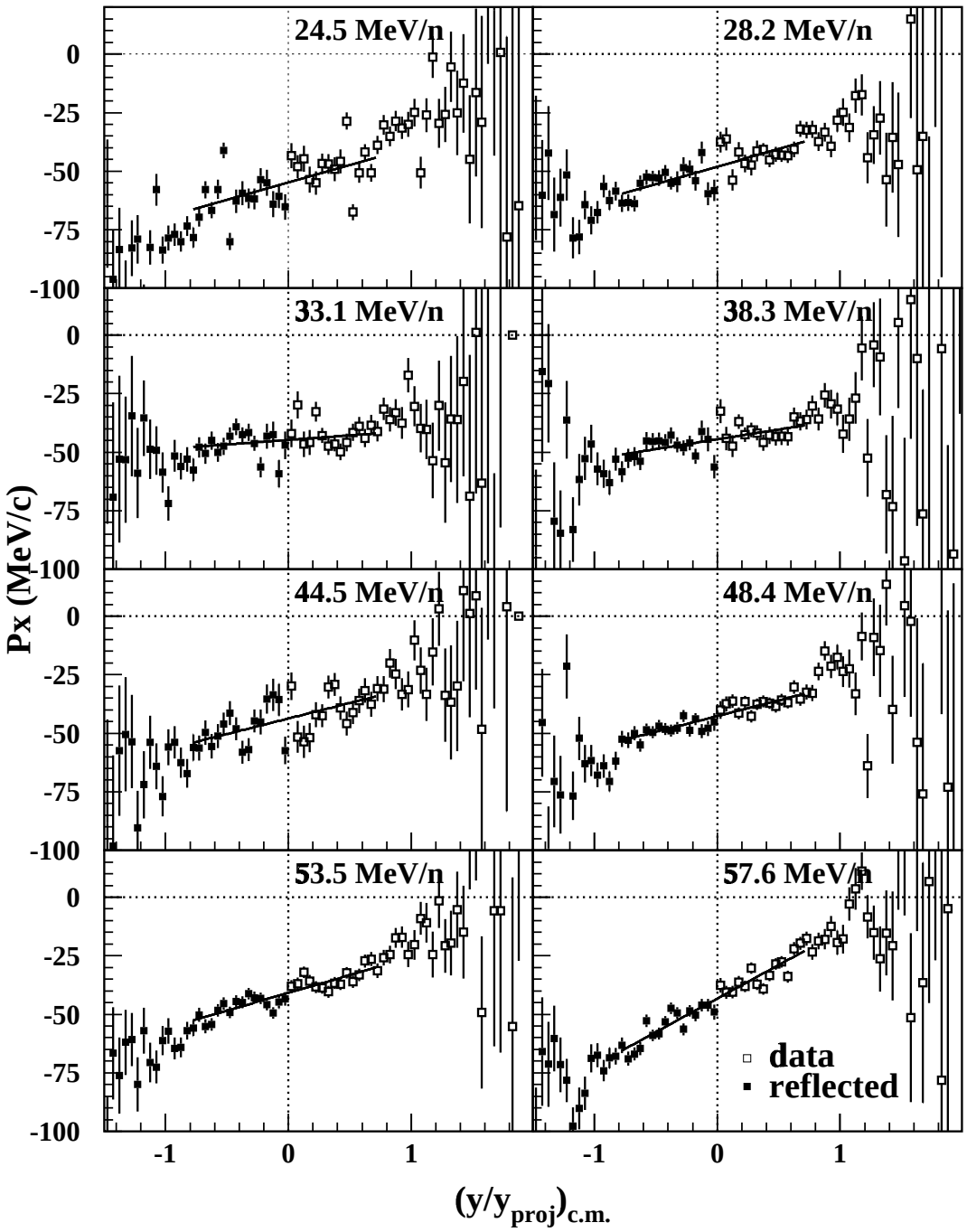

Figure 4.15: Average transverse momentum *vs.* the reduced rapidity in near-central Au+Au collisions ($\langle b/b_{\max}\rangle = 0.28$). $Z = 3$ is the flow particle of interest. Open squares are experimental measurements, and solid squares are reflections about $y = 0$ assuming forward/backward symmetry in the collision.

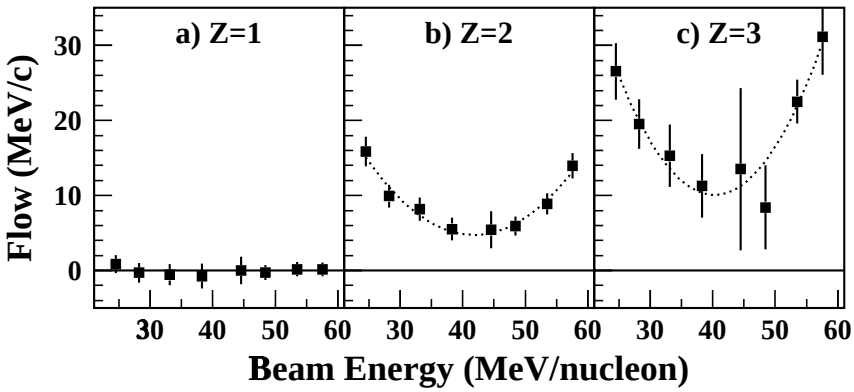

Figure 4.16: Extracted flow values in near-central ($\langle b/b_{\max} \rangle = 0.28$) Au+Au collisions for $Z = 1, 2, 3$ POI.

Sec. 2.2.1. However, for $Z = 2$ and $Z = 3$ the plot clearly shows that the flow goes through a minimum. Because measurements are unable to distinguish between the *negative* attractive scattering which dominates below E_{bal} and the *positive* repulsive scattering which dominates above E_{bal}, such a minimum is indicative of the balance energy for the system. The dotted curves are parabolic fits, included to guide the eye.

To assimilate the experimental data with theoretical predictions and to account for the attractive regime below the balance energy, the flow data below the minimum are reflected about the x axis and plotted in Figure 4.17. The dashed (solid) linear least squares fits are with the 44.5 MeV/nucleon data point reflected (not reflected). For $Z = 2$, this corresponds to a balance energy of 42.5 ± 3.5 (43.1 ± 3.6) MeV/nucleon. For $Z = 3$, the numbers are 41.6 ± 4.3 (41.9 ± 6.1) MeV/nucleon. The errors above are statistical. However, the use of two different fits introduces a small systematic error of 1 MeV/nucleon, resulting in a balance energy of 42 ± 4 MeV/nucleon. The balance energy for $Z = 3$ is the same as for $Z = 2$ to within error bars, in agreement with previous experimental studies that showed no dependence on particle type [57].

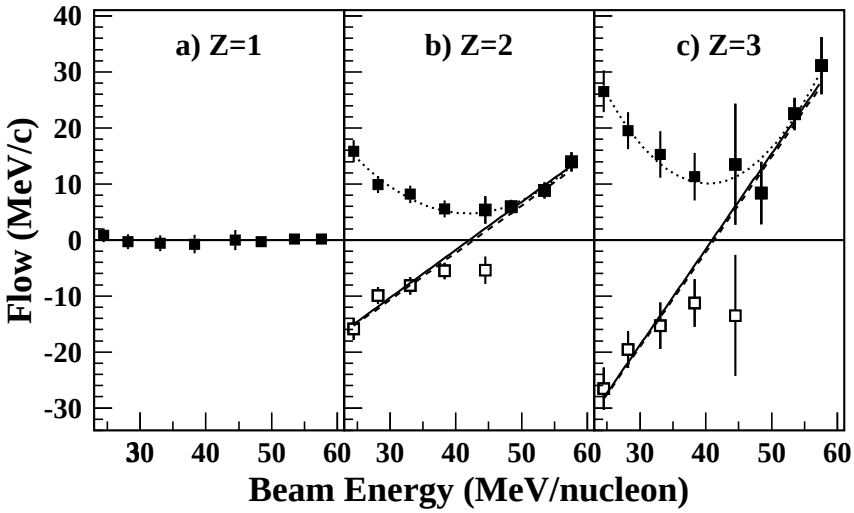

Figure 4.17: Extracted flow values in near-central ($\langle b/b_{\max}\rangle = 0.28$) Au+Au collisions for $Z = 1, 2, 3$ POI. Flow values below the minimum are reflected about the x-axis, and dashed (solid) lines represent linear least-squares fits with (without) the 44.5 MeV/nucleon value reflected.

4.3.3 Directed Flow Over a Wide Range of Energies

The 4π Array flow data presented to this point have been corrected for dispersion in the reaction plane determination, which arises from the fact that there are a finite number of particles in the collision. As discussed in Sec. 3.3.3, the dispersion correction leads to an increase in the measured amount of directed flow. Figure 4.18 shows the effect of the dispersion correction for $Z = 2$ POI. Solid squares indicate the experimental measurements from Fig. 4.16, and open squares are dispersion-corrected.

Once dispersion correction is made, the directed flow data presented in this chapter can be compared to Au+Au flow data taken over a wide range of energies. Table 4.1 lists other Au+Au experiments that have produced directed flow measurements over the past fifteen years. When plotting the various data on the same graph, it should be noted that small differences in analysis techniques are difficult to account for. Some of the differences present in a few of the experiments are:

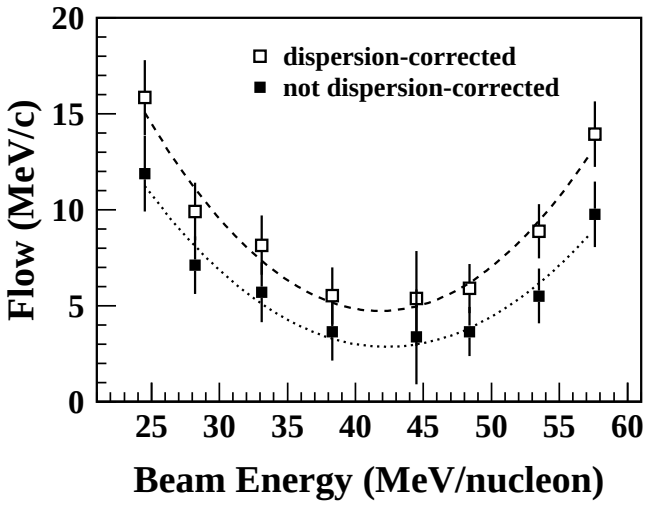

Figure 4.18: Experimental flow values for near-central Au+Au collisions with $Z = 2$ as POI. Solid squares are directly measured values, and open squares are corrected for dispersion in the reaction plane determination.

- impact-parameter binning
- dispersion correction method
- global experimental cuts on $p^{\perp}$ due to acceptance
- inclusion/exclusion of POI in reaction plane determination
- normalization of flow variable

Figure 4.19 shows the directed flow normalized by the fragment masses over the beam energy range $25A$ MeV to $11.8A$ GeV. The 4π Array data agree well with the general trend from higher energies. The flow excitation function appears to peak at $E_{\mathrm{beam}} \sim 2A$ GeV, and recent results from NA49 at CERN indicate near-zero directed flow in ^{208}Pb+^{208}Pb collisions at $E_{\mathrm{beam}} = 158A$ GeV [71].

Experiment	Location	Date	Energy Range	Reference
Plastic Wall/Ball	Berkeley	1983	150 AMeV - 1.05 AGeV	[50]
EOS TPC	Berkeley	1995	250 AMeV - 1.15 AGeV	[65]
FOPI	Darmstadt	1997	100 AMeV - 800 AMeV	[66]
E877	Brookhaven	1997	11.8 AGeV	[73]
E895	Brookhaven	1997	2 AGeV - 8 AGeV	[27]

Table 4.1: A list of the other Au+Au directed flow experiments included in the excitation function of Fig. 4.19.

4.3.4 Summary

In the remaining sections of this chapter, the BUU model is used to investigate two aspects of $E_{\rm bal}$ over the extended range of system mass: the increasing strength of the Coulomb interaction and its influence on the mass dependence, and the loss of sensitivity of the balance energy to both the impact parameter and the in-medium cross section. The latter is a significant finding, since the equation of state is isolated for the first time using the balance energy.

4.4 The BUU Model

The ability to extract information about the equation of state from studying nuclear collisions rests upon the agreement between observables found in experimental data and produced in numerical models. A model derives its strength from its ability to reproduce experimental quantities when initial conditions are varied. For example, it is well known that the total number of fragments produced in a collision increases with decreasing impact parameter, increasing beam energy, and increasing system size. A model that claims to simulate accurately fragmentation in nuclear collisions must reproduce these dependencies.

As discussed in Sec. 1.5, a numerical implementation of the Boltzmann-Uehling-

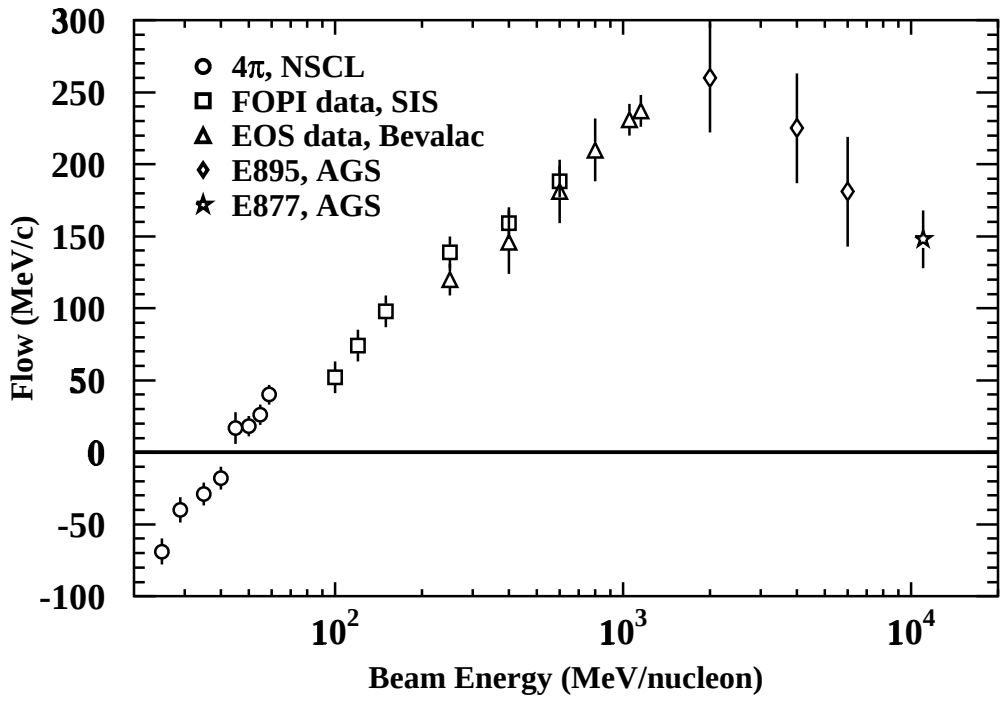

Figure 4.19: Directed flow normalized by the fragment masses plotted as a function of incident beam energy for several Au+Au experiments.

Uhlenbeck (BUU) model [54, 74] has been successful in reproducing various collective flow phenomena such as the balance energy. The BUU model propagates test particles (which represent nucleons in a collision) through phase space as they interact with each other via the *inter-nucleon potential*: a hard-core repulsion at short distances ($r \lesssim 1$fm), a strong attraction at intermediate distances ($1 \lesssim r \lesssim 2$fm), and a weak attraction at long distances ($r > 2$fm). The Pauli Exclusion Principle is approximated by monitoring the densities for both coordinate-space and phase-space. BUU is useful when the behavior of nuclear matter collectively is of interest; however, BUU does not coalesce nucleons into fragments and therefore is not suited to reproducing multiplicity distributions or fragment energy spectra.

In the current implementation, the inter-nucleon potential is split among two mechanisms: a nuclear mean field for low-momentum processes, and hard scattering for modeling the strong, repulsive, high-momentum processes. The form of the nuclear mean field potential $U(\rho)$ is

$$U(\rho) = a\left(\frac{\rho}{\rho_0}\right) + b\left(\frac{\rho}{\rho_0}\right)^{\sigma}, \tag{4.4}$$

where U represents the average of the potentials of the surrounding matter on a single nucleon. In Equation (4.4), ρ_0 is normal nuclear matter density, a is attractive, b is repulsive, and $\sigma > 1$. The parameters a, b, and σ are constrained by knowing the density ρ_0 and saturation binding energy of ground-state nuclear matter and by initializing all nucleons with the Fermi momentum p_F:

$$K = 9(\frac{p_F^2}{3m} + a + \sigma b), \tag{4.5}$$

where K is the compressibility of nuclear matter [54]. (See Sec. 1.2.1 for a discussion of the compressibility as the relationship between energy and density.) Typical values in the current study for the compressibility K are shown in Table 4.2 [19]. A *soft* EOS corresponds to $K = 200$ MeV, and a *hard* EOS corresponds to $K = 380$ MeV.

Model	K (MeV)	a (MeV)	b (MeV)	σ
Soft	200	-356	303	7/6
Medium	235	-218	164	4/3
Hard	380	-124	70.5	2

Table 4.2: Parameter sets used for the mean field U.

For a given value of K, $|a|$ is always greater than $|b|$. Therefore, when $\rho = \rho_0$, $U(\rho)$ is attractive. As ρ increases, the repulsive term increases in relative strength, and above a density

$$\rho = \left(-\frac{a}{b}\right)^{\sigma-1} \rho_0 \tag{4.6}$$

$U(\rho)$ is repulsive. This density-dependent effect contributes to the crossover from negative to positive flow with increasing beam energy.

The hard scattering of nucleons at short distances is parameterized by

$$\sigma_{\rm nn} = \sigma_{\rm free}\left(1 + \alpha\frac{\rho}{\rho_0}\right), \tag{4.7}$$

where $\sigma_{\rm nn}$ is the in-medium nucleon-nucleon cross section, $\sigma_{\rm free}$ is the nucleon cross section in vacuum, and α is a parameter between 0 and -1 [18]. The effect of reducing the cross section is to make nucleus-nucleus collisions less repulsive on average, since there are fewer collisions.

The compressibility K and in-medium cross section $\sigma_{\rm nn}$ are the main quantities of interest in the BUU model. It is hoped that K and $\sigma_{\rm nn}$ can be constrained by comparison to experimental data.

Modeling the Balance Energy with BUU

The BUU model is well-suited for investigating the energy dependence of directed flow, since the inter-nucleon potential is represented by density-dependent variables (K and $\sigma_{\rm nn}$). At low energies, the attractive portion of the nuclear mean field $U(\rho)$

dominates the collision dynamics, leading to negative directed flow in the reaction plane. BUU successfully reproduces this effect. Figure 4.20 shows BUU calculations in coordinate space projected onto the reaction plane for ^{40}Ar+^{45}Sc at an incident energy of 40 MeV/nucleon and a reduced impact parameter of $b/b_{\rm max} = 0.28$. Each frame represents a time step of 15 fm/c ($\sim 5\times10^{-23}$ s) in the evolution of the collision. After maximum density is reached in the overlap region of the nuclei, participant and spectator matter deflects mostly to negative scattering angles, indicative of negative flow.

As the obtained density ρ increases with increasing beam energy, the repulsive portion of the mean field $U(\rho)$ and the hard scattering due to $\sigma_{\rm nn}$ gradually dominate the reaction dynamics. Figure 4.21 shows BUU calculations for ^{197}Au+^{197}Au at an incident energy of 150 MeV/nucleon. Each frame represents a time step of 20 fm/c ($\sim 6 \times 10^{-23}$ s). After maximum compression, nuclear matter mostly deflects to positive scattering angles, and the signal for positive directed flow is clearly evident.

The procedure for extracting the balance energy for a given system and set of input parameters (K, $\sigma_{\rm nn}$, $b/b_{\rm max}$) is the same as for experimental data, except that for BUU the reaction plane is known *a priori* and exclusion of a flow particle of interest is unnecessary. Nucleons are placed into rapidity bins, and the average transverse momenta projected into the reaction plane, p_x, is plotted as a function of the reduced c.m. rapidity, $(y/y_{\rm proj})_{\rm cm}$. Figure 4.22 shows the results for Au+Au collisions for several energies encompassing the balance energy. The flow at each energy is extracted by fitting the midrapidity range $|(y/y_{\rm proj})_{\rm cm}| < 0.5$ to a least squares fit, and the balance energy is determined by plotting the extracted flow values as a function of incident energy.

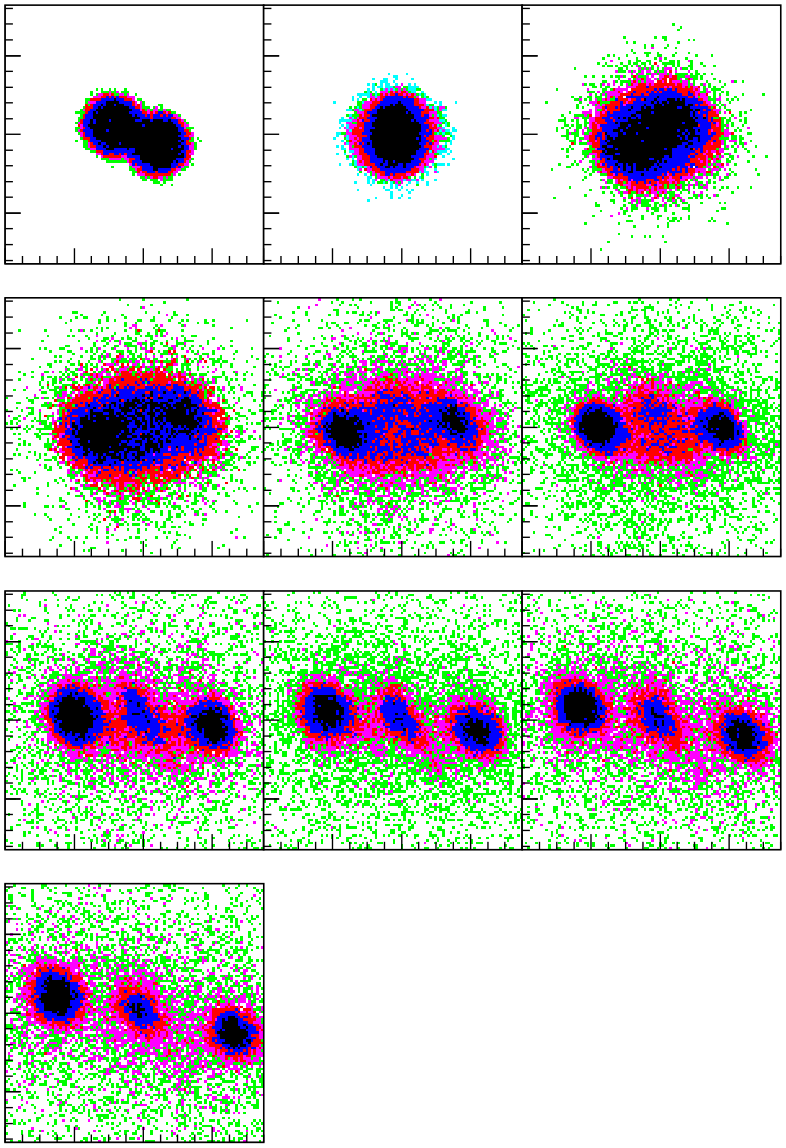

Figure 4.20: BUU calculations in coordinate space projected onto the reaction plane for ^{40}Ar+^{45}Sc at an incident energy of 40 MeV/nucleon and a reduced impact parameter of $b/b_{\max} = 0.28$. Each frame represents a time step of 15 fm/c ($\sim 5 \times 10^{-23}$ s) in the evolution of the collision.

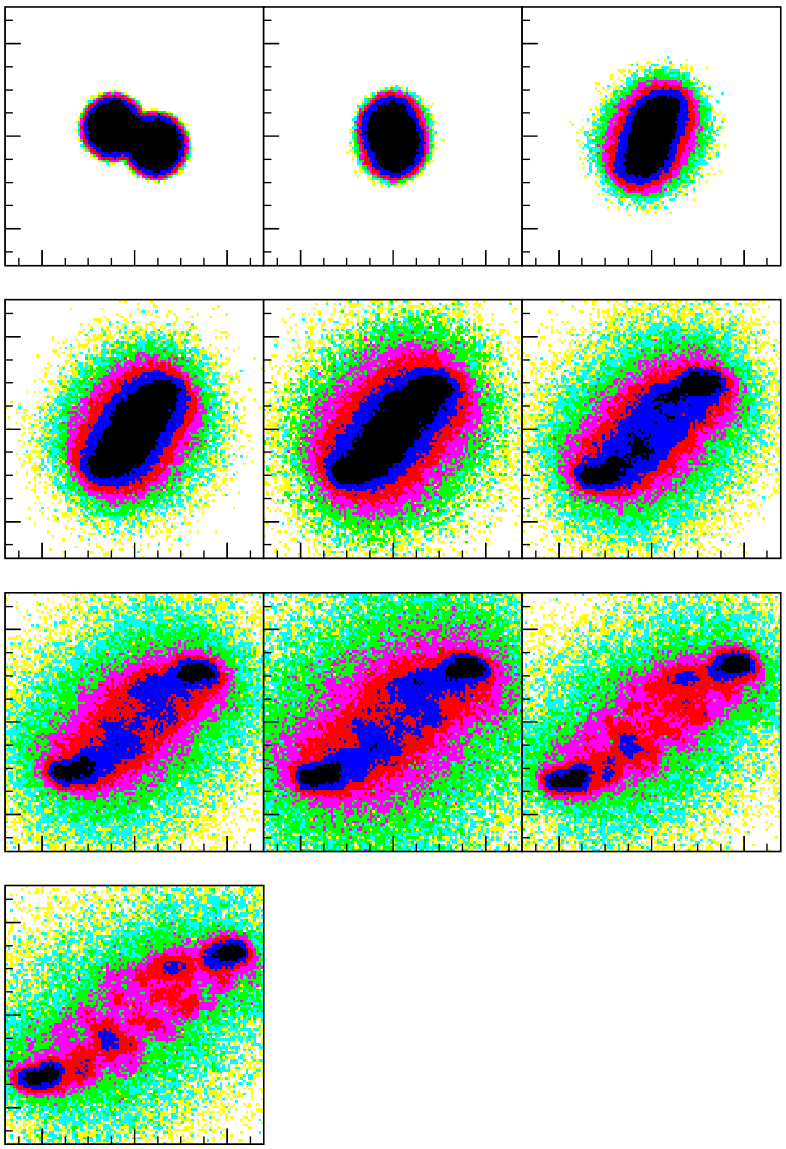

Figure 4.21: BUU calculations in coordinate space projected onto the reaction plane for ^{197}Au+^{197}Au at an incident energy of 150 MeV/nucleon and a reduced impact parameter of $b/b_{\max} = 0.28$. Each frame represents a time step of 20 fm/c ($\sim 5 \times 10^{-23}$ s) in the evolution of the collision.

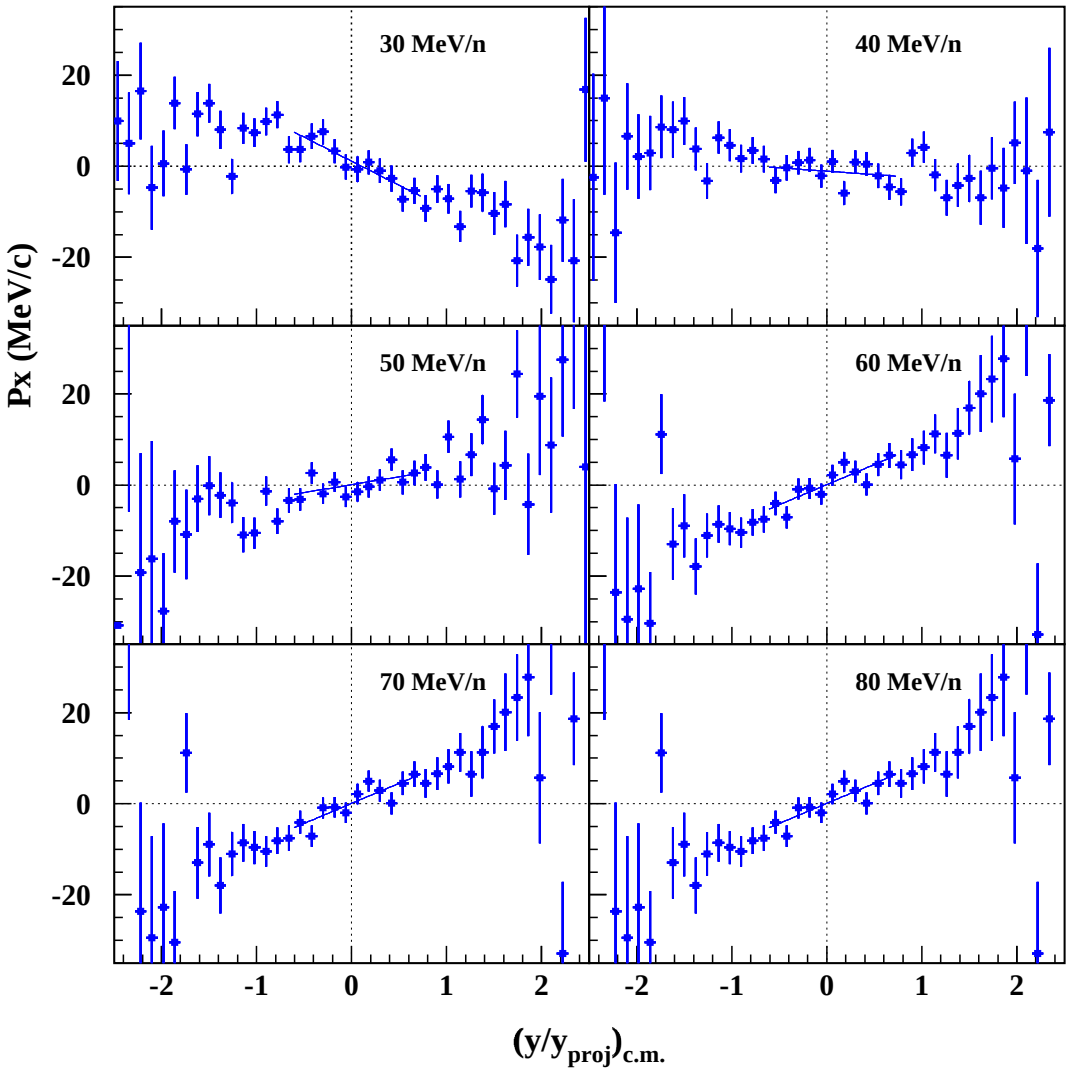

Figure 4.22: BUU calculations of the average transverse momentum *vs.* the reduced rapidity in near-central Au+Au collisions ($b/b_{\max} = 0.28$).

4.5 Effect of Coulomb Interaction on the Balance Energy

As discussed in Sec. 4.2.3, Zhou *et al.* investigated the effect of excluding the Coulomb interaction from VUU calculations of the balance energy for light systems. The general finding was that $E_{\rm bal}$ is higher when Coulomb effects are turned off, which is expected since the Coulomb interaction acts to increase the repulsive dynamics of the collision. However, the VUU calculations were carried out only for systems up to $A = 200$.

Westfall *et al.* [57] postulated that the nuclear mean field can be associated with the surface of the two interacting nuclei and hence should scale as $A^{2/3}$. Also, the repulsive nucleon-nucleon interaction should scale as A, the number of nucleons present. They observed that the competition between these two effects leads to the $A^{-1/3}$ dependence in the experimental data. The role of Coulomb repulsion was not included in their discussion because of the small system masses. Figure 4.23 shows the balance energy plotted as a function of the system mass for an accumulated set of 4π Array data[8], represented by open squares. Data are for near-central events with $\langle b/b_{\rm max}\rangle = 0.28$. A power law fit of the form $E_{\rm bal} \propto A^{-\tau}$ agrees well with the data. However, $\tau_{\rm Data} = 0.44 \pm 0.03$, which is not in agreement with the suggested $A^{-1/3}$ dependence.

To investigate the role of Coulomb forces in the system mass dependence of $E_{\rm bal}$, BUU calculations were performed for systems of various masses, from Ne+Al ($A = 47$) to Au+Au ($A = 394$). For the present calculations, a soft equation of state ($K = 200$ MeV) and a reduced in-medium cross section ($\alpha = -0.2$, see Eq. 4.4) was used. The Coulomb interaction is included or excluded by way of an input flag to the

[8]The ^{12}C+^{12}C point from the original mass dependence paper by Westfall *et al.* [57] is excluded from Fig. 4.23.

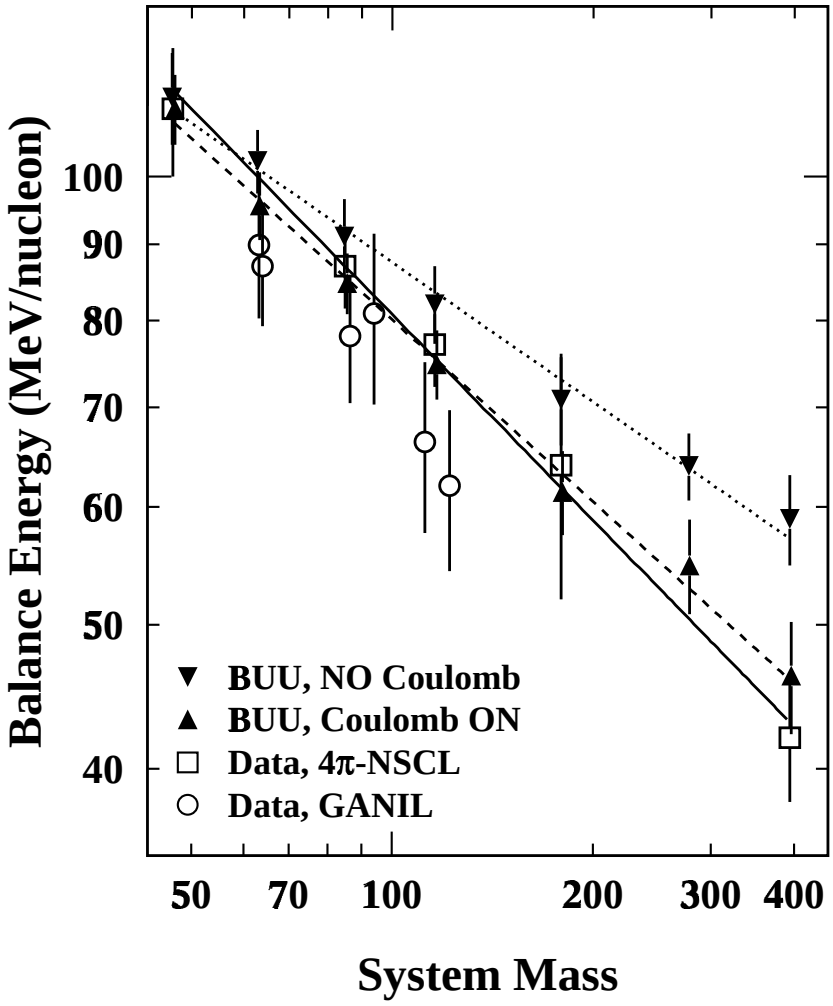

Figure 4.23: Balance energy as a function of combined system mass. Open squares/circles are experimental data, and triangles represent BUU calculations with and without the Coulomb interaction included in the calculation.

BUU program. Figure 4.23 also shows the results of the BUU calculations (solid triangles). With the Coulomb interaction included in the calculation (dashed line), the simulation agrees well with the data ($\tau_{\rm BUU} = 0.41 \pm 0.03$). When the Coulomb interaction is removed (dotted line), $\tau = 0.31 \pm 0.03$, very close to the anticipated value of $\tau = 1/3$ from scaling arguments.

4.6 Au+Au as a Probe of the Nuclear EOS

The disappearance of directed flow was suggested initially as a powerful probe of the EOS [76]. However, numerous model calculations have demonstrated that the balance energy, while sensitive to the nuclear compressibility K, was also sensitive to the in-medium cross section $\sigma_{\rm nn}$ [77, 26, 67]. Zheng *et al.* recently used an isospin-dependent BUU model for the ^{48}Ca+^{48}Ca system to show that the same balance energy is obtained with a stiff EOS and vacuum cross section as with a soft EOS and reduced $\sigma_{\rm nn}$ [79]. In fact, $E_{\rm bal}$ was shown to have a weak dependence on K for light systems [69]. Also, $E_{\rm bal}$ was shown to depend strongly on the impact parameter [58, 68, 69], further hindering study of the EOS. However, all of these studies were carried out for systems with $A \lesssim 200$.

In this section we show for the first time that the compressibility K can be isolated using the balance energy. We reveal that the impact parameter dependence of $E_{\rm bal}$ weakens as the system mass increases and nearly vanishes for a heavy system such as Au+Au. We employ BUU model calculations [78, 18] to show that the dependence of $E_{\rm bal}$ on $\sigma_{\rm nn}$ weakens as well for heavy systems. These findings, together with a strong dependence on the compressibility, allow for the first time extraction of EOS properties with the balance energy, which is particularly beneficial because the balance energy is a relatively model-independent observable [26]. Finally, the extended system mass dependence of $E_{\rm bal}$ can then be used to examine the magnitude of $\sigma_{\rm nn}$.

4.6.1 Independence of $E_{\rm bal}$ from Impact Parameter

Previously, the balance energy was observed to increase linearly as a function of impact parameter b for light systems [58]. This dependence was attributed to the need for a larger incident energy to overcome effects of the mean field as the participant zone gets smaller (with decreasing b). Figure 4.24 shows the balance energy as a function of the reduced impact parameter $b/b_{\rm max}$ for the four systems Ar+Sc, Ni+Ni, Kr+Nb, and Au+Au. Data were recorded at the National Superconducting Cyclotron Laboratory with the 4π Array in a consistent configuration which included a 45-element High Rate Array in the forward direction. Details of the experimental setup can be found in Chapter 2 and in Refs. [58, 59, 80]. Not all impact parameter bins are shown due to detector acceptance effects at low incident energies and for less-central collisions. The lines represent linear fits to the data, included to guide the eye. As the system mass increases $E_{\rm bal}$ exhibits a weaker dependence on $b/b_{\rm max}$, and for Au+Au the dependence nearly vanishes. This could be due to the increasing role of the Coulomb interaction as $b/b_{\rm max}$ increases, counteracting the attractive mean field. Therefore, for near-central collisions b can be regarded as a model-independent parameter when comparing $E_{\rm bal}$ to model calculations for Au+Au.

4.6.2 Independence of $E_{\rm bal}$ From $\sigma_{\rm nn}$

We present results of a comprehensive and systematic study of the balance energy using the BUU model for a wide range of system sizes, $63 < A < 394$. For each system size, several energies near the anticipated balance energy were chosen, and several combinations of (K, α) were selected: K = 200, 235, and 380 MeV and α = 0, -0.1, -0.2, and -0.3. Each set of parameters was calculated using four different random number seeds to build statistics and to minimize any effect from the choice of seed. For all systems, an impact parameter corresponding to $b/b_{\rm max} = 0.28$ was

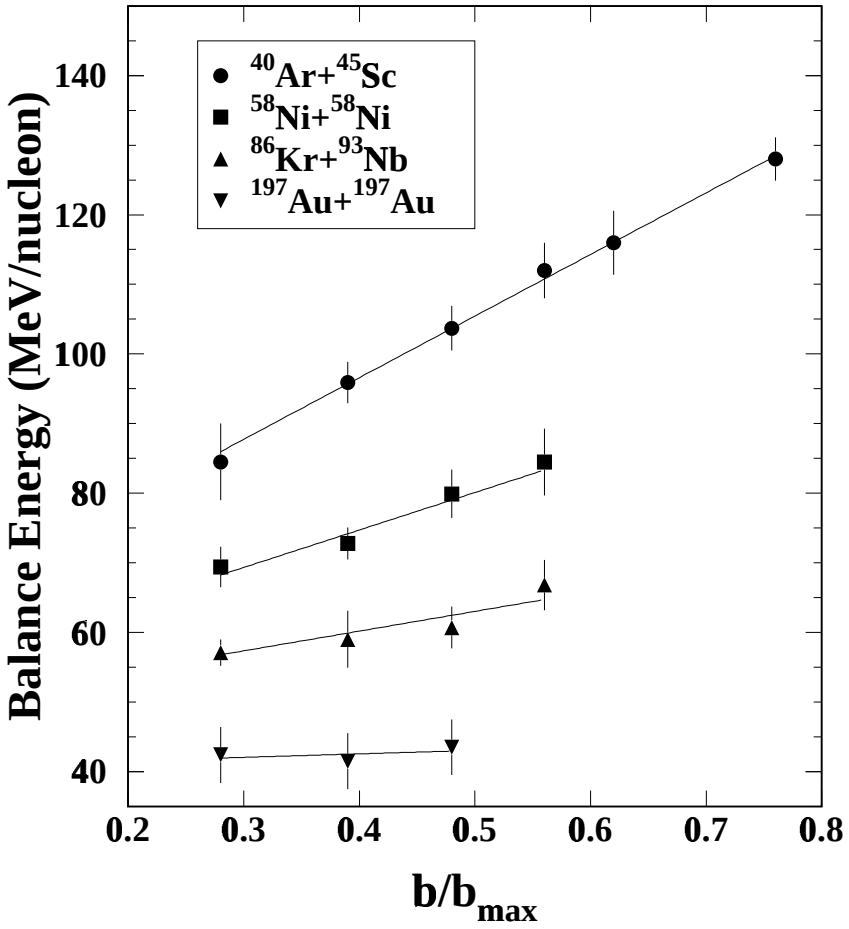

Figure 4.24: Balance energy as a function of the reduced impact parameter for four systems. Data are taken with the 4π Array, the linear fits are intended to guide the eye.

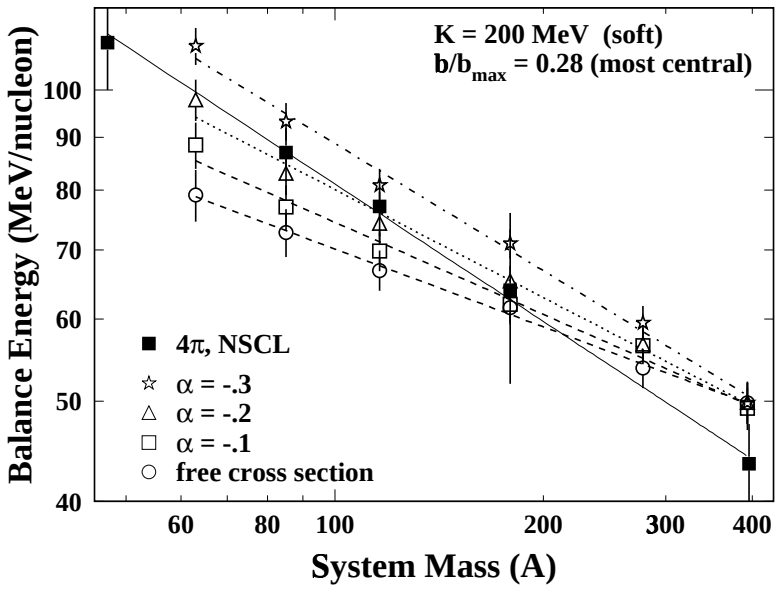

Figure 4.25: BUU model calculations of the mass dependence of $E_{\rm bal}$ for values different reductions of the in-medium cross section σnn. Experimental measurements of $E_{\rm bal}$ are shown as solid squares. The calculated balance energy for Au+Au depends very weakly on the value of α.

used in order to compare to the most central bin of our experimental data (for which the mean $b/b_{\rm max} \approx 0.28$). Note that momentum-dependent mean fields were not included in the present numerical implementation, since $E_{\rm bal}$ is affected very little by momentum dependence at low beam energies and in near-central collisions [60].

Figure 4.25 shows balance energies extracted from BUU calculations as a function of the system mass for four different cross sections, assuming a soft equation of state. Lines represent power law fits to the simulated values, as suggested by the experimental mass dependence of $E_{\rm bal}$ [57, 81]. The error bars are associated with the linear fit of the flow excitation function. The balance energy clearly shows a strong dependence on α for light systems, in agreement with previous theoretical work. However, as the system size increases, the α dependence of $E_{\rm bal}$ nearly vanishes. For $A = 394$

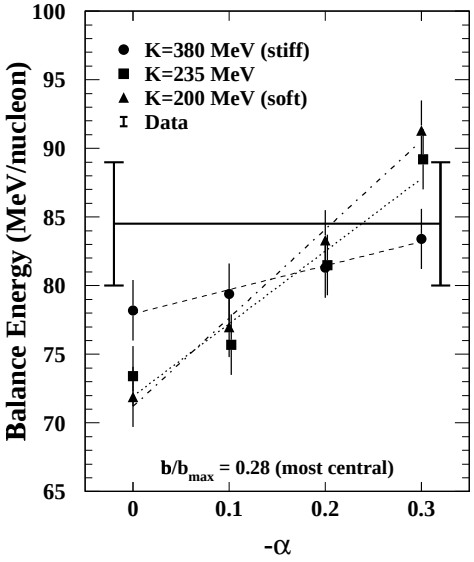

Figure 4.26: BUU balance energies plotted as a function of the σnn reduction parameter $-\alpha$ for three different values of the compressibility K for Ar+Sc. The experimental measurement is represented by a flat line with error bars.

(Au+Au), all of the BUU balance energies are well within error bars.

The gradual loss of the sensitivity of $E_{\rm bal}$ to $\sigma_{\rm nn}$ can be attributed to the change in the collision dynamics at lower beam energies and for larger system masses. As A increases, hard scattering processes play a lesser role in the dynamics of the collision due to Pauli blocking [68]. Therefore, for heavy systems the balance energy is due mostly to combined effects of the attractive mean field and the repulsive Coulomb interaction. Without the Coulomb interaction included in the BUU calculations, $E_{\rm bal}$ for Au+Au is $\sim$10-15 MeV/nucleon larger (see Sec. 4.5).

4.6.3 Isolation of Nuclear Compressibility

Since the balance energy for Au+Au is nearly independent of $\sigma_{\rm nn}$ (over a range of α's) and the impact parameter, BUU predictions can be compared directly to the experimental value of the balance energy to estimate the nuclear compressibility K. This

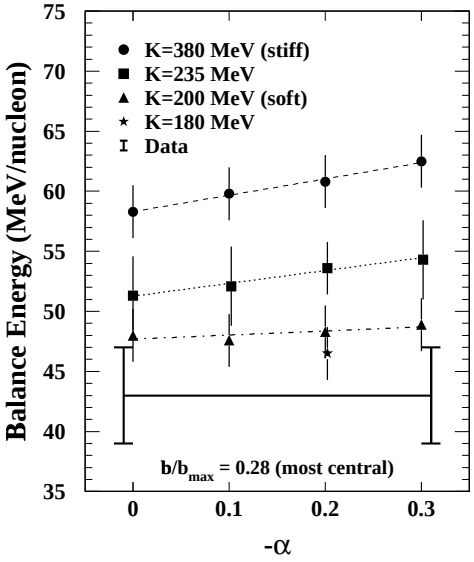

Figure 4.27: BUU balance energies plotted as a function of the σnn reduction parameter $-\alpha$ for three different values of the compressibility K for Au+Au. The experimental measurement is represented by a flat line with error bars.

is in contrast to lighter systems for which K could not be isolated. Figure 4.26 shows BUU balance energies for Ar+Sc ($A = 85$) as a function of the cross section reduction parameter $-\alpha$ for three different values of the nuclear compressibility: K=200, 235, and 380 MeV. Dashed lines are included only to guide the eye. The single experimental value is plotted as a horizontal line with error bars. Depending on the α selected, all three K's can agree within error bars of the experimental value for $E_{\rm bal}$.

In Figure 4.27, BUU balance energies for Au+Au are plotted vs. $-\alpha$, and again the experimental value is represented by a horizontal line. Only $K = 200$ MeV, which corresponds to a *soft* equation of state, falls within error bars of the experimental measurement. The approximate value of K is in good agreement with other measurement techniques; see Table 4.3. Studies of the isoscalar monopole resonance indicate K=200$\pm$20 MeV [82], while recent Thomas-Fermi model calculations pointed to K=234 MeV [8]. Also, Pan and Danielewicz estimated that K lies between 165

Technique	K (MeV)	Date	Author(s)	Reference
Isoscalar Monopole Resonance	200 ± 20	1999	Chung *et al.*	[82]
Giant Monopole Resonance	231 ± 5	1999	Youngblood *et al.*	[83]
Linear Momentum Transfer	210	1996	Haddad *et al.*	[84]
Thomas-Fermi Model	234	1998	Myers and Swiatecki	[8]
Transport Model	165-220	1993	Pan and Danielewicz	[85]

Table 4.3: A comparison of recent values for the compressibility K for a variety of measurement techniques.

and 220 MeV by studying the dependence of sideward flow on multiplicity [85].

4.6.4 Extrapolation of $\sigma_{\rm nn}$

Once a value for K in the BUU parameterization is established, the system mass dependence can be used to investigate the magnitude of $\sigma_{\rm nn}$'s deviation from the vacuum cross section. Figure 4.25 shows the experimental data for the mass dependence of the balance energy (filled boxes). A reduction of $\alpha = -0.2$ in the cross section agrees well with the data for light- and medium-sized systems, while $\alpha = -0.3$ most closely reproduces the slope (power-law exponent) on the experimental mass dependence.

4.7 Summary

In conclusion, we have presented the disappearance of directed transverse flow for Au+Au using the MSU 4π Array. Our results indicate that the balance energy is 42 ± 4 MeV/nucleon. We have also shown that $E_{\rm bal}$ scales as $A^{-\tau}$ for heavy systems as well as light systems. When the Coulomb interaction is removed from the BUU model calculations, $\tau \approx 1/3$, which supports previous scaling arguments about the competing roles of the nuclear mean field and nucleon-nucleon scattering. The measurement of the balance energy for Au+Au presented in this section extends the

system mass dependence of $E_{\rm bal}$ by a factor of two.

We have shown that the impact parameter dependence of the balance energy nearly vanishes for heavy systems such as Au+Au, which we attribute to the increased strength of the Coulomb repulsion counteracting the attractive mean field as $b/b_{\rm max}$ increases. We have also performed a systematically complete set of BUU calculations to show that the sensitivity of $E_{\rm bal}$ to the in-medium cross section weakens as the system size increases and nearly disappears for Au+Au. This effect is ascribed to the lesser role of hard scattering processes at lower beam energies. These two findings allow the EOS parameter K, the nuclear compressibility, to be estimated using the balance energy for the first time. BUU calculations for Au+Au with K=200 MeV, corresponding to a soft EOS, produce balance energies which lie within error bars of the recently measured value. The experimental mass dependence is then employed to estimate the cross section reduction parameter α to be -0.2 to -0.3.

Chapter 5

Disappearance of Elliptic Flow at Intermediate Energies

In the past year, two major elliptic flow developments in very different energy ranges have generated a lot of discussion. In the 1-10 GeV/nucleon range, measured changes in the shape of the elliptic flow excitation function have been used to suggest a softening in the nuclear equation of state. And at intermediate energies, transport model calculations of elliptic flow near the balance energy show a strong dependence on the nuclear equation of state. (See Sec. 1.5 for introductory discussion.)

This chapter is structured similar to the previous chapter, except that the model calculations presented in Sec. 5.4 are published theoretical calculations. The full Fourier analysis of midrapidity emission patterns is carried out for four systems: ^{40}Ar+^{45}Sc, ^{58}Ni+^{58}Ni, ^{86}Kr+^{93}Nb, and ^{197}Au+^{197}Au. The first study of the mass dependence of the *transition energy*, introduced in Sec. 1.5.2, is presented, as well as elliptic flow measurements for Au+Au made over a wide range of energies. Finally, isospin-dependent model calculations are compared to data for our lightest system, Ar+Sc.

5.1 History of Elliptic Flow

The first mention of midrapidity emission perpendicular to the reaction plane occurred in a 1982 theory paper by Stöcker *et al.* [86]. Using a fluid dynamical model to study reactions at $E_{\rm lab}$ = 390 MeV/nucleon, they calculated that angular distributions of protons emitted from near-central collisions show *out-of-plane* jet structures at $\theta_{\rm c.m.} = 90°, \phi = \pm 90°$. They attributed the out-of-plane emission to the fact that compressed matter perpendicular emitted in the reaction plane is hindered or blocked by "spectator" matter.

In the same month that the Stöcker *et al.* paper appeared in *Physical Review C*, a paper by Gyulassy, Frankel, and Stöcker was published in *Physics Letters B* which employed a kinetic energy tensor to analyze flow patterns for the first time [49]. A 3×3 *flow* tensor is constructed from the emitted particles' momentum components, weighted inversely by the mass of the fragments. The eigenvectors of the tensor represent the principal axes of the flow ellipsoid, and its shape and orientation relative to the reaction plane and the beam axis can be used to measure in-plane and out-of-plane emission.

Experimentally observed out-of-plane emission, termed *squeeze-out*, was first observed in 1989 at nearly the same time by two competing collaborations. The Diogène Collaboration at the Saturne synchrotron in Saclay observed slight peaks in the azimuthal distribution of particles at midrapidity in 800 MeV/nucleon Ne-induced reactions [87]. At the Bevalac in Berkeley, the Plastic Ball/Wall group observed out-of-plane emission in Au+Au collisions at 400 MeV/nucleon [88]. They also characterized the emission patterns in terms of the kinetic energy flow ellipsoid, which could account for directed flow as well as out-of-plane flow.

The strength of the Plastic Ball/Wall Collaboration's analysis technique was their use of the transverse momentum method to determine the reaction plane. This al-

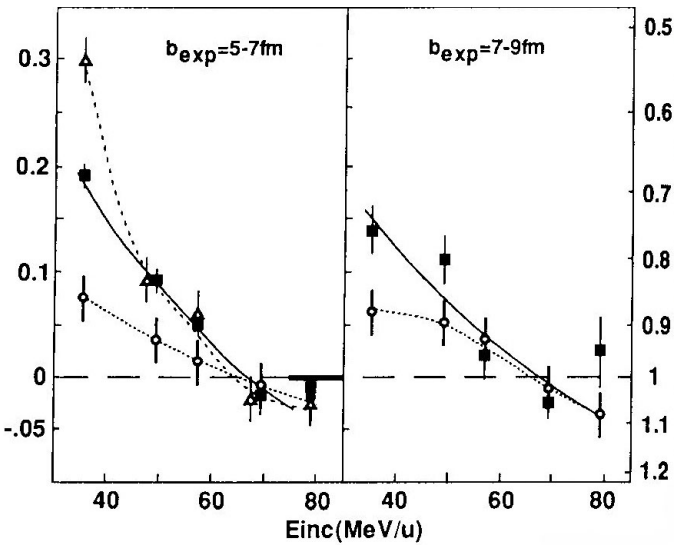

Figure 5.1: First experimental evidence for the transition from in-plane to out-of-plane emission in intermediate-energy collisions. Data are taken with the Nautilus detector at GANIL [92].

lowed the flow ellipsoid to be rotated into the reaction plane initially, followed by a second rotation so that the ellipsoid's primary axis coincided with the beam axis. Without this two-fold rotation, the ϕ-distributions would show irregularities and would not be peaked at $\phi = 90°, 270°$. The same collaboration also characterized squeeze-out as a function of projectile energy and mass, as well as the rapidity dependence by using a novel ratio of out-of-plane/in-plane emission [91].

The transition from in-plane to out-of-plane emission was first observed using ^{64}Zn+^{58}Ni collisions at the GANIL facility by the NAUTILUS collaboration in 1994 [92]. Figure 5.1 shows their data in the form of excitation functions of a_2, a measure of the anisotropy. In-plane emission is indicated by positive a_2, and out-of-plane emission is indicated by negative a_2. The energy of transition increases as the impact parameter increases, similar to the balance energy for light systems (see Sec. 4.6.1). Also, the MINIBALL/ALADIN collaboration observed the onset of out-of-plane emission (the experiment was conducted at GSI) in Au+Au collisions of 100 MeV/nucleon [93], where out-of-plane emission is seen for central collisions while peripheral collisions

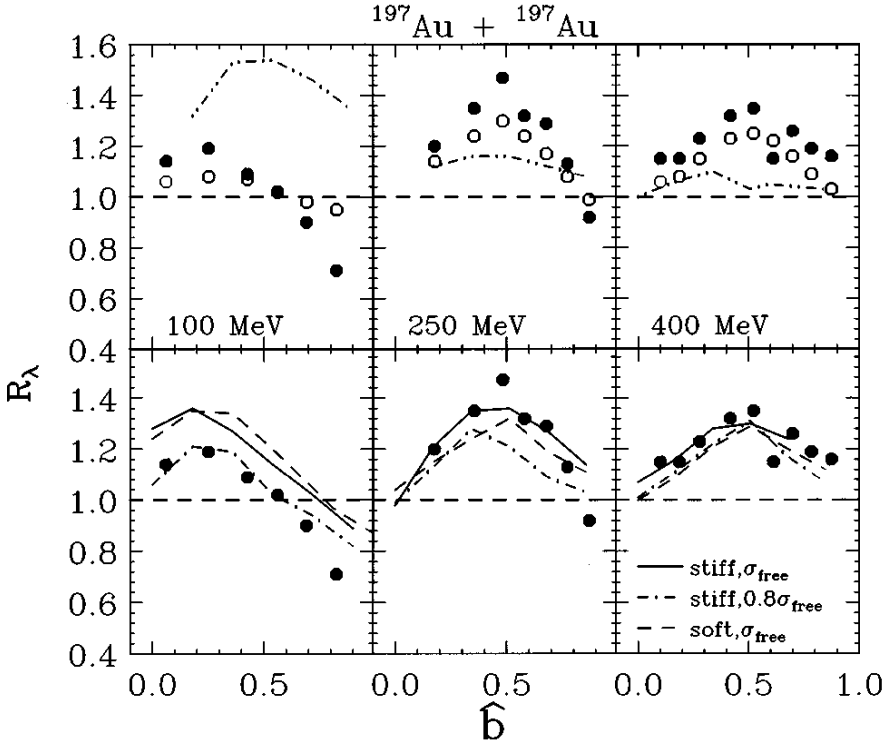

Figure 5.2: Impact parameter dependence of the anisotropy ratio, in which positive R_λ values correspond to predominantly out-of-plane emission. Data are taken with the Miniball/ALADIN detector [93].

clearly show in-plane emission. Their comparison to Boltzmann-Uehling-Uhlenbeck calculations showed that as the beam energy is increased, the value for the reduction in the in-medium nucleon-nucleon cross section appears to change; see Fig. 5.2.

In the past couple years, the field of elliptic flow[1] has expanded to include measurements at Bevalac, SIS, AGS, and recently SPS. The out-of-plane energy regime, extending roughly from 80 MeV/nucleon to 4 GeV/nucleon, is especially interesting because information about the early high-density stage of the collision is preserved in the detected particles. In fact, the ratio of out-of-plane to in-plane emission appears to be very sensitive to some of the parameters of the equation of state in this energy

[1]The term *elliptic* (or *elliptical*) *flow* was introduced in 1997 by Heinz Sorge [89], a theorist at SUNY-Stony Brook who studied the elliptical emission patterns at midrapidity that were measured by the E877 Collaboration at Brookhaven [90].

range, as demonstrated by Hartnack *et al.* [94]. But of greater interest is the recent finding by the E895 Collaboration published in 1999 [27]. Using elliptic flow measurements of protons for Au+Au from 2-8A GeV, a crossover from out-of-plane to in-plane flow is seen. Comparison of the crossover energy to a relativistic Boltzmann equation suggests a softening of the nuclear equation of state from stiff to soft around 4A GeV. Such a softening of the EOS could result from a number of effects, including the possible onset of a nuclear matter phase change, discussed by P. Danielewicz *et al.* [95]. At intermediate energies, Zheng *et al.* at Texas A&M used isospin-dependent BUU calculations to show that the first crossover from in-plane to out-of-plane emission is dependent on the EOS [79]. This will be discussed in the next section.

5.2 Motivation for Present Study

The azimuthal anisotropy of particle emission near 90° in the center-of-mass frame (which signifies elliptic flow) is an attractive quantity for two reasons. First, measuring the azimuthal distribution of protons and fragments at midrapidity is a relatively easy task for the experimentalist. At intermediate energies, the only delicate part of the analysis rests in the reaction plane determination.[2] Second, as stated earlier, fragments emitted out of the reaction plane at midrapidity are uninhibited by projectile- and target-like fragments after the collision. With the addition of Au+Au, data are available for masses extending from A=85 (Ar+Sc) to A=394. The detector setup is nearly identical for the four analyzed data sets. Therefore, a systematic study of the mass dependence of the *transition energy* can be performed without taking additional data.

[2]Another slightly involved calculation at higher energies is the determination of the flow angle; that is, the angle between the major axis of the flow ellipsoid and the beam axis. However, at intermediate energies, the major axis nearly coincides with the beam axis, and rotating into the frame of the flow ellipsoid is unnecessary. See Ref. [97]

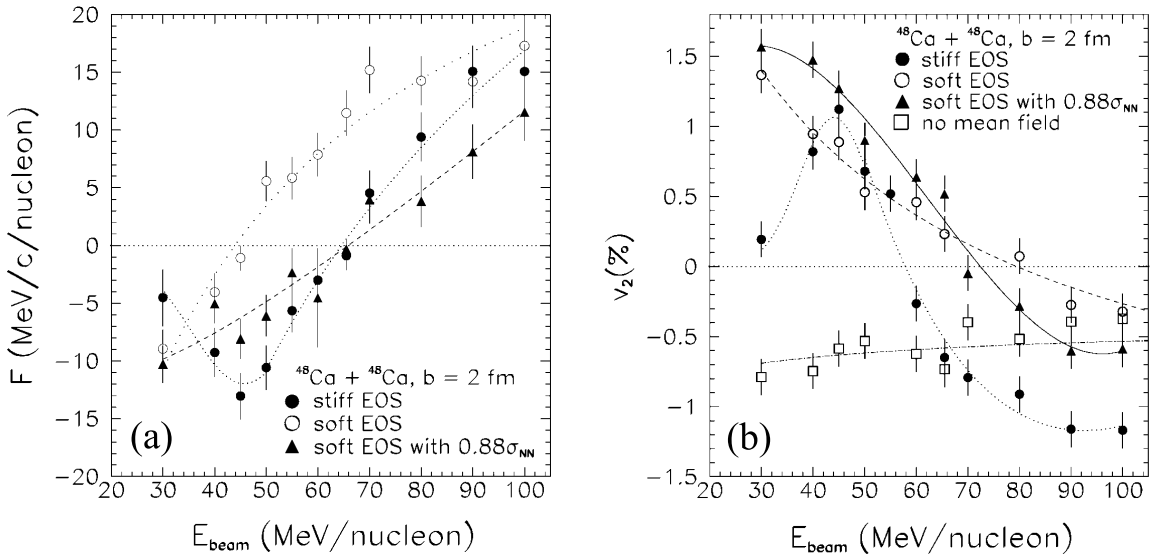

Figure 5.3: Isospin-dependent BUU calculations of the excitation function of (a) the proton directed flow and (b) the proton elliptic flow in ^{48}Ca+^{48}Ca collisions at an impact parameter of 2 fm. Taken from Ref. [79].

5.2.1 Recent Theoretical Findings

Recently, theorists working at Texas A&M studied proton elliptic flow in collisions of ^{48}Ca+^{48}Ca at energies from 30 to 100 MeV/nucleon using an isospin-dependent Boltzmann-Uehling-Uehlenbeck (IBUU) model [79]. Their initial hope was that the elliptic flow transition would not show the dual dependence on the compressibility K and in-medium cross section $\sigma_{\rm nn}$ exhibited by the disappearance of directed flow for light systems (see Sec. 4.6).

Figure 5.3 shows the results of the IBUU calculations.[3] In Figure 5.3(a) the directed flow excitation function is calculated for three different sets of parameters. The same balance energy ($F = 0$) is obtained for a stiff EOS and a soft EOS with a reduced $\sigma_{\rm nn}$. However, as shown in Figure 5.3(b), the proton elliptic flow excitation function for both the soft EOS and stiff EOS changes from positive (in-plane) at low energies to negative (out-of-plane) at high energies, and the energy at which this

[3]Although they chose neutron-rich nuclei, effects due to isospin asymmetry on the proton elliptic flow are not very strong, as discussed in Ref. [96].

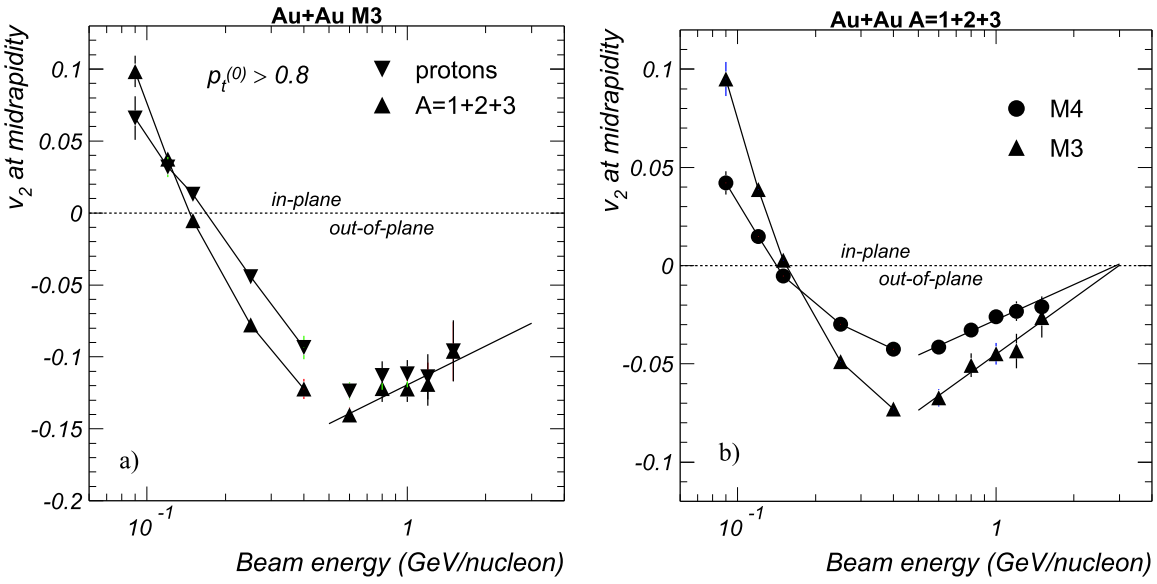

Figure 5.4: Elliptic flow in Au+Au collisions from 90 MeV/nucleon to 1.49 GeV/nucleon as measured by the FOPI Collaboration at GSI-Darmstadt for (a) a high-p_t cut and (b) all p_t included. Taken from Ref. [98]

transition occurs differs for the two EOS. Zheng *et al.* concluded that the transition energy is more sensitive to the EOS than $\sigma_{\rm nn}$ and suggested that the study of both directed and elliptic flow at intermediate energies would allow the extraction of both K and $\sigma_{\rm nn}$. For present consideration, the ^{40}Ar+^{45}Sc system is very close to ^{48}Ca+^{48}Ca in size and proton number. Therefore, comparison of experimental data to the IBUU calculations can be useful for extracting EOS information.

5.2.2 Previous Studies of Elliptic Flow for Au+Au

Similar to the directed flow analysis of Chapter 4, a strong motivation exists for studying elliptic flow for the Au+Au system in particular. To date, Au+Au elliptic flow has been studied in several experiments at SIS at GSI-Darmstadt, Bevalac at Berkeley, and AGS at Brookhaven. In particular, the FOPI Collaboration recently completed an extensive study of Au+Au elliptic flow between 90 MeV/nucleon and 1.5 GeV/nucleon [66, 97, 98]. Figure 5.4 shows the elliptic flow for three different

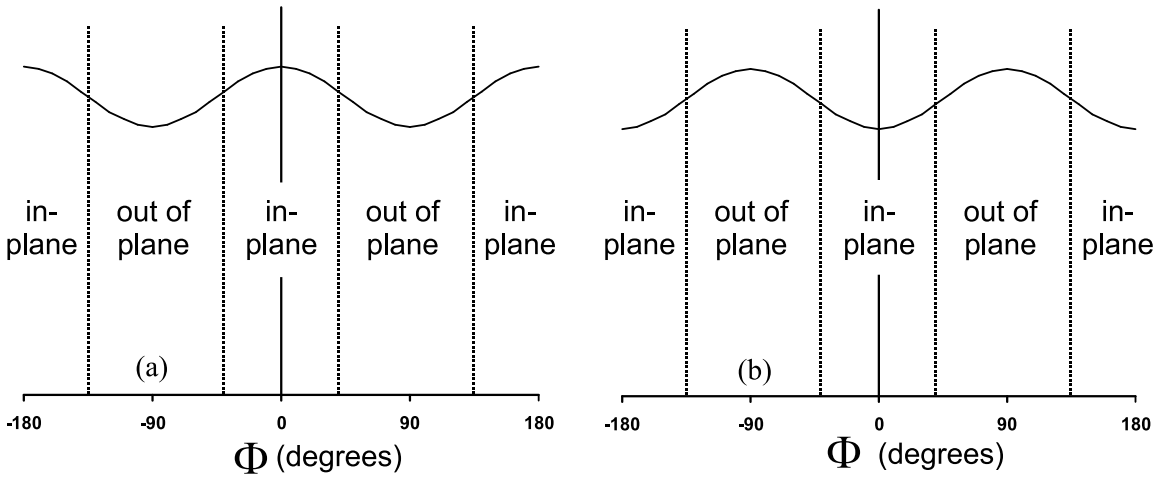

Figure 5.5: Schematic representation of Φ distributions for (a) predominantly in-plane and (b) predominantly out-of-plane emission.

cuts on particle type and transverse momentum p_t. The transition energy $E_{\rm tran}$ occurs near 100 MeV/nucleon for all three cuts, and the data with high-p_t particles exhibits a lower $E_{\rm tran}$ than the inclusive data. Not only does this suggest that $E_{\rm tran}$ is significantly higher than $E_{\rm bal}$, but it also suggests that the transition energy does not occur within the range of energies measured with the 4π Array.

5.3 Experimental Results

As discussed in Sec. 1.5.2, the azimuthal anisotropy of particles emitted near midrapidity exhibits a minimum at an incident energy, $E_{\rm tran}$. At energies below $E_{\rm tran}$, the azimuthal emission pattern at midrapidity is primarily in-plane; that is, the Φ distribution ($\Phi = \phi_i - \phi_{\rm rp}$) is peaked at 0° and 180°. Above the transition energy, the azimuthal emission pattern is primarily out-of-plane, signified by peaks at ±90°. Figure 5.5 is a schematic representation of the Φ distributions for both elliptic flow regions.

5.3.1 Fourier Expansion

The basic technique for studying elliptic flow is owed to Gutbrod *et al.* [91] who recognized that the presence of directed flow hinders the extraction of the squeeze-out (out-of-plane flow) signal. Because elliptic flow is expected to be symmetric about the reaction plane as well as the perpendicular plane, fitting a Φ distribution with a $\cos(2\Phi)$ term could characterize the strength of the elliptic flow. To account for both the $\cos(\Phi)$ nature of directed flow and the $\cos(2\Phi)$ nature of elliptic flow in the azimuthal distributions, a Fourier expansion of the form

$$\frac{dN}{d\Phi} = a_0^{\rm exp}\{1 + a_1^{\rm exp}\cos(\Phi) + a_2^{\rm exp}\cos(2\Phi)\}, \tag{5.1}$$

is used, where $dN/d\Phi$ represents the azimuthal distribution of emitted fragments at midrapidity. In Eq. (5.1), $a_0^{\rm exp}$ is a normalization factor, $a_1^{\rm exp}$ is related to the in-plane directed flow component and $a_2^{\rm exp}$ to the elliptic flow component. The superscript "exp" on the coefficients is to remind that the coefficients extracted from fitting the Φ-distribution are not corrected for reaction plane dispersion. This correction, discussed in Sec. 3.3.3, is made for a_2 by dividing the experimental coefficient by the correction factor:

$$a_2 = \frac{a_2^{\rm exp}}{\langle\cos(\Delta\phi_{\rm rp})\rangle}. \tag{5.2}$$

Therefore,

$$\frac{dN}{d\Phi} = a_0\{1 + a_1\cos(\Phi) + a_2\cos(2\Phi)\}, \tag{5.3}$$

after the dispersion corrections are made. Since the dispersion correction to $a_2^{\rm exp}$ is made after fitting the Fourier expansion to the Φ distribution, the other coefficients can be ignored in the rest of the analysis.

Two different conventions are in practice for quantifying the elliptic flow in terms of the a_2 coefficient. First, the ratio of out-of-plane to in-plane emission, called the

number squeeze-out ratio by Gutbrod *et al.* [91], is defined as the number of particles at midrapidity emitted perpendicular to the reaction plane divided by the number of particles emitted in the reaction plane and is given by

$$R_N = \frac{N(90°) + N(-90°)}{N(0°) + N(180°)}, \tag{5.4}$$

where $N(\Phi)$ represents the summed number of particles in a 90° wedge centered at Φ. Stated more explicitly,

$$R_N = \frac{\int_{45°}^{135°} \frac{dN}{d\Phi} d\Phi + \int_{-135°}^{-45°} \frac{dN}{d\Phi} d\Phi}{\int_{-45°}^{45°} \frac{dN}{d\Phi} d\Phi + \int_{135°}^{225°} \frac{dN}{d\Phi} d\Phi}. \tag{5.5}$$

According to this definition, $R_N < 1$ and $R_N > 1$ are related to a preferential emission of matter in the reaction plane and out of this plane, respectively, while $R_N = 1$ corresponds to a perfect azimuthally isotropic distribution.

R_N can be expressed in terms of the a_2 coefficient from the Fourier expansion by taking into account that $a_1 = 0$ at midrapidity, since directed flow should be zero at $y_{\rm cm} = 0$. Therefore, inserting Eq. (5.3) into Eq. (5.4):

$$R_N = \left. \frac{[1 + a_2 \cos(180°)] + [1 + a_2 \cos(-180°)]}{[1 + a_2 \cos(0°)] + [1 + a_2 \cos(360°)]} \right|_{y_{\rm cm}=0}, \tag{5.6}$$

which reduces to

$$R_N = \frac{1 - a_2}{1 + a_2} \ . \tag{5.7}$$

More recent studies of azimuthal anisotropy and elliptic flow favor the use of the coefficient a_2 itself, with some normalization. Taking the beam direction along the z axis and the reaction plane on the x-z plane as usual, the elliptic flow is determined from the average difference between the square of the x and y components of particle transverse momentum, *i.e.*,

$$v_2 = \left\langle \frac{p_x^2 - p_y^2}{p_x^2 + p_y^2} \right\rangle \ . \tag{5.8}$$

v_2 is a measure of the aspect ratio of the flow ellipsoid, and $v_2 > 0$ ($v_2 < 0$) indicates in-plane (out-of-plane) alignment of the ellipsoid. v_2 can be related to the Fourier coefficient a_2 by recognizing that

$$\left\langle \frac{p_x^2 - p_y^2}{p_x^2 + p_y^2} \right\rangle = \langle \cos(2\Phi) \rangle \tag{5.9}$$

and since $\langle \cos(2\Phi) \rangle$ corresponds to $a_2/2$ in the Fourier expansion of Eq. (5.3),

$$v_2 = \frac{a_2}{2} \, . \tag{5.10}$$

Eqs. (5.7) and (5.10) give the expressions for relating the Fourier coefficient a_2 to other methods for measuring anisotropy. In the present analysis, v_2 is the chosen elliptic flow representation.

5.3.2 The Transition Energy for Au+Au

Now that the technique for characterizing elliptic flow has been presented, the Fourier expansion of Eq. 5.1 can be applied to experimental Φ distributions at midrapidity for any of the available systems and energies. As with the directed flow analysis of Sec. 4.3.2, each detected particle in a collision is treated separately, and a reaction plane is determined from the remaining particles in the collision. This removes any autocorrelation associated with the "particle of interest" (POI) and ensures that an out-of-plane signal is not manufactured by problems in the reaction plane determination.

Also, since the azimuthal distribution is the object of analysis, particles are not weighted in the Φ-distributions. It has been suggested [100] that the Φ distribution should be weighted by the transverse momentum $\mathbf{p}_i^{\perp}$ of the included particles. However, since this is not generally practiced, $\mathbf{p}_i^{\perp}$ weighting is not carried out in the present analysis.

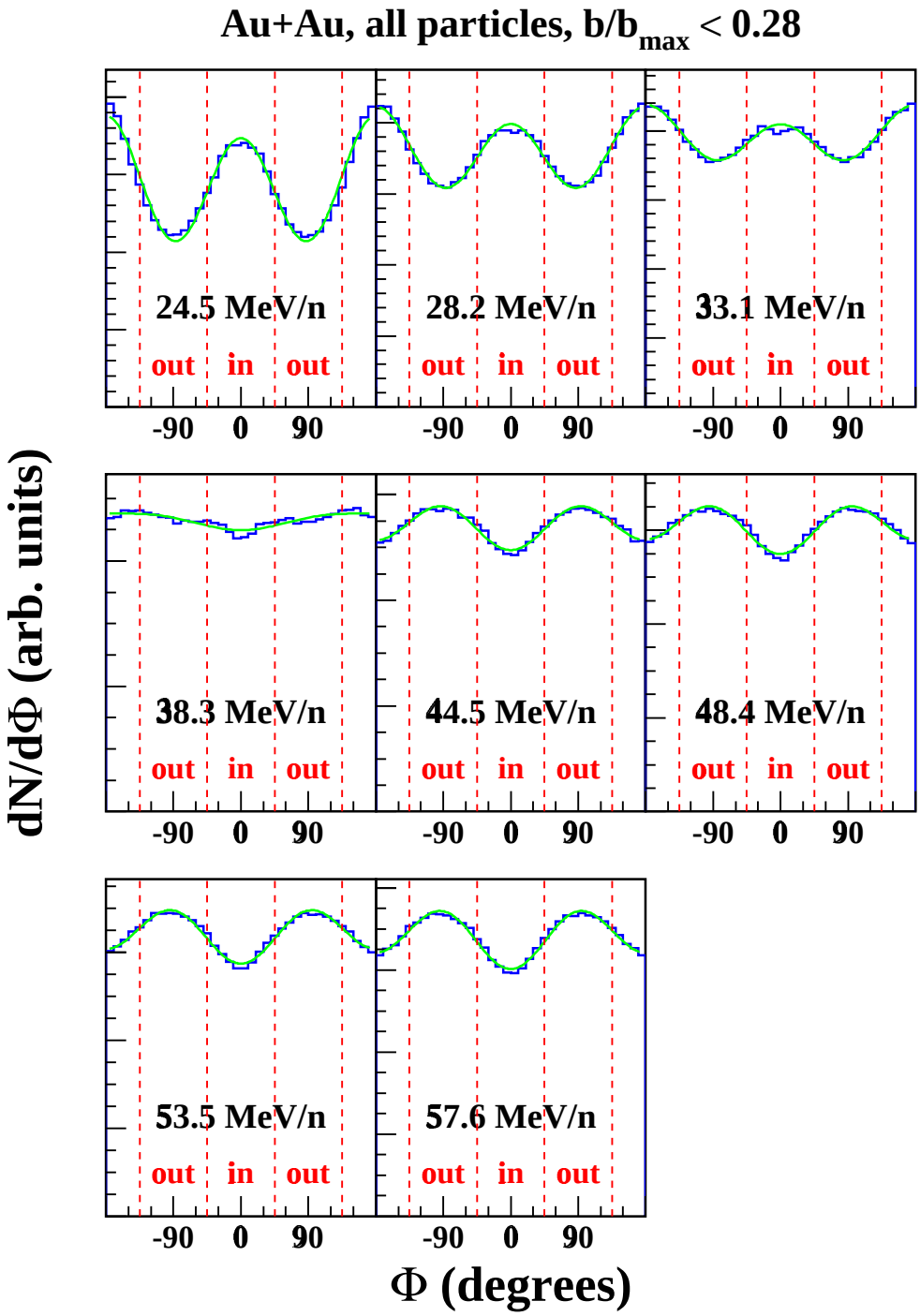

Figure 5.6: Azimuthal distribution of particles in near-central Au+Au collisions emitted near midrapidity ($|(y/y_{\rm proj})_{\rm cm}| \leq 0.5$). Blue lines indicate the experimental spectra, and green curves represent Fourier fits of the form of Eq. 5.1. Dashed red lines are shown to indicate in-plane and out-of-plane regions of particle emission.

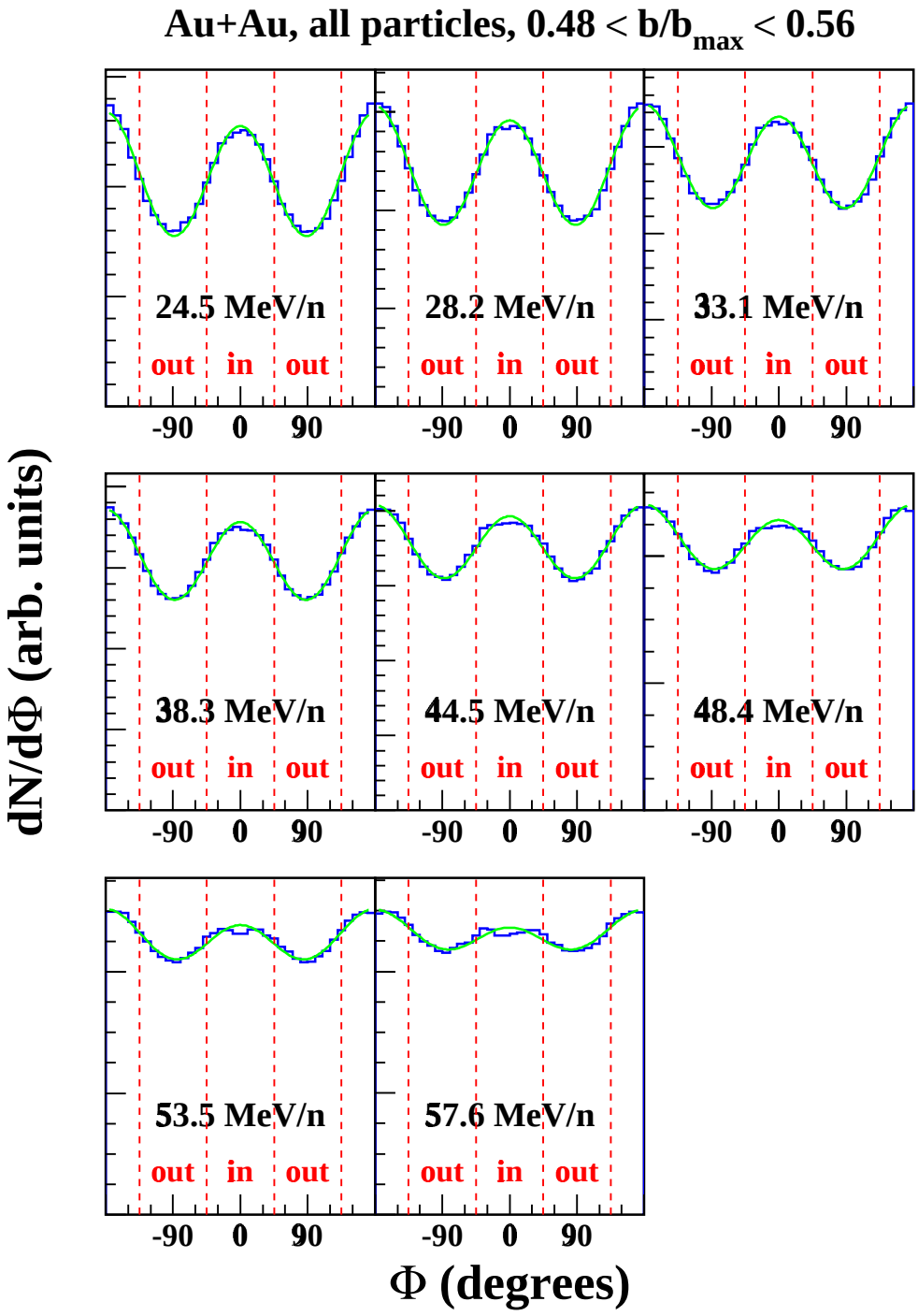

Figure 5.7: Azimuthal distribution of particles in semi-central Au+Au collisions emitted near midrapidity ($|(y/y_{\rm proj})_{\rm cm}| \leq 0.5$). Blue lines indicate the experimental spectra, and green curves represent Fourier fits of the form of Eq. 5.1. Dashed red lines are shown to indicate in-plane and out-of-plane regions of particle emission.

For the present analysis, events were placed into impact parameter bins of equal width, following the geometrical prescription of Sec. 3.1. Figures 5.6 and 5.7 show the midrapidity Φ distributions at all reduced incident beam energies for near-central ($b/b_{\rm max} < 0.28$) and semi-central ($0.48 < b/b_{\rm max} < 0.56$) Au+Au collisions, respectively. In these plots and all subsequent plots, the midrapidity region is defined as

$$-0.5 \leq (y/y_{\rm proj})_{\rm cm} \leq 0.5 \ . \tag{5.11}$$

For elliptic flow experiments in the regime of higher multiplicities and limited acceptance, narrower midrapidity regions usually are selected [71, 27]. The green curves in Figures 5.6 and 5.7 represent fits to the Fourier expansion of Eq. 5.1. At low energies, the Φ-spectra are peaked at 0° and $\pm 180^\circ$, indicating primarily in-plane elliptic flow. As the beam energy is increased, the Φ-spectra become flatter. For the near-central impact parameter bin, the Φ-spectra exhibit peaks at $\pm 90^\circ$ for incident energies above 44.5 MeV/nucleon, indicative of primarily out-of-plane elliptic flow. For the semi-central bin, the elliptic flow is primarily in-plane over the entire range of beam energies studied.

Before presenting the v_2 excitation functions, it is fruitful to discuss some general traits of the Φ distributions. These distributions show both a four-fold symmetry from the shape of the ellipsoids and a two-fold symmetry attributed to two effects. First, since the POI is excluded from the reaction plane determination, it is less likely that the reaction plane will be in the direction of the POI. This leads to a slight suppression of Φ near 0° when compared to Φ near 180° as well as a small depression of Φ at $\Phi = 0^\circ$. Second, peaks and valleys in the out-of-plane region are not centered exactly at $\pm 90^\circ$. This two-fold asymmetry is due to the fact that the Φ distributions are about the *beam* axis, not the flow axis. Near the transition energy, the flow axis nearly coincides with the beam axis, so that a coordinate transformation is not necessary. In addition, true flow angles are difficult to determine accurately in this

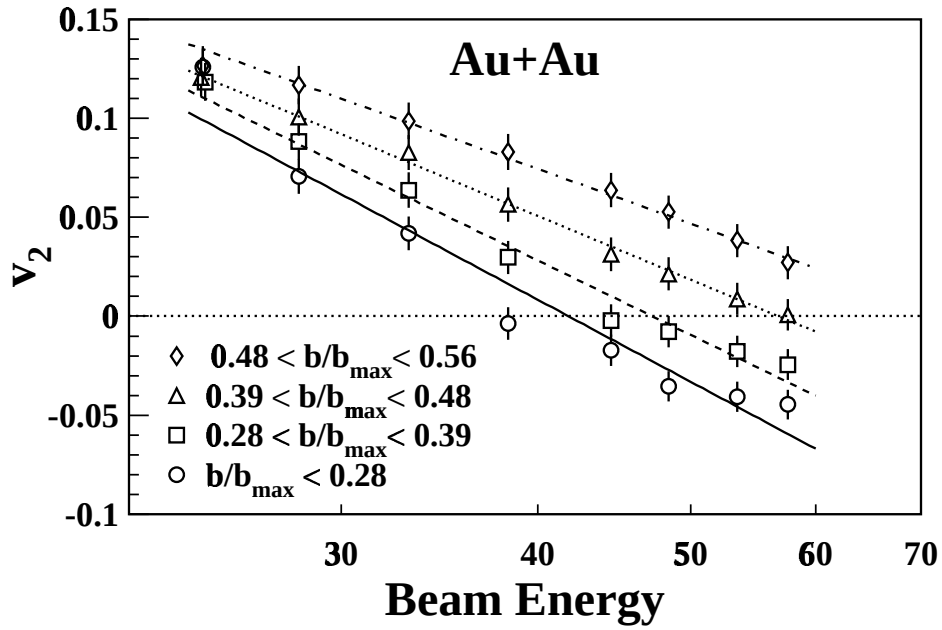

Figure 5.8: Elliptic flow plotted as a function of incident beam energy for Au+Au collisions. Data are for four different impact parameter bins, and solid and dashed lines correspond to logarithmic fits to the data.

energy range because of a finite number of detected particles.

The second order coefficients a_2 can be extracted from the Fourier fits for each beam energy and impact parameter bin. Figure 5.8 shows the v_2 coefficients obtained from Eq. 5.10 for Au+Au collisions. Data for four different impact parameter bins are shown. The error bars are obtained by assigning statistical errors to each bin in the Φ distribution and extracting the error from the convergence minimization routine HFITV, which is standard routine in the CERN library. The fits in Figure 5.8 are logarithmic, as suggested by the trend of the data. All impact parameter bins show an energy dependence of v_2, and as the impact parameter is increased, the transition energy also increases.

The monotonic relationship between b and $E_{\rm tran}$ for Au+Au over the range of impact parameters here can be attributed to the energy deposited into the overlap (participant) zone of the collision. When going from peripheral to central collisions,

b Bin	E_{tran}
$b/b_{\mathrm{max}} < 0.28$	41 ± 3 MeV/nucleon
$0.28 < b/b_{\mathrm{max}} < 0.39$	46 ± 4 MeV/nucleon
$0.39 < b/b_{\mathrm{max}} < 0.48$	56 ± 3 MeV/nucleon
$0.48 < b/b_{\mathrm{max}} < 0.56$	75 ± 6 MeV/nucleon

Table 5.1: Au+Au transition energies extracted from logarithmic fits to the data in Figure 5.8.

the deposited energy becomes larger and the expansion takes place faster, leading to the development of an out-of-plane elliptic flow signal at a lower incident energy. In less central collisions, the excited participant zone needs a higher incident beam energy to generate expansion/emission patterns quickly enough to be hindered by projectile-like or target-like nuclear matter; otherwise, the participant zone will emit fragments unhindered because the spectator pieces will have left the collision zone beforehand. The impact parameter dependence of E_{tran} is in stark contrast to the lack of an impact parameter dependence of E_{bal} for Au+Au (see Sec. 4.6.1). This strengthens the notion of two separate collective mechanisms at work in non-central nuclear collisions.

Table 5.1 lists the values of E_{tran} obtained from the logarithmic fits in Figure 5.8. The error bars are associated with the variance in E_{tran} when data points are excluded systematically from the fit. The data is in strong disagreement with measurements of E_{tran} made by the FOPI group, as evidenced in Figure 5.4. For example, the "M4" impact parameter bin in Figure 5.4(b), which corresponds roughly to $0.39 < b/b_{\mathrm{max}} < 0.56$, has a value for E_{tran} that is greater than 100 MeV/nucleon, a 30-40 MeV/nucleon disparity from the present measurement.

5.3.3 Mass Dependence of the Transition Energy

Using the same analysis technique applied to the Au+Au system, the elliptic flow over a range of beam energies was studied in three additional systems: ^{40}Ar+^{45}Sc, ^{58}Ni+^{58}Ni and ^{86}Kr+^{93}Nb. The subsystem configuration selected in the data analysis for these three systems is the same for Au+Au, presented in Chapter 2.[4] Figures 5.9, 5.10, and 5.11 show representative Φ distributions of particles emitted near midrapidity ($|(y/y_{\rm proj})_{\rm cm}| \leq 0.5$) for the three systems mentioned above. Data are for semi-central collisions with $0.28 < b/b_{\rm max} < 0.39$, and dashed lines represent Fourier fits of the form of Eq. 5.1. At low incident energies for all three systems, emission is primarily in-plane, signified by peaks (valleys) at $\Phi = 0°, 180°$ ($\pm 90°$). As the beam energy is increased, a transition to primarily out-of plane emission, characterized by peaks (valleys) at $\pm 90°$ ($\Phi = 0°, 180°$), is observed.

The extracted v_2 values for each system are plotted *vs.* incident beam energy in Figures 5.12 and 5.13 for near-central and semi-central impact parameter bins, respectively. The curves are included only to guide the eye. The transition energy decreases as the system mass increases for both impact parameter bins. Complementary theoretical studies of the mass dependence of $E_{\rm tran}$ are needed to understand the effect. Interestingly, the mass dependence of $E_{\rm tran}$ follows a trend similar to the mass dependence of $E_{\rm bal}$.

5.4 Comparison to Theoretical Work

Recent calculations based on an isospin-dependent Boltzmann-Uehling-Uhlenbeck (IBUU) model indicated that the crossover from in-plane to out-of-plane elliptic flow is sensitive to the nuclear equation of state. Calculations for ^{48}Ca+^{48}Ca at incident

[4]The ^{86}Kr+^{93}Nb physics files used in the present analysis contained identified particles from a fourth subsystem known as the Zero Degree Detector [34]. However, these particles were ignored in all aspects of the analysis, including impact parameter binning and reaction plane determination.

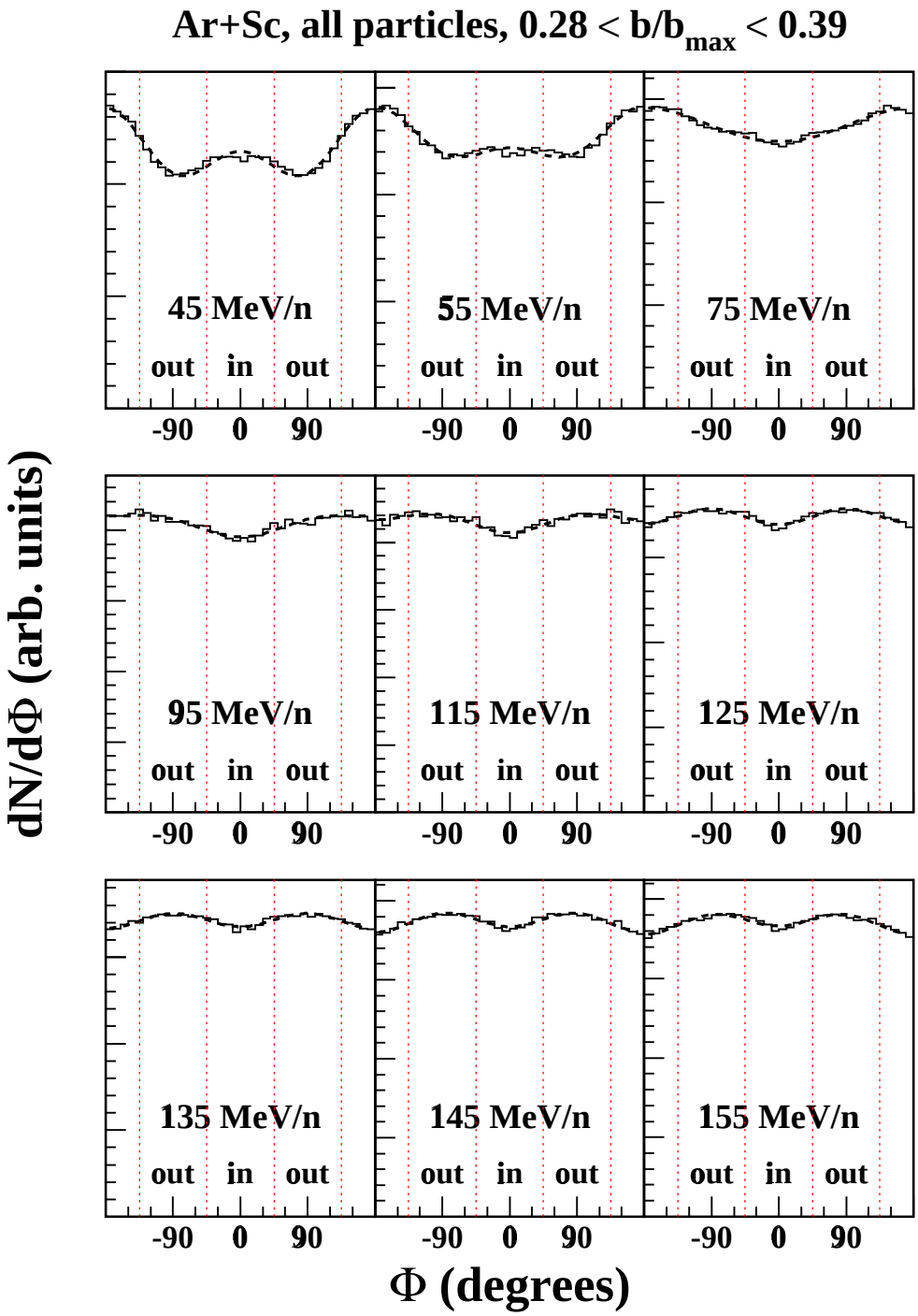

Figure 5.9: Azimuthal distribution of particles in semi-central ^{40}Ar+^{45}Sc collisions near midrapidity ($|(y/y_{\rm proj})_{\rm cm}| \leq 0.5$). Dashed curves represent Fourier fits of the form of Eq. 5.1.

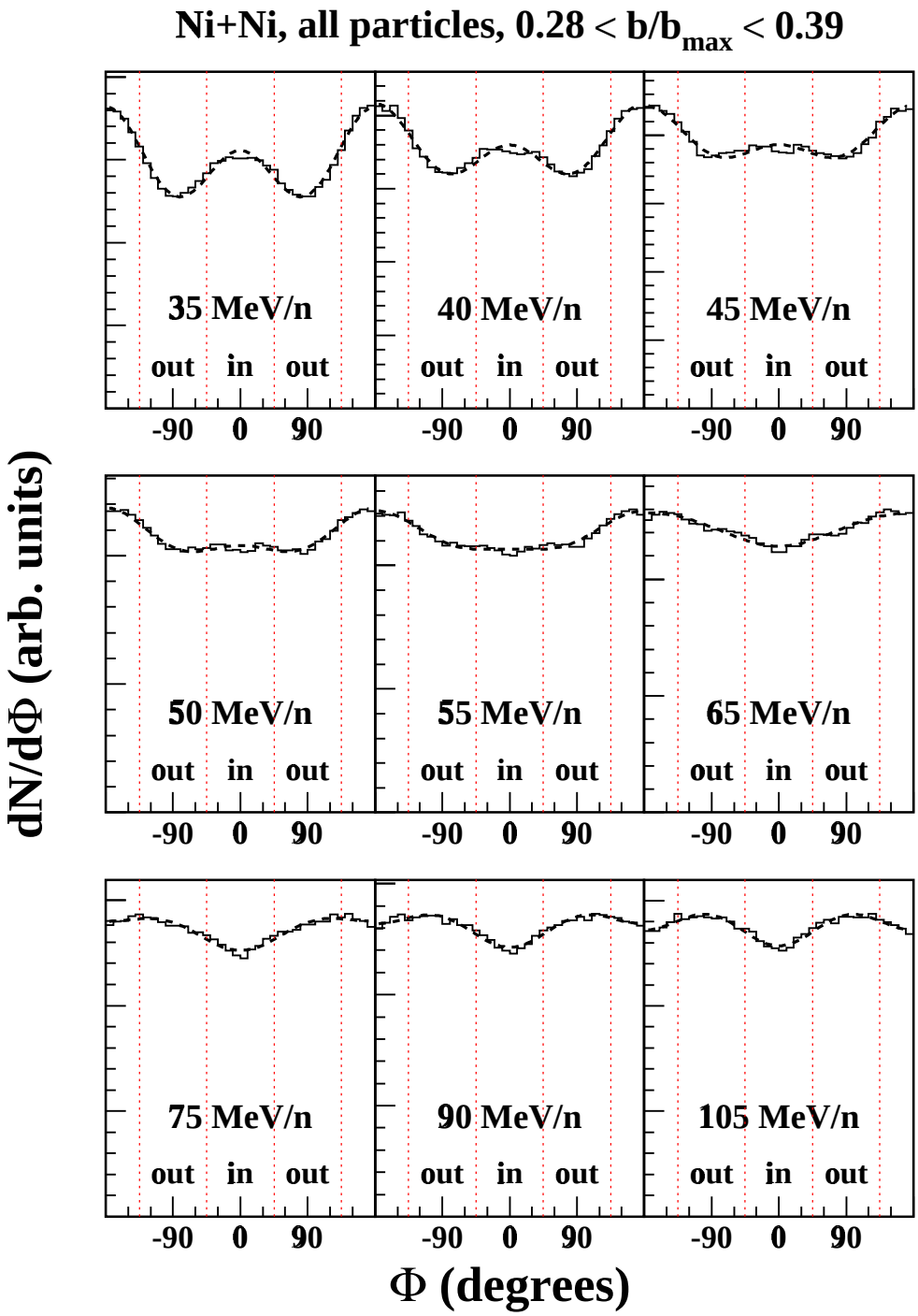

Figure 5.10: Azimuthal distribution of particles in semi-central ^{58}Ni+^{58}Ni collisions near midrapidity ($|(y/y_{\rm proj})_{\rm cm}| \leq 0.5$). Dashed curves represent Fourier fits of the form of Eq. 5.1.

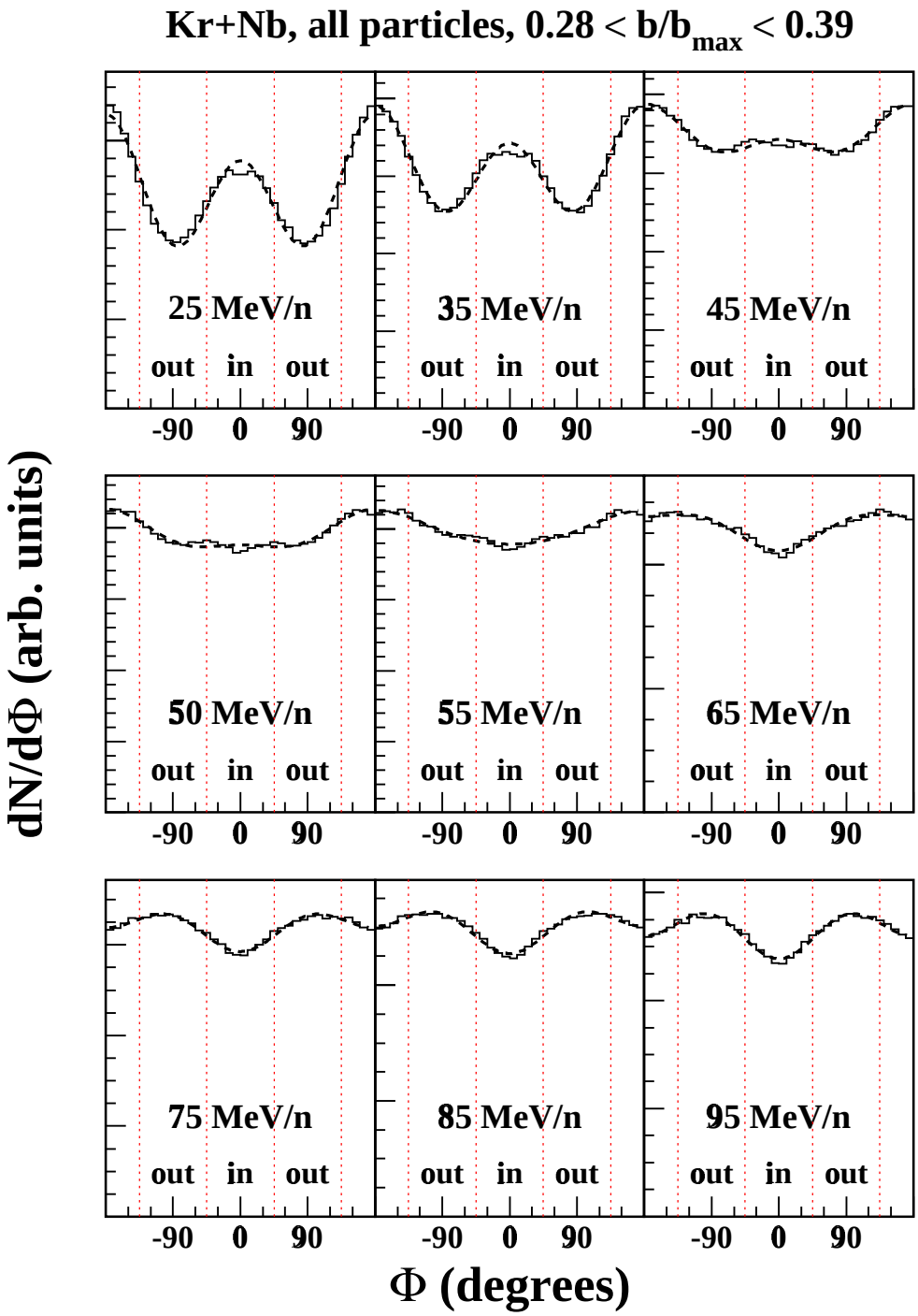

Figure 5.11: Azimuthal distribution of particles in semi-central ^{86}Kr+^{93}Nb collisions near midrapidity ($|(y/y_{\rm proj})_{\rm cm}| \leq 0.5$). Dashed curves represent Fourier fits of the form of Eq. 5.1.

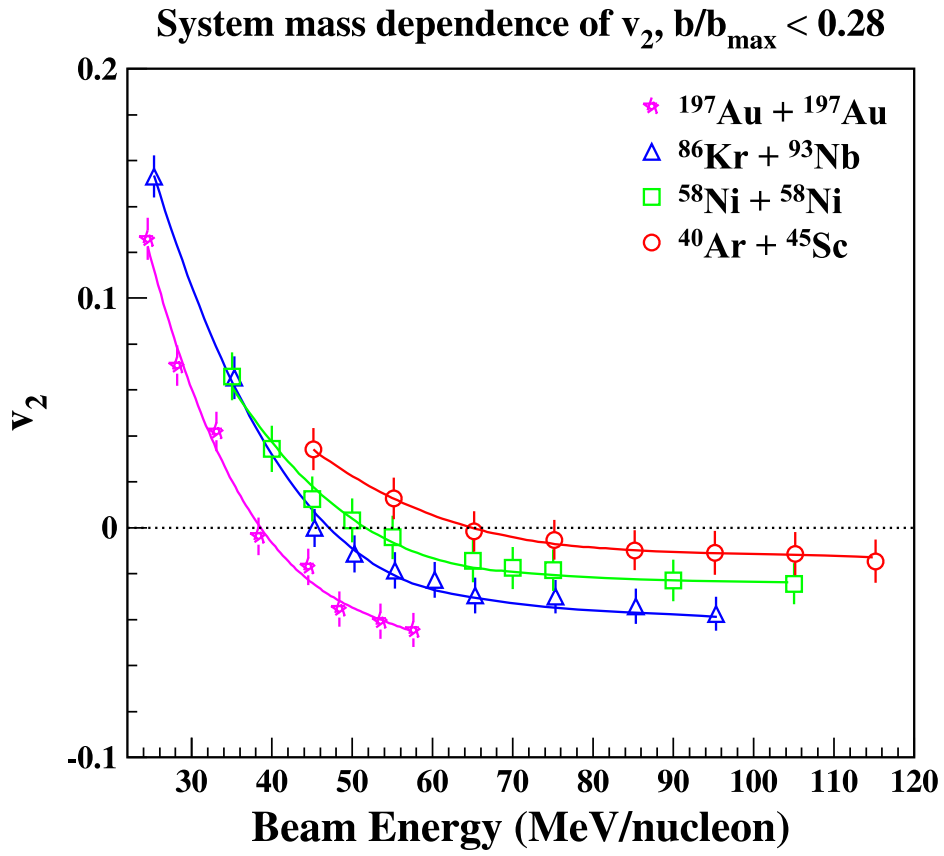

Figure 5.12: Elliptic flow for four systems as a function of incident beam energy in near-central collisions ($b/b_{\mathrm{max}} < 0.28$).

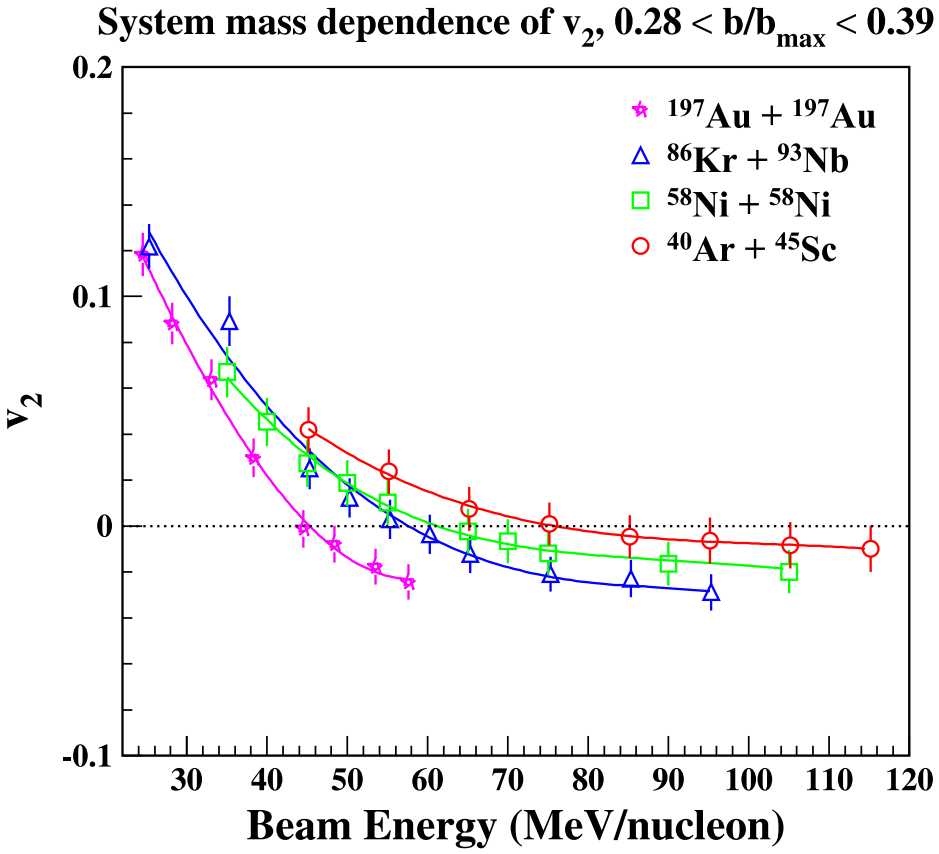

Figure 5.13: Elliptic flow for four systems as a function of incident beam energy in semi-central collisions ($0.28 < b/b_{\rm max} < 0.39$).

energies between 30 and 100 MeV/nucleon showed the transition energy to be lower for stiffer EOS (*i.e.,* higher nuclear compressibility K) than for a soft EOS, even if the in-medium cross section is reduced [79]. This is in stark contrast to the balance energy, which shows almost no sensitivity to the EOS for medium-sized systems with reduced cross-section [18, 69] and the opposite relationship between EOS stiffness and $E_{\rm bal}$ for vacuum cross section (see Sec. 4.6.3). Therefore, the transition energy may be more useful than the balance energy for resolving the nuclear EOS stiffness using medium-sized systems.

Figure 5.14 shows the elliptic flow for ^{40}Ar+^{45}Sc data taken with the 4π Array plotted with the IBUU calculations for ^{48}Ca+^{48}Ca, since these systems are very close in mass. The ^{40}Ar+^{45}Sc data is for the most central impact parameter bin (shown in Figure 5.12) so that the impact parameter of the calculations closely matches the mean impact parameter of the data. For the data, $\langle b/b_{\rm max}\rangle \approx 0.20$, and for the calculations, $b/b_{\rm max} = 0.23$. The curves for both the data and calculations are included to guide the eye. The transition energy for the ^{40}Ar+^{45}Sc data appears to agree most closely with the soft EOS and reduced $\sigma_{\rm nn}$. This finding is in good agreement with the directed flow studies of Sec. 4.6. It should be noted that the magnitudes of the v_2 values in Fig. 5.14 are questionable, since the IBUU calculations from Ref. [79] were performed in an independent-particle formulation with no fragment clustering. However, the energy of crossover is the observable of interest, and differences in the magnitudes are unimportant. Also, the isospin of the system may be important. More calculations are needed.

5.5 Summary

In this chapter we have presented the disappearance of elliptic flow at intermediate energies for several systems. The transition energy for Au+Au shows a strong impact

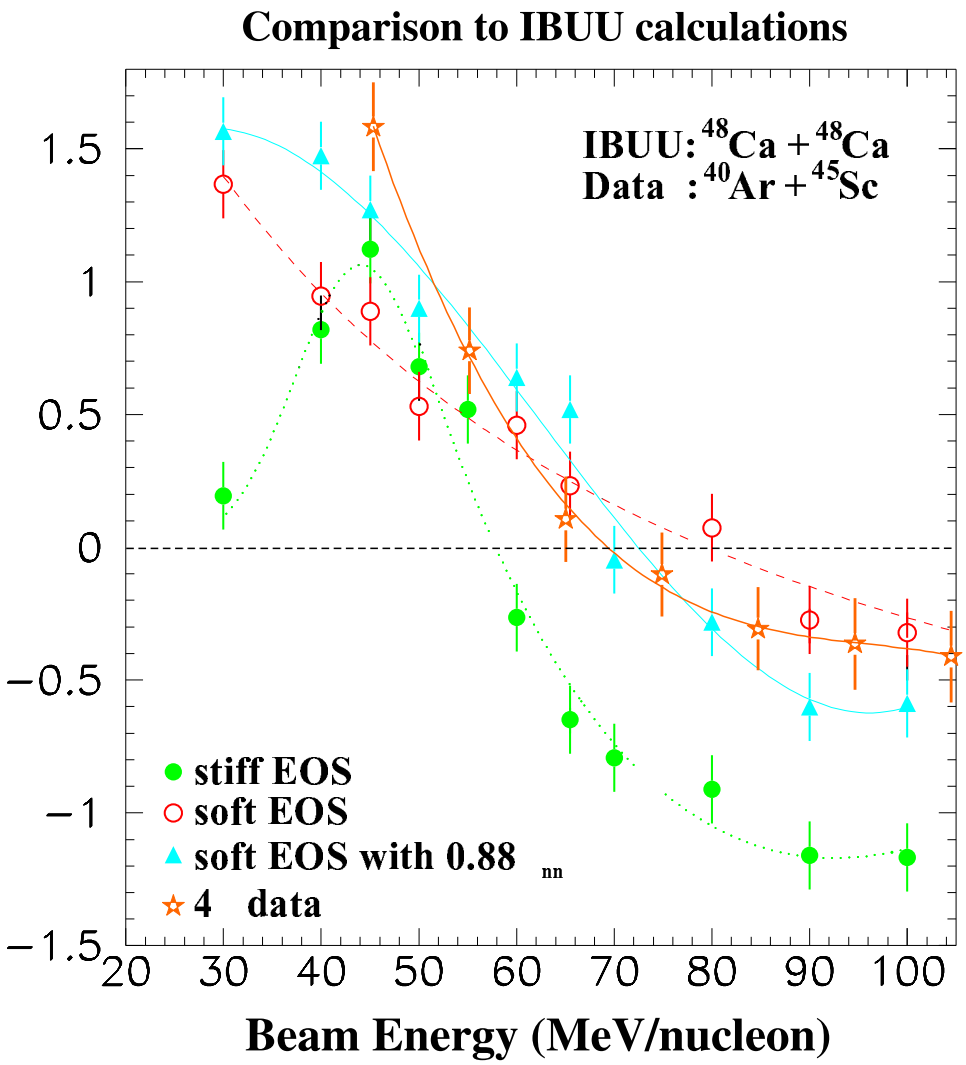

Figure 5.14: Comparison of isospin-dependent Boltzmann-Uehling-Uhlenbeck (IBUU) calculations of ^{48}Ca+^{48}Ca from Ref. [79] with ^{40}Ar+^{45}Sc experimental data taken with the 4π Array.

parameter dependence, which is in contrast to the balance energy results of Chapter 4. The values obtained for the Au+Au transition energy are also quite different from previously published values by the FOPI Collaboration at GSI.

Also, the mass dependence of the transition energy was shown. Similar to the balance energy, the transition energy increases as the system size decreases. Previous theoretical calculations of ^{48}Ca+^{48}Ca by the Texas A&M group showed a strong dependence of $E_{\rm tran}$ on the nuclear EOS, and ^{40}Ar+^{45}Sc experimental data agrees most closely to the soft EOS with a reduced in-medium cross section. This is in good agreement with the findings of Chapter 4. Thus, an additional observable for probing the nuclear EOS using nuclear collisions is established, and future theoretical studies may constrain the nuclear EOS further by exploring the mass- and impact-parameter dependence of the transition energy.

Chapter 6

Conclusion

In this thesis, we have studied two transitions in collective flow observables: the disappearance of directed flow at intermediate energies, or *balance energy*; and the first disappearance of elliptic flow $E_{\rm tran}$, also at intermediate energies, called the *transition energy*. The study of transitions, or zeroes, in flow excitation functions is especially useful because the energy of transition is not influenced strongly by experimental biases such as detector acceptance and detector granularity. Also, these transitions can be modeled by theory without incorporating the complexities of fragment formation and experimental reaction plane dispersion.

The balance energy for Au+Au is interesting because it extends the mass dependence of the balance energy by a factor of 2 in system mass. Previous experimental studies at higher energies were only able to extrapolate $E_{\rm bal}$ for Au+Au, and the extrapolated value depends on the reaction plane dispersion which alters the finite flow values at each measured energy. Also, QMD calculations suggested that the balance energy for Au+Au might be obscured by the large Coulomb interaction for the heavy system. In this thesis we presented the balance energy for Au+Au and showed that the Coulomb interaction acts to decrease the balance energy. In fact, removing the Coulomb term from Boltzmann-Uehling-Uhlenbeck (BUU) model calculations

restores the expected $\tau \approx 1/3$ exponent in the $E_{\rm bal} \propto A^{-\tau}$ power-law relationship. The value of $\tau \approx 1/3$ is predicted by a simple scaling argument in which the balance energy arises from surface effects which scale as $A^{2/3}$, and volume effects which scale with A.

Also, previous theoretical studies of the balance energy showed a dual dependence on the nuclear compressibility K and the in-medium cross section $\sigma_{\rm nn}$ for light- and medium-sized systems. The impact parameter dependence of $E_{\rm bal}$ also has been observed experimentally for light systems. However, BUU calculations in this thesis of the balance energy for Au+Au is nearly independent of $\sigma_{\rm nn}$, and the impact parameter dependence nearly vanishes for Au+Au as well. Therefore, for the first time the balance energy is used to constrain the nuclear equation of state, and comparison between the experimental $E_{\rm bal}$ for Au+Au and BUU calculations show agreement with a *soft* equation of state. The extended mass dependence then is used to show a reduction of 20-30% in the in-medium nucleon cross section.

The elliptic flow transition energy for Au+Au was presented, and the values obtained with the 4π Array show substantial disagreement with previous measurements by the FOPI group at GSI. The transition energy for Au+Au shows a strong impact parameter dependence, in contrast to the balance energy.

The mass dependence of $E_{\rm tran}$ was studied using four systems with a nearly identical configuration of the 4π Array. As the system size increases, the transition energy decreases, similar to the balance energy. Comparison between experimental ^{40}Ar+^{45}Sc data and ^{48}Ca+^{48}Ca isospin-dependent BUU calculations show good agreement with a *soft* EOS, in accordance with the directed flow results.

Therefore, two different phenomena have been shown for the first time to be useful for constraining the nuclear EOS. Both the balance energy for Au+Au and the transition energy for Ar+Sc agree with model calculations in the BUU framework

that incorporate a **soft** equation of state and a reduced in-medium nucleon cross section. Further theoretical and experimental studies are warranted, as a primary goal of nuclear physics is to determine these two entities. It is ultimately hoped that nuclear collisions may be useful for constraining the value of the nuclear compressibility and resolving some of the difference in values obtained from monopole and dipole resonance studies.

Appendix A

4π Array Parameters

This Appendix contains many of the specifications for the 4π Array at the time of this this thesis experiment. Please refer to Chapter 2 for related discussion and diagrams of the 4π Array.

Table A.1: Solid angle subtended by the Ball Phoswiches.

Module Type	Ideal (msr)	True (msr)
Hexagon	(6×) 75.2	66.0
Pentagon	(5×) 59.0	49.9

Table A.2: Solid angle subtended by the HRA Phoswiches.

HRA Detector Number	Solid Angle (msr each)
1, 2, 3, 4, 5, 6, 7, 8, 9, 10	5.11
12, 15, 18, 21, 24	6.27
11, 13, 14, 16, 17, 19, 20, 22, 23, 25	6.18
27, 28, 31, 32, 35, 36, 39, 40, 43, 44	6.88
26, 29, 30, 33, 34, 37, 38, 41, 42, 45	6.65

Table A.3: Phoswich Scintillator Specifications.

Element	Plastic	Thickness (mm)	Rise time (ns)	Decay time (ns)
Ball Fast ΔE	BC412	3.2	1.0	3.3
Ball Slow E	BC444	250	20	180
HRA Fast ΔE	NE110	1.7	1.1	3.3
HRA Slow E	NE115	194	8.0	320

Table A.4: Low Energy Thresholds for the HRA.

Particle Type	Punch-in Energy (MeV)	Particle Type	Punch-in Energy (MeV)	Particle Type	Punch-in Energy (MeV)
p	13	C	269	Al	877
d	17	N	341	Si	962
t	20	O	419	P	1079
He	50	F	515	S	1170
Li	99	Ne	591	Cl	1294
Be	152	Na	687	Ar	1455
B	212	Mg	767		

Table A.5: Low Energy Thresholds for the Ball Telescopes.

Particle Type	Punch-in Energy (MeV)	Particle Type	Punch-in Energy (MeV)	Particle Type	Punch-in Energy (MeV)
He	12	N	74	Mg	163
Li	23	O	91	Al	184
Be	34	F	108	Si	202
B	46	Ne	123	P	224
C	59	Na	146	S	242

Table A.6: Mean angles for the ball phoswiches.

Module	A		B		C		D		E		F	
	θ	ϕ	θ	ϕ	θ	ϕ	θ	ϕ	θ	ϕ	θ	ϕ
1	23.1	342.0	32.3	5.6	46.0	356.3	51.7	342.0	46.0	324.7	32.3	318.4
2	23.1	270.0	32.3	293.6	46.0	287.3	51.7	270.0	46.0	252.7	32.3	246.4
3	23.1	198.0	32.3	221.6	46.0	215.3	51.7	198.0	46.0	180.7	32.3	174.4
4	23.1	126.0	32.3	149.6	46.0	143.3	51.7	126.0	46.0	108.7	32.3	102.4
5	23.1	54.0	32.3	77.6	46.0	71.3	51.7	54.0	46.0	36.7	32.3	30.4
6	54.7	298.0	54.7	314.0	67.3	317.5	74.6	306.0	67.3	294.5		
7	54.7	226.0	54.7	242.0	67.3	245.5	74.6	234.0	67.3	222.5		
8	54.7	154.0	54.7	170.0	67.3	173.5	74.6	162.0	67.3	150.5		
9	54.7	82.0	54.7	98.0	67.3	101.5	74.6	90.0	67.3	78.5		
10	54.7	10.0	54.7	26.0	67.3	29.5	74.6	18.0	67.3	6.5		
11	64.9	342.0	72.4	355.0	86.5	354.4	93.5	342.0	86.5	329.6	72.4	329.0
12	64.9	270.0	72.4	283.0	86.5	282.4	93.5	270.0	86.5	257.6	72.4	257.0
13	64.9	198.0	72.4	211.0	86.5	210.4	93.5	198.0	86.5	185.6	72.4	185.0
14	64.9	126.0	72.4	139.0	86.5	138.4	93.5	126.0	86.5	113.6	72.4	113.0
15	64.9	54.0	72.4	67.0	86.5	66.4	93.5	54.0	86.5	41.6	72.4	41.0
16	86.5	306.0	93.5	318.4	107.6	319.0	115.1	306.0	107.6	293.0	93.5	293.6
17	86.5	234.0	93.5	246.4	107.6	247.0	115.1	234.0	107.6	221.0	93.5	221.6
18	86.5	162.0	93.5	174.4	107.6	175.0	115.1	162.0	107.6	149.0	93.5	149.6
19	86.5	90.0	93.5	102.4	107.6	103.0	115.1	90.0	107.6	77.0	93.5	77.6
20	86.5	18.0	93.5	30.4	107.6	31.0	115.1	18.0	107.6	5.0	93.5	5.6
21	105.4	342.0	112.7	353.5	125.3	350.0	125.3	334.0	112.7	330.5		
22	105.4	270.0	112.7	281.5	125.3	278.0	125.3	262.0	112.7	258.5		
23	105.4	198.0	112.7	209.5	125.3	206.0	125.3	190.0	112.7	186.5		
24	105.4	126.0	112.7	137.5	125.3	134.0	125.3	118.0	112.7	114.5		
25	105.4	54.0	112.7	65.5	125.3	62.0	125.3	46.0	112.7	42.5		
26	128.3	306.0	134.0	323.3	147.7	329.6	156.9	306.0	147.7	282.4	134.0	288.7
27	128.3	234.0	134.0	251.3	147.7	257.6	156.9	234.0	147.7	210.4	134.0	216.7
28	128.3	162.0	134.0	179.3	147.7	185.6	156.9	162.0	147.7	138.4	134.0	144.7
29	128.3	90.0	134.0	107.3	147.7	113.6	156.9	90.0	147.7	66.4	134.0	72.7
30	128.3	18.0	134.0	35.3	147.7	41.6	156.9	18.0	147.7	354.4	134.0	0.7

Table A.7: Mean angles for the HRA phoswiches.

Detector	θ	ϕ	Detector	θ	ϕ	Detector	θ	ϕ
1	5.4	0.0	16	10.6	246.0	31	14.3	279.0
2	5.4	324.0	17	10.6	222.0	32	14.3	261.0
3	5.4	288.0	18	9.6	198.0	33	15.9	243.0
4	5.4	252.0	19	10.6	174.0	34	15.9	225.0
5	5.4	216.0	20	10.6	150.0	35	14.3	207.0
6	5.4	180.0	21	9.6	126.0	36	14.3	189.0
7	5.4	144.0	22	10.6	102.0	37	15.9	171.0
8	5.4	108.0	23	10.6	78.0	38	15.9	153.0
9	5.4	72.0	24	9.6	54.0	39	14.3	135.0
10	5.4	36.0	25	10.6	30.0	40	14.3	117.0
11	10.6	6.0	26	15.9	9.0	41	15.9	99.0
12	9.6	342.0	27	14.3	351.0	42	15.9	81.0
13	10.6	318.0	28	14.3	333.0	43	14.3	63.0
14	10.6	294.0	29	15.9	315.0	44	14.3	45.0
15	9.6	270.0	30	15.9	297.0	45	15.9	27.0

LIST OF REFERENCES

[1] Committee on Nuclear Physics, *Nuclear Physics: The Core of Matter, The Fuel of Stars* (National Academy Press, 1999).

[2] V. Ninov *et al.*, *Phys. Rev. Lett.* **83**, 1104 (1999).

[3] M. Mukerjee, *Sci. Am.* **3**, 64 (2000).

[4] S.M. Wong, *Introductory Nuclear Physics* (Prentice-Hall, 1999).

[5] D. Bandyopadhyay *et al.*, *Nucl. Phys.* **A511**, 1 (1990).

[6] H. Jaqaman *et al.*, *Phys. Rev.* C **27**, 2782 (1983).

[7] S.H. Kahana, *Ann. Rev. Nucl. Part. Sci.* **39**, 231 (1989).

[8] W.D. Myers and W.J. Swiatecki, *Phys. Rev.* C **57**, 3020 (1998).

[9] J.W. Harris and B. Müller, *Ann. Rev. Nucl. Part. Sci.* **46**, 71 (1996).

[10] W. Bauer, G.F. Bertsch, and U. Mosel, *Phys. Rev.* C **34**, 2127 (1986).

[11] N.W. Ashcroft and N.D. Mermin, *Solid State Physics* (Saunders, 1976).

[12] C. Mahaux and R. Sartor, "Nuclear Matter With Non-Relativistic Potentials," *Nuclear Matter and Heavy Ion Collisions* (Plenum, 1989).

[13] J.P. Blaizot, *Phys. Rep.* **64**, 171 (1980).

[14] W.D. Myers and W.J. Swiatecki, *Ann. Phys.* **84**, 211 (1974).

[15] J. Cooperstein, *Phys. Rev.* C **37**, 786 (1988).

[16] M. Prakash, T.L. Ainsworth, and J.M. Lattimer, *Phys. Rev. Lett.* **61**, 2518 (1988).

[17] J. Madsen, *Phys. Rev. Lett.* **81**, 3311 (1998).

[18] D. Klakow, G. Welke, and W. Bauer, *Phys. Rev.* C **48**, 1982 (1993).

[19] F. Daffin, Ph.D. Thesis (1998).

[20] S.Z. Belenkij and L.D. Landau, *Nuovo Cimento Suppl.* **3**, 15 (1956).

[21] H.A. Gustafsson *et al.*, *Phys. Rev. Lett.* **52**, 1590 (1984).

[22] K.A. Brückner, *Phys. Rev.* **97**, 1353 (1955).

[23] G.D. Westfall *et al.*, *Phys. Rev. Lett.* **37**, 1202 (1976).

[24] R. Pak *et al.*, *Phys. Rev.* C **54**, 1681 (1996).

[25] W. Reisdorf and H.G. Ritter, *Ann. Rev. Nucl. Part. Sci.* **47**, 663 (1997).

[26] C.A. Ogilvie *et al.*, *Phys. Rev.* C **42**, R10 (1990).

[27] C. Pinkenburg *et al.*, *Phys. Rev. Lett.* **83**, 1295 (1999).

[28] C.M. Hung and E.V. Shuryak, *Phys. Rev. Lett.* **75**, 4003 (1995).

[29] W.K. Wilson *et al.*, *Phys. Rev.* C **41**, R1181 (1990).

[30] G.D. Westfall *et al.*, *Nucl. Instrum. Methods* **A238**, 347 (1985).

[31] C.R. Gruhn *et al.*, *Nucl. Instrum. Methods* **196**, 33 (1982).

[32] G.F. Knoll, *Radiation Detection and Measurement*, Second Edition (John Wiley & Sons, 1989)

[33] R. Pak *et al.*, *NSCL/MSU Ann. Rep.* 233 (1992)

[34] N.T.B. Stone, Ph.D. Thesis (1996).

[35] R. Pak, Ph.D. Thesis (1996).

[36] C. Cavata *et al.*, *Phys. Rev.* C **42**, 1760 (1990).

[37] C.A. Ogilvie *et al.*, *Phys. Rev.* C **40**, 654 (1989).

[38] L. Phair *et al.*, *Nucl. Phys.* **A548**, 489 (1992).

[39] R. Pak, Ph.D. Thesis , (1996).

[40] J. Cugnon *et al.*, *Phys. Lett.* **109B**, 146 (1985).

[41] W.K. WIlson, R. Lacey, C.A. Ogilvie, and G.D. Westfall, *Phys. Rev.* C **45**, 738 (1992).

[42] Alice WWW Home [Online] http://www.cern.ch/Alice

[43] A.M. Poskanser and S.A. Voloshin, *Phys. Rev.* C **58**, 1671 (1998).

[44] J. Barrette *et al.*, *Phys. Rev.* C **55**, 1420 (1997).

[45] A.E. Glassgold, W. Heckrotte, and K.M. Watson, *Ann. Phys.* **6**, 1 (1959).

[46] *The Particle Century*, edited by G. Fraser (Institute of Physics Pub., 1998).

[47] W. Scheid, H. Müller, and W. Greiner, *Phys. Rev. Lett.* **32**, 741 (1974).

[48] H. Stöcker and W. Greiner, *Phys. Rep.* **137**, 277 (1986).

[49] M. Gyulassy, K.A. Frankel, and H. Stöcker, *Phys. Lett.* **110B**, 185 (1982).

[50] R.E. Renfordt *et al.*, *Phys. Rev. Lett.* **53**, 763 (1984).

[51] H.A. Gustafsson *et al.*, *Phys. Rev. Lett.* **52**, 1594 (1984).

[52] P. Danielewicz and G. Odyniec, *Phys. Lett.* **157B**, 146 (1985).

[53] H. Stöcker, J.A. Maruhn, and W. Greiner, *Phys. Rev. Lett.* **44**, 725 (1980).

[54] G.F. Bertsch and S. DasGupta, *Phys. Rep.* **160**, 189 (1988).

[55] J. Aichelin and H. Stöcker, *Phys. Lett.* B **176**, 14 (1986).

[56] D. Krofcheck *et al.*, *Phys. Rev. Lett.* **63**, 2028 (1989).

[57] G.D. Westfall *et al.*, *Phys. Rev. Lett.* **71**, 1986 (1993).

[58] R. Pak *et al.*, *Phys. Rev.* C **54**, 2457 (1996).

[59] R. Pak *et al.*, *Phys. Rev. Lett.* **78**, 1026 (1997).

[60] R. Pak *et al.*, *Phys. Rev.* C **53**, R1469 (1996).

[61] J. Gosset *et al.*, *Phys. Rev. Lett.* **62**, 1251 (1989).

[62] D.H. Rischke, *Nucl. Phys.* **A610**, 88c (1996).

[63] H.A. Gustafsson *et al.*, *Mod. Phys. Lett. A* **3**, 1323 (1988).

[64] W.M. Zhang *et al.*, *Phys. Rev.* C **42**, R491 (1990).

[65] M. Partlan *et al.*, *Phys. Rev. Lett.* **75**, 2100 (1995).

[66] P. Crochet *et al.*, *Nucl. Phys.* **A624**, 755 (1997).

[67] H. Zhou, Z. Li, and Y. Zhuo, *Phys. Rev.* C **50**, R2664 (1994).

[68] S. Soff *et al.*, *Phys. Rev.* C **51**, 3320 (1995).

[69] Z.Y. He *et al.*, *Nucl. Phys.* **A598**, 248 (1996).

[70] W.G. Meyer *et al.*, *Phys. Rev.* C **25**, 179 (1980).

[71] H. Appelshauser *et al.*, *Phys. Rev. Lett.* **80**, 4136 (1998).

[72] D.A. Cebra and W. Caskey (private communication).

[73] J. Barrette *et al.*, *Phys. Rev.* C **56**, 3254 (1997).

[74] W. Bauer, C.K. Gelbke, and S. Pratt, *Ann. Rev. Nucl. Part. Sci.* **42**, 77 (1992).

[75] J.J. Molitoris and H. Stöcker, *Phys. Rev.* C **32**, 346 (1985).

[76] D. Krofcheck *et al.*, *Phys. Rev.* C **46**, 1416 (1992).

[77] G.F. Bertch, W.G. Lynch, and M.B. Tsang, *Phys. Lett.* B **189**, 384 (1987).

[78] W. Bauer, *Phys. Rev. Lett.* **61**, 2534 (1999)..

[79] Y. Zheng *et al.*, *Phys. Rev.* C **83**, 2534 (1999).

[80] N.T.B. Stone *et al.*, *Phys. Rev. Lett.* **78**, 2084 (1997).

[81] D. Magestro *et al.*, *Phys. Rev.* C **62**, ??? (2000).

[82] K.C. Chung, C.S. Wang, and A.J. Santiago, *Phys. Rev.* C **59**, 714 (1999).

[83] D.H. Youngblood *et al.*, *Phys. Rev. Lett.* **82**, 691 (1999).

[84] F. Haddad *et al.*, *Phys. Rev.* C **53**, 1437 (1996).

[85] Q. Pan and P. Danielewicz, *Phys. Rev. Lett.* **70**, 2062 (1993).

[86] H. Stöcker *et al.*, *Phys. Rev.* C **25**, 1873 (1982).

[87] M. Demoulins *et al.*, *Phys. Lett.* B **241**, 476 (1990).

[88] H.H. Gutbrod *et al.*, *Phys. Lett.* B **216**, 267 (1989).

[89] H. Sorge, *Phys. Rev. Lett.* **78**, 2309 (1997).

[90] J. Barrette *et al.*, *Phys. Rev. Lett.* **73**, 2532 (1994).

[91] H.H. Gutbrod *et al.*, *Phys. Rev.* C **42**, 640 (1990).

[92] R. Popescu *et al.*, *Phys. Lett.* B **331**, 285 (1994).

[93] M.B. Tsang *et al.*, *Phys. Rev.* C **53**, 1959 (1996).

[94] C. Hartnack *et al.*, *Mod. Phys. Lett. A* **13**, 1151 (1994).

[95] P. Danielewicz *et al.*, *Phys. Rev. Lett.* **81**, 2438 (1998).

[96] B.A. Li, C.M. Ko, and Z.Z. Ren, *Phys. Rev. Lett.* **78**, 1644 (1997).

[97] N. Bastid *et al.*, *Nucl. Phys.* **A622**, 573 (1997).

[98] A. Andronic, FOPI Collaboration, *Quark Matter '99* , (1999).

[99] W.K. Wilson, Ph.D. Thesis (1990).

[100] A. Andronic, GSI (private communication).